

# Temperature-Controlled Microchip Liquid Chromatography System

Thesis by

**Victor Chi-Yuan Shih**

In Partial Fulfillment of the Requirements  
for the Degree of

Doctor of Philosophy



California Institute of Technology

Pasadena, California

2006

(Defended April 11, 2006)

© 2006

Victor Chi-Yuan Shih

All Rights Reserved

To my parents and wife

## Acknowledgements

My advisor, Dr. Yu-Chong Tai, made my Ph.D. study the most significant and fruitful experience in my life. Working with Dr. Tai day in and day out for five years, I was amazed by his wisdom in making the right decisions, doing the right things at the right time. He showed me the art of managing things according to priority, by which one's limited time and energy can be leveraged to maximize achievements. Although extremely demanding on research, Dr. Tai has never failed to cheer us up with optimism and a sense of humor when reality showed cold faces to our efforts. Dr. Tai makes our Lab a fun place to work with his fairness to people, generosity, and unique fearless leadership. I was so lucky to work with him and have a mentor like him.

My parents have given me tremendous support in every aspect and stage of my life. They worked hard and saved every possible penny to provide the best environment and resources for their children. Being away from them for many years, I often regretted that I was not able to appreciate more their love and share their hardship in my young years. This thesis is dedicated to them, as a present for their sixtieth birthdays. Dear dad and mom, I have missed you so much these years and happy birthday to you!

My wife, Vanessa Lin, is an amazing lady. She makes me laugh all the time! I could not imagine what a miserable life I would have led without her taking care of me each day during this energy-challenging five years at Caltech. While many student-dependents found life here not much fun, my wife found her way out by making many friends, taking interesting courses, and shopping everywhere. Her incredible ability

to cook all kinds of delicious food made my dining time the happiest of every day. With her faith in me, I have overcome bad times and failures. Most important of all, my efforts in life are all worth it when she is beside me to share the joys. I am the luckiest man to have met her and to have her as my wife. (Vanessa, I love you!)<sup>∞</sup>.

I would also like to thank the current and previous members of the Caltech Micromachining Laboratory who have given me advice and help. Mr. Trevor Roper is a respectful technician from whom I have learned tremendously. It has always been a wonderful experience working with him inside the cleanroom. Mrs. Christine Matsuki and Mrs. Tanya Owen are very nice secretaries and their help has extensively facilitated my research. Dr. Tze-Jung Yao, Dr. Yong Xu, Dr. Ellis Meng, Dr. Jun Xie, Dr. Qing He, Dr. Matthieu Liger, Dr. Justin Boland, and Mr. Ted Harder have given me great advice in research and have been good friends of mine over the years. Special thanks are dedicated to Dr. Yao, who introduced me to this lovely lab, and Dr. Xie, with whom I had so many fruitful research discussions. My colleagues in our lab, Scott Miserendino, Changlin Pang, Angela Tooker, Siyang Zheng, Damien Rodger, Po-Jui Chen (we shared so much fun), Quoc Quach, Wen Li, Nick Lo, Jason Shih, and Mike Liu are wonderful working company. Yang Chen and Wei Li are outstanding Caltech undergrads with whom I have worked. I will never forget the joyful memories we shared over the years.

Finally, I would like to thank my Ph.D. candidacy and defense committee members: Prof. Terry D. Lee at City of Hope, Prof. Jerry Pine, Prof. David Rutledge, Prof. Demetri Psaltis, Prof. Changhui Yang, and Prof. Joel Burdick at Caltech for their insightful guidance and suggestions on my Ph.D. research.

## **Abstract**

# **Temperature-Controlled Microchip Liquid Chromatography System**

Thesis by

**Victor Chi-Yuan Shih**

Doctor of Philosophy in Electrical Engineering

California Institute of Technology

High-performance liquid chromatography (HPLC) is one of the most important analytical tools heavily used in the fields of chemistry, biotechnology, pharmaceuticals, and the food industry. The power of liquid chromatography comes from its ability to achieve molecular separation with extremely high efficiency and its great flexibility of incorporating versatile sensors for detecting a broad range of analytes. In the past decades, great efforts have been put into liquid chromatography instrumentation and methods, aiming to further improve separation efficiency, sensitivity, repeatability, throughput, and costs. The contribution of this thesis is to illustrate with real examples the great potential of MEMS microchip liquid chromatography systems with on-chip temperature control for replacing and improving the conventional desktop HPLC systems.

This thesis is composed of seven chapters. Chapter 1 gives an introduction to MEMS technology and its application in making lab-on-a-chip systems. Chapter 2 describes the theoretical background and the evolution of HPLC technology. Chapter 3 demonstrates how to use state-of-the-art MEMS technology to make high-pressure microfluidic channels, which will be used for constructing microchip HPLC systems later. Chapter 4 describes a temperature-controlled microchip HPLC system that uses a temporal temperature gradient to achieve analyte elution. Separation of amino acids and low density lipoproteins was successfully demonstrated using the proposed system. Chapter 5 describes a novel embedded HPLC system, which demonstrated a record high pressure capacity (> 1000 psi) among microchip HPLC systems. High quality separation results of trace-level daunorubicin and doxorubicin were obtained using the proposed system and laser-induced fluorescence detection. A novel  $C^4D$  sensor together with the RISE sensitivity enhancement method was proposed and investigated for the first time for microchip HPLC analyte detection. Chapter 6 describes the first work to pack 30 nm gold nanoparticles into the HPLC separation column as the stationary phase with the assistance of in-situ molecular self-assembly between nanoparticles and thiolated molecules. Preliminary results demonstrated the possibility of building fully filled nanoparticle HPLC columns for extremely high separation efficiency application. Chapter 7 then gives the conclusions of this thesis.

# Table of Contents

<b>Chapter 1</b>	<b>MEMS Technology</b> .....	1
1.1	Introduction.....	1
1.1.1	MEMS by Definition.....	1
1.1.2	MEMS Fabrication Technology.....	2
1.1.2.1	Bulk Micromachining.....	2
1.1.2.2	Surface Micromachining.....	6
1.1.2.3	Other Technologies.....	6
1.1.2.4	Summary.....	8
1.1.3	Market and Products of MEMS Technology.....	9
1.2	Lab-on-a-Chip System by MEMS Technology.....	12
1.2.1	Applications of Lab-on-a-Chip System.....	12
1.2.2	Challenges and Outlooks.....	14
1.3	Parylene as a Microstructure Material.....	16
1.3.1	Introduction to Parylene.....	16
1.3.2	Applications of Parylene Thin Film in MEMS.....	20
1.4	Bibliography.....	22
<b>Chapter 2</b>	<b>Evolution of HPLC Technology</b> .....	28
2.1	High-Performance Liquid Chromatography.....	28
2.1.1	Introduction.....	28
2.1.2	History.....	30
2.1.3	Theory.....	32
2.1.3.1	Analyte Retention and Chromatogram.....	32
2.1.3.2	Height Equivalent to a Theoretical Plate.....	36
2.1.3.3	Reduced/Dimensionless Parameters.....	37

2.1.3.4	Band-Broadening Phenomenon .....	38
2.2	HPLC Instrumentation.....	42
2.2.1	Separation Column .....	42
2.2.1.1	Separation Column Tube.....	42
2.2.1.2	Separation Column Packing Material .....	43
2.2.2	Solvent Pumps .....	45
2.2.3	Sample Injection Valves .....	46
2.2.4	Analyte Detectors .....	46
2.3	Logical Trend of HPLC Instrumentation.....	49
2.3.1	Predictions from the Theory .....	49
2.3.2	Benefits of Microchip HPLC System.....	50
2.4	Review of Microchip HPLC Systems.....	51
2.5	Comparisons between LC and CE.....	53
2.6	Conclusions.....	56
2.7	Bibliography .....	57
 <b>Chapter 3 High-Pressure Microfluidic Channel Technology .....</b>		<b>62</b>
3.1	Introduction.....	62
3.2	Review of Microfluidic Channel Technology... ..	63
3.2.1	PDMS Microfluidic Channel.....	63
3.2.2	Thermal-Bonding Microfluidic Channel.....	64
3.2.3	Nitride Microfluidic Channel .....	64
3.2.4	Parylene Microfluidic Channel.....	65
3.2.5	Buried Microfluidic Channel.....	66
3.3	High-Pressure Parylene Microfluidic Channel Technology .....	68
3.3.1	Anchored-Type Parylene Microfluidic Channel.....	68
3.3.2	Embedded-Type Parylene Microfluidic Channel .....	70

3.3.3	Comparisons .....	73
3.4	Conclusions.....	73
3.5	Bibliography .....	75
<b>Chapter 4</b>	<b>Temperature-Controlled Microchip HPLC System.....</b>	<b>78</b>
4.1	Temperature Gradient Interaction Chromatography.....	78
4.2	Chip Design, Fabrication, and, Characterization.....	81
4.2.1	Low-Power, Low-Pressure-Capacity System .....	81
4.2.1.1	Design and Fabrication .....	81
4.2.1.2	System Characterization.....	83
4.2.2	High-Power, High-Pressure-Capacity System.....	87
4.2.2.1	Design and Fabrication .....	87
4.2.2.2	System Characterization.....	90
4.2.2.3	Application of Parylene Thermal Isolation Technology .....	95
4.3	TGIC Chip Packaging.....	98
4.4	Stationary-Phase Particle Packing .....	99
4.5	Chip Temperature Programming .....	100
4.6	Examples of Separation .....	101
4.6.1	Amino Acid Separation.....	101
4.6.1.1	Introduction.....	101
4.6.1.2	Sample Preparation .....	102
4.6.1.3	Electrochemical Detection .....	104
4.6.1.4	Separation Results and Comments.....	104
4.6.2	Low Density Lipoprotein Separation.....	107
4.6.2.1	Introduction.....	107
4.6.2.2	Sample Preparation .....	109
4.6.2.3	Conductivity Detection .....	109

4.6.2.4	Separation Results and Comments.....	111
4.7	Conclusions.....	113
4.8	Bibliography .....	114
<b>Chapter 5</b>	<b>Embedded HPLC System.....</b>	<b>120</b>
5.1	Introduction.....	120
5.2	Single-Mask Embedded HPLC System.....	121
5.2.1	Design and Fabrication .....	121
5.2.2	System Characterization .....	124
5.3	Multiple-Mask Embedded HPLC system.....	126
5.3.1	Design and Fabrication .....	126
5.3.2	System Characterization .....	130
5.4	Laser-Induced Fluorescence Detection.....	134
5.4.1	Introduciton.....	134
5.4.2	System Design and Fabrication .....	135
5.4.3	LIF Detection Characterization .....	138
5.5	Capacitively-Coupled Contactless Conductivity Detection .....	139
5.5.1	Sensor Design and Fabrication .....	140
5.5.2	Sensor Characterization.....	141
5.5.3	Resonance-Induced Sensitivity Enhancement for C <sup>4</sup> D .....	143
5.6	LABVIEW Program for Complete HPLC Procedure Control .....	150
5.6.1	Program Design .....	150
5.6.2	Program Performance Characterization.....	151
5.7	Examples of Separation .....	155
5.7.1	Daunorubicin Elution.....	157
5.7.2	Separation of Daunorubicin and Doxorubicin.....	157
5.8	Conclusions.....	159

5.9	Bibliography .....	160
<b>Chapter 6</b>	<b>Packing Nanoparticles into HPLC Column.....</b>	<b>162</b>
6.1	Introduction.....	162
6.2	Molecular-Self-Assembly-Assisted Nanoparticle Packing .....	164
6.2.1	Concept.....	164
6.2.2	System Design and Fabrication .....	165
6.2.3	Molecular-Self-Assembly Characterizations.....	166
6.2.4	Column Packing Results and Comments.....	174
6.3	Conclusions.....	175
6.4	Bibliography .....	176
<b>Chapter 7</b>	<b>Conclusions.....</b>	<b>178</b>

## List of Figures

Figure 1-1: Bulk micromachining technology .....	4
Figure 1-2: Working mechanism of DRIE and representative structures .....	5
Figure 1-3: Surface micromachining technology .....	7
Figure 1-4: Integrated surface/bulk micromachining technology.....	8
Figure 1-5: Various microsystems market studies from 1990 to 2000 .....	11
Figure 1-6: Market breakout for 1st-level-packaged MEMS and MST products.....	11
Figure 1-7: Chemical structures of parylene N, C, and D .....	16
Figure 1-8: Parylene deposition system and the involved chemical processes .....	18
Figure 1-9: Parylene microfluidic devices.....	21
Figure 2-1: Illustration of the chromatographic separation process .....	29
Figure 2-2: The inventor of chromatography, Twsett, and his chromatographic device ..	31
Figure 2-3: Chromatogram and its characteristic features.....	32
Figure 2-4: Four mechanisms of band broadening.....	40
Figure 2-5: Van Deemter curve.....	41
Figure 2-6: Schematic plot for a typical HPLC system .....	42
Figure 2-7: Chemical modification of silica surface.....	44
Figure 2-8: A six-port, two-position manual sample injection valve.....	47
Figure 2-9: Microchip research activities on LC and CE .....	55
Figure 3-1: Pictures of assorted microfluidic channels.....	67
Figure 3-2: Anchored-type parylene channel.....	69
Figure 3-3: Cross-sectional pictures of a trench-anchored parylene channel .....	69
Figure 3-4: Basic embedded-type parylene channel.....	70
Figure 3-5: Fabrication process flow for the advanced embedded-type parylene channel	72
Figure 3-6: SEM of the advanced embedded-type parylene channel .....	72
Figure 4-1: Working principles of TGIC .....	80

Figure 4-2: Process flow for the low-power, low-pressure-capacity TGIC microchip.....	83
Figure 4-3: Photographs of the fabricated low-power, low-pressure-capacity TGIC device .....	84
Figure 4-4: Different channel configurations for pressure capacity study.....	85
Figure 4-5: Temperature coefficient of resistance (TCR) characterization of Ti/Pt resistive heater.....	86
Figure 4-6: Power consumption comparison .....	86
Figure 4-7: Process flow for the high-power, high-pressure-capacity TGIC microchip ..	88
Figure 4-8: Photographs of the fabricated high-power, high-pressure-capacity TGIC device.....	89
Figure 4-9: (a) Illustration of parylene-cross-linking structure, (b) a photograph showing the fabricated 150- $\mu\text{m}$ -wide, wafer-thickness air gap and the thermally isolated silicon temperature zone.....	90
Figure 4-10: FEMLAB simulation showing stress distribution inside the 10- $\mu\text{m}$ -thick parylene column wall under a 200 psi uniform pressure loading .....	91
Figure 4-11: Power consumption comparison .....	92
Figure 4-12: On-chip temperature rise ( $\Delta T$ ) spatial distribution during temperature gradient operation: (■) air-gap-surrounded island area, (□) off-island area .....	92
Figure 4-13: FEMLAB simulation showing an exaggerated vertical displacement of the thermally isolated silicon island loaded with uniform pressure from underneath .....	93
Figure 4-14: FEMLAB simulation showing vertical displacement of the thermally isolated silicon island as a function of DRIE trench depth “d”. .....	94
Figure 4-15: FEMLAB simulation showing flow-preheating around the silicon-made liquid access channel.....	94
Figure 4-16: Some representative thermal-isolation technologies.....	96
Figure 4-17: (a) Three temperature zones created by two air-gap rings on a silicon substrate for continuous-flow PCR applications, (b) a photograph showing the	

microfluidic channel crossing the air gap between temperature zones.....	97
Figure 4-18: (a) Continuous-flow PCR device with 10 PCR cycles, (b) thermal image of the powered-up PCR device.....	98
Figure 4-19: Exploded view of chip-packaging for chromatography tasks.....	99
Figure 4-20: Parylene column packed with 5- $\mu\text{m}$ -C18 silica particles using 200 psi nitrogen gas pressure source .....	100
Figure 4-21: Power/voltage input profile to generate on-chip constant temperature gradient .....	101
Figure 4-22: Cyclic voltammetry characterization of the derivatized amino acids .....	103
Figure 4-23: System setup for amino acid separation.....	105
Figure 4-24: Chromatogram showing derivatized amino acids separated using temperature gradient elution .....	106
Figure 4-25: Schematic illustration of nLDL/LDL <sup>-</sup> molecular structures .....	108
Figure 4-26: LDL separation obtained by conventional HPLC with salt gradient elution and UV detection .....	112
Figure 4-27: LDL separation obtained by microchip HPLC with isocratic elution at room temperature and conductivity detection.....	112
Figure 5-1: Top view of the 15 $\mu\text{m}$ parylene coating process. (a, b) Filter/column section, (c, d) liquid inlet/outlet before and after parylene coating.....	122
Figure 5-2: XeF <sub>2</sub> etching size-effect study .....	123
Figure 5-3: 5 $\mu\text{m}$ fluorescent beads packed into an embedded parylene column by slurry-packing .....	123
Figure 5-4: (a) Fabricated single-mask HPLC chip, (b) thin-film (skin) HPLC device by peeling parylene membrane from (a), (c) SEM picture of LIF detector channel profile. Parylene/oxide layer was peeled off .....	124
Figure 5-5: Embedded parylene channel loaded with 1015 psi inner pressure without fracture .....	125

Figure 5-6: Parylene column stress analysis under 100 psi inner pressure loading.....	125
Figure 5-7: Fabrication process flow for the multiple-mask embedded HPLC system..	127
Figure 5-8: (a, b) Top view of liquid access hole before and after the third parylene coating, (c, d) top view of the particle filter before and after the third parylene coating, (e) column cross-section, (f) filter cross-section after etching away top parylene layer.....	128
Figure 5-9: Embedded parylene column packed with 3 $\mu\text{m}$ (top) and 5 $\mu\text{m}$ (bottom) porous C18 silica particles using slurry-packing technique .....	129
Figure 5-10: (a) Formation mechanism for submicron-sized particle filter. (b) Actual picture of the submicron-sized particle filter, the red spot symbolizes a 1 $\mu\text{m}$ -sized particle .....	130
Figure 5-11: (a) Fabricated multiple-mask embedded HPLC microchip, (b) surface profile scan was obtained using Tencor P15 surface profiler, (c) chip packaging .....	131
Figure 5-12: Flow rate vs. pressure curve of the embedded LC column .....	134
Figure 5-13: (a) Schematic plot of the LIF system, (b) pictures of the actual system....	137
Figure 5-14: Laser spot alignment to microchip LIF detection cell .....	138
Figure 5-15: LIF signal standard deviation vs. signal level.....	139
Figure 5-16: C <sup>4</sup> D for capillary separation systems .....	140
Figure 5-17: C <sup>4</sup> D for microchip HPLC system.....	140
Figure 5-18: The equivalent circuit model of the C <sup>4</sup> D cell and its component values ...	141
Figure 5-19: Impedance analysis of the C <sup>4</sup> D cell .....	142
Figure 5-20: The transient responses of the C <sup>4</sup> D cell when the cell was filled with different media .....	143
Figure 5-21: The concept of resonance-induced sensitivity enhancement for C <sup>4</sup> D.....	146
Figure 5-22: HSPICE analysis of total impedance magnitude vs. frequency.....	147
Figure 5-23: Overall impedance change versus solution resistance at resonant frequency .....	148
Figure 5-24: Cell impedance fluctuation due to component value variations .....	148

Figure 5-25: User-interface of the developed LABVIEW program for the complete automatic control of HPLC procedures .....	152
Figure 5-26: Examples of temperature profile tracking performance of the LABVIEW program.....	154
Figure 5-27: Step-function temperature profile tracking.....	155
Figure 5-28: Sample injection and elution pumping procedures.....	156
Figure 5-29: Examples of separations.....	158
Figure 6-1: Micron-sized and nanometer-sized particles.....	163
Figure 6-2: Concept of molecular-self-assembly-assisted nanoparticle packing.....	165
Figure 6-3: (a) The process, (b) the design, and (c) the fabricated device of the PDMS/glass microfluidic system.....	166
Figure 6-4: (a) Chemical structure of the bisdisulfide model molecule, (b) a schematic plot of the assembled nanoparticle-molecule compound.....	167
Figure 6-5: Solvent system screening procedures .....	169
Figure 6-6: Solvent system screening test results.....	169
Figure 6-7: TEM and SEM pictures of gold nanoparticles.....	171
Figure 6-8: Electrical properties of the compound formed by gold nanoparticles and model molecules .....	173
Figure 6-9: Gold nanoparticle size effect on conjugation efficiency.....	173
Figure 6-10: Self-assembly and packing tests on PDMS devices.....	174
Figure 6-11: Packing self-assembled aggregate into the HPLC column .....	175

## List of Tables

Table 1-1: Comparisons of anisotropic silicon etchants .....	4
Table 1-2: Advantages of miniaturization technologies.....	10
Table 1-3: LOC companies .....	13
Table 1-4: Properties for parylene N, C, and D .....	20
Table 2-1: Typical sensitivity data for common HPLC detectors.....	47
Table 2-2: Comparisons between LC and CE.....	54
Table 4-1: Cardiovascular disease in the United States .....	108
Table 5-1: System leak rate testing.....	132
Table 5-2: Experimental verification of RISE method using discrete circuit components .....	149
Table 5-3: PID parameters used in all testing experiments.....	153
Table 5-4: Temperature standard deviations at various temperature levels.....	154

---

# CHAPTER 1

---

## MEMS TECHNOLOGY

### 1.1 Introduction

#### 1.1.1 MEMS by Definition

Micro-Electro-Mechanical Systems (MEMS) refer to micro-fabricated systems that contain at least some of their dimensions in the micrometer range. They are typically manufactured using planar processing technologies similar to semiconductor processes such as surface micromachining and/or bulk micromachining. MEMS devices generally range in sizes from a micrometer to a centimeter. MEMS are also called micromachines or microsystems technology (MST). Depending on the applications, MEMS can contain one or more microstructures that have electrical, mechanical, optical, and biological sensing or actuating functionality.

## **1.1.2 MEMS Fabrication Technology**

In the early years of its development, many of MEMS processing techniques were adapted from those used in the IC fabrication industry. Some representative processes were photolithography, thermal oxidation, diffusion, ion implantation, chemical vapor deposition (CVD), thermal evaporation, sputtering, wet chemical etching, and plasma etching. Over the years, as the applications of micromachining broadened, many microfabrication technologies have been developed. Those fabrication technologies can be categorized into bulk micromachining, surface micromachining, and other technologies that will be discussed in detail in the following sections.

### **1.1.2.1 Bulk Micromachining**

Bulk micromachining refers to microfabrication techniques used to form 3-D structures by selectively etching into the substrate, then removing the bulk of substrate to leave behind the desired micro structures. Although silicon is most often used as the substrate material, other materials such as glass, gallium arsenide, and quartz can also be used. The fabrication technique uses wet (chemical) or dry (plasma, gas) etching to etch the substrate with masking films to form micro structures in the substrate. The etching can be either isotropic (non-directional) or anisotropic (directional) depending on the etchant chemicals used as well as the crystal orientation of the substrate [1, 2] As follows, assorted frequently used etching techniques for silicon substrate will be discussed.

For isotropic silicon wet etching, HNA is often used. HNA is a combination of hydrofluoric, nitric, and acetic acid solutions [3]. The etching rate of silicon is

independent of the crystal orientation. It is a complex etching system with highly-variable etching rates. The major disadvantage of HNA is that it can be difficult to find an appropriate masking material since  $\text{SiO}_2$  is etched at a significant rate for all mix ratios.  $\text{Si}_3\text{N}_4$  or Au is desirable as a masking material because of its lower etching rate in HNA.

Gas phase isotropic silicon etching techniques are also available. The fluorine-based inert halogens in the vapor phase, such as xenon difluoride ( $\text{XeF}_2$ ) [4, 5] and bromine trifluoride ( $\text{BrF}_3$ ) [6], can spontaneously etch silicon when in contact. Several unique advantages are available for this gas phase etching process. For example, the etching process is carried out at room temperature and will not generate any mechanical stress due to material thermal mismatch [7]. Also, compared with liquid phase etching process, gas phase etching is mechanically much gentler, which is critical for preserving fragile micro structures on the wafer during etching. Moreover, the stiction problem that is often encountered when releasing micro structures such as beams, cantilevers, or diaphragms using wet etching can be completely avoided in the gas phase etching system [8]. Finally,  $\text{XeF}_2$  or  $\text{BrF}_3$  has high etching selectivity over most masking materials, such as silicon dioxide ( $> 3000:1$ ), silicon nitride ( $> 400:1$ ), photoresist ( $> 1000:1$ ) and metal (Cr, Au) ( $> 1000:1$ ) [6].

For anisotropic silicon etching such as EDP [9], KOH [10], or TMAH [11], etching is much faster in some crystal plane directions than in others. In fact, the etching rate is slowest in the  $\langle 111 \rangle$  direction and fastest in the  $\langle 100 \rangle$  and  $\langle 110 \rangle$  directions. Accordingly, planes of  $\langle 111 \rangle$ ,  $\langle 100 \rangle$ , and  $\langle 110 \rangle$  will reveal during the etching and form angles of  $54.74^\circ$  between  $\langle 100 \rangle / \langle 111 \rangle$  planes and  $90^\circ$  between  $\langle 110 \rangle / \langle 111 \rangle$  planes,

respectively, as illustrated in Figure 1-1. Table 1-1 summarizes etching specifications for EDP, KOH, and TMAH.

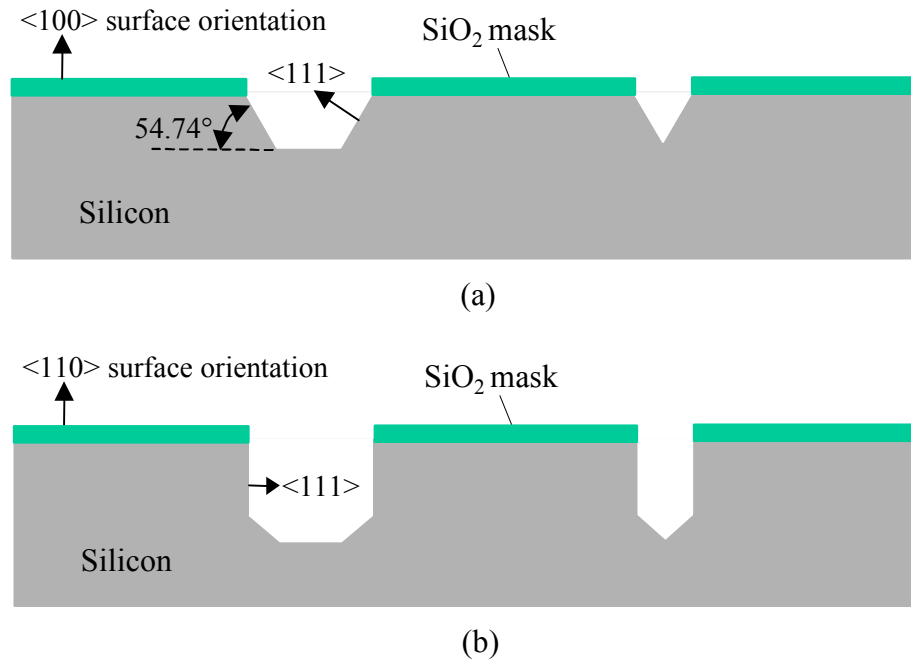


Figure 1-1: Bulk micromachining technology. (a) Anisotropic etching on <100> surface orientation, and (b) anisotropic etching on <110> surface orientation.

Table 1-1: Comparisons of anisotropic silicon etchants.

Etchant	Typical etching conditions	Anisotropic <100>/<111> etch ratio	Boron etch stop	Etch rate of masking layers
EDP	50 - 115 °C 20 - 80 μm/hr	10 - 35	@ 2 x 10 <sup>20</sup> cm <sup>-3</sup> boron, etch rate reduced by 10 <sup>3</sup>	SiO <sub>2</sub> (2 Å/min) Si <sub>3</sub> N <sub>4</sub> (1 Å/min)
KOH	50 - 90 °C 10 - 100 μm/hr	100 - 400	@ 2 x 10 <sup>20</sup> cm <sup>-3</sup> boron, etch rate reduced by 100	SiO <sub>2</sub> (14 Å/min) Si <sub>3</sub> N <sub>4</sub> (negligible)
TMAH	60 - 90 °C 10 - 60 μm/hr	10 - 20	@ 2 x 10 <sup>20</sup> cm <sup>-3</sup> boron, etch rate reduced by 10	SiO <sub>2</sub> (2 Å/min) Si <sub>3</sub> N <sub>4</sub> (negligible)

Another popular anisotropic silicon etching process is deep reactive ion etching (DRIE) [12]. DRIE can create very high aspect ratio structures ( $> 20:1$ ) into the silicon substrate with straight sidewalls. DRIE etching selectivity of silicon over photoresist and  $\text{SiO}_2$  are around 50:1 and 100:1, respectively. Figure 1-2 shows the working principle of DRIE and some of the fabricated micro structures.

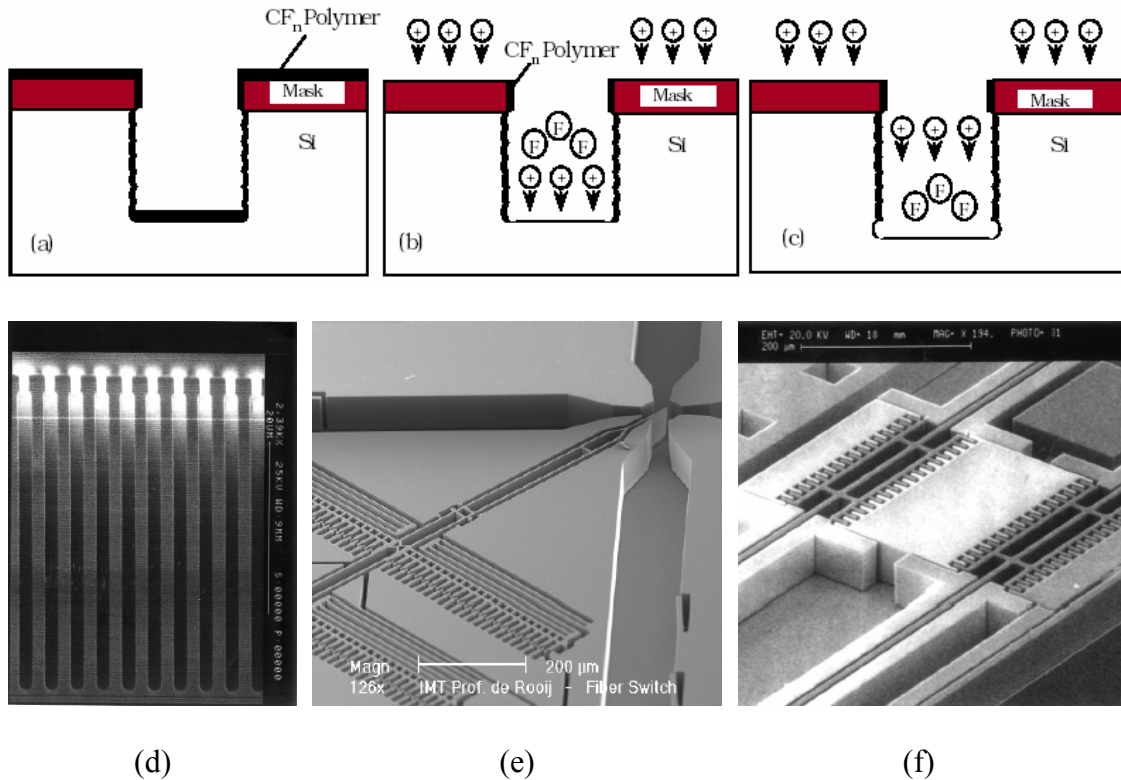


Figure 1-2: Working mechanism of DRIE and representative structures. (a)-(c), an illustration of DRIE working mechanism showing alternating passivating and etch cycles [12]. During the passivating cycle (a), fluorocarbon polymer covers all surfaces. During the initial part of the etch cycle (b), the polymer is removed from the base of the trench with the assistance of ion energy. During the rest of the etch cycle (c), the exposed silicon is etched isotropically. (d)  $1\mu\text{m}$ -wide trenches etched to  $35\mu\text{m}$  depth [12]. (e) A fiber-optic switch etched using DRIE. (f) An accelerometer fabricated with DRIE [12].

### 1.1.2.2 Surface Micromachining Technology

Surface micromachining technology is used for building micro structures on top of the substrate. Structures are in general formed using multiple steps of thin-film processes. The substrate only provides a mechanical support for the surface thin-film structures and typically does not participate in the processing.

A typical surface micromachining process uses two types of thin-film materials: structural and sacrificial materials. The structural materials can be polysilicon, SiO<sub>2</sub>, Si<sub>3</sub>N<sub>4</sub>, different types of polymers (parylene, PMMA, Teflon, etc.) or even metals. The sacrificial layers can be polysilicon, phosphosilicate glass (PSG), SiO<sub>2</sub>, polymers (photoresist and polyimide), or metals. In the beginning of the process, a sacrificial layer is deposited and patterned on the substrate (Figure 1-3). The structural layer is then deposited and patterned into desirable forms. Finally, the sacrificial layer is removed by wet or dry etching to release the target structures. With multiple layers of different structural materials deposited on top of each other, complicated devices of various functionalities can be fabricated as shown in Figure 1-3(d,e).

### 1.1.2.3 Other Technologies

Besides bulk and surface micromachining there are numerous MEMS fabrication technologies developed for specific applications. For example, LIGA (a German acronym for Lithographie, Galvanoformung, Abformung) combines the molding method with X-ray lithography and electroplating. The combination usage of electroplating and X-ray lithography was first carried out at IBM in 1975 by Romankiw, *et al.* [14]. The high-aspect-ratio metal structures were made by electroplating gold in X-ray-defined

resist patterns of height up to 20  $\mu\text{m}$ . This work was first done without the molding. The addition of molding to the lithography and electroplating process was developed by W. Ehrfeld, *et al.* [15]. The process is capable of yielding an extremely high-aspect-ratio structure (at least 100:1).

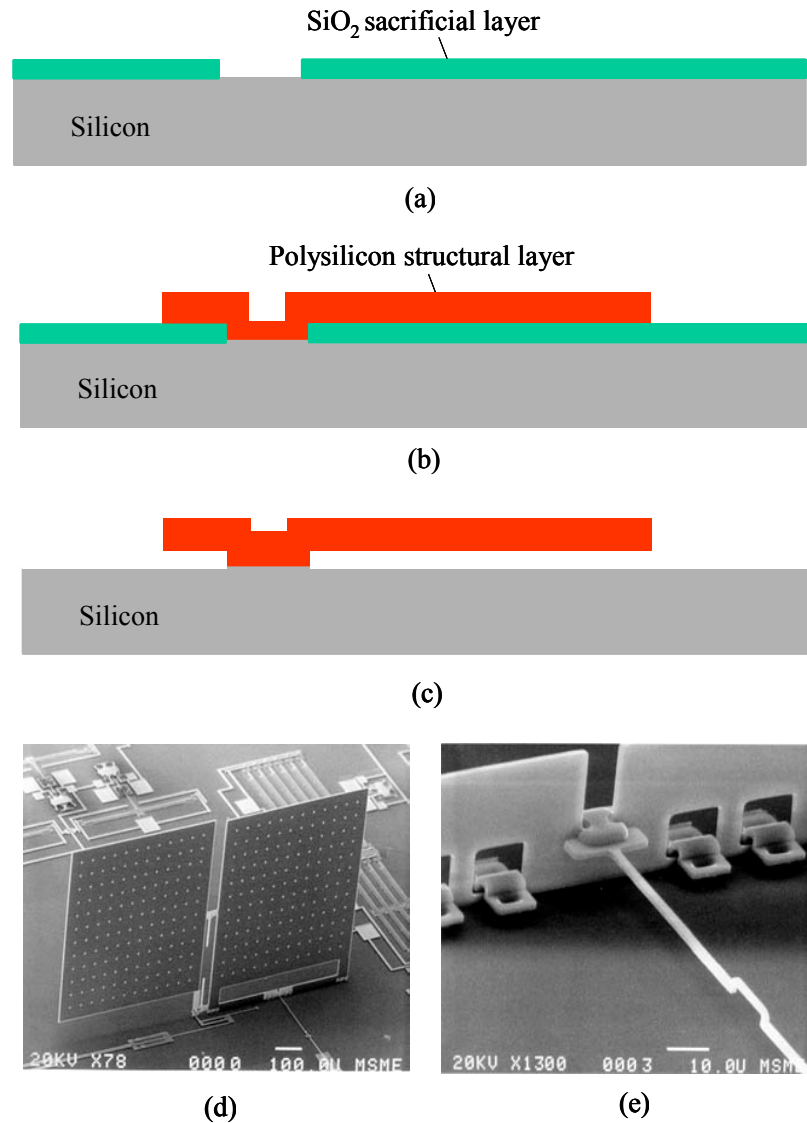


Figure 1-3: Surface micromachining technology, (a) deposition and patterning of  $\text{SiO}_2$  sacrificial layer, (b) deposition and patterning of polysilicon structural layer, (c) sacrificial layer releasing, (d, e) examples of surface micromachining devices [13].

Besides LIGA, some representative technologies include silicon-silicon fusion bonding [16], silicon-glass anodic bonding [17], 3-D stereolithography [18], micro electrical discharge machining (EDM) [19], laser micromachining [20], plastic injection molding [21], etc.

#### 1.1.2.4 Summary

MEMS fabrication technologies introduced above including bulk micromachining, surface micromachining, and others can be combined in a single process flow to make complicated micro structures to serve versatile application needs. For example, Figure 1-4 shows a silicon-micromachined neurochip upon which cultured mammalian neurons can be continuously and individually monitored and stimulated [22]. The neurochip is based upon a surface-micromachined 4x4 array of metal electrodes, each of which has a bulk-micromachined well structure (created by EDP etch) designed to hold a single mature cell body while permitting normal outgrowth of neural processes.

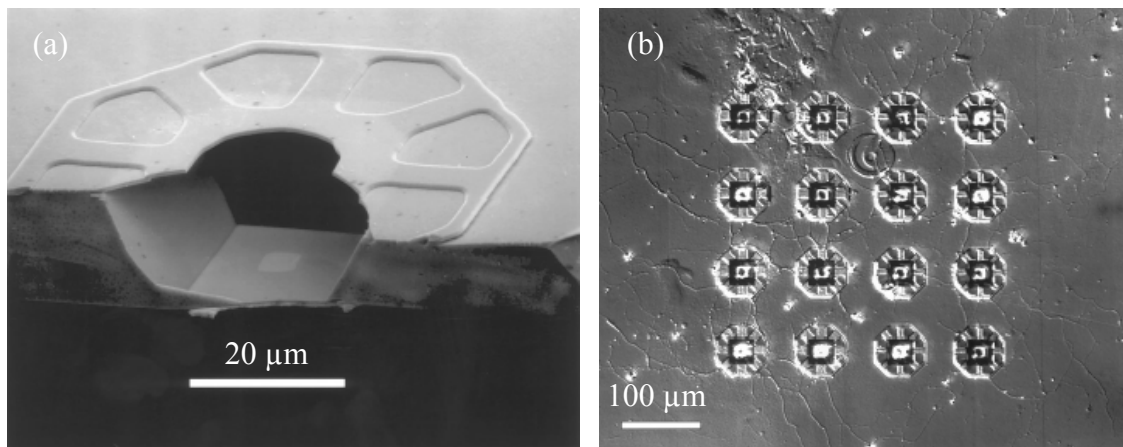


Figure 1-4: Integrated surface/bulk micromachining technology. (a) SEM of a neurochip cleaved to reveal the cross-section of a well. (b) Micrograph of a hippocampal culture on a 4x4 neurochip after 8 days in culture [22].

### **1.1.3 Market and Products of MEMS Technology**

In 1959, Richard Feynman gave his famous speech titled “There’s plenty of room at the bottom,” at Caltech, in which he declared the tremendous application opportunities in the miniaturization of machines [23]. In 1965, the first MEMS device, a resonant gate transistor, was demonstrated [24]. In 1982, Kurt Peterson’s groundbreaking paper “Silicon as a mechanical material,” [1] summarized many micromachining developments to that date, which greatly increased the awareness of MEMS. In 1989, researchers at the University of California Berkeley demonstrated the first IC-processed electrostatic micro-motors [25, 26], after which a wide variety of MEMS devices, technologies, and applications have been developed.

Over the past decade, various MEMS applications such as hard disk read/write heads, ink-jet printer head, pressure sensors, and accelerometers have proven their values in the marketplace. The fast-growing MEMS market and potential MEMS applications have attracted more and more researchers and funding resources into this field which effectively speeds up the commercialization of MEMS products. Table 1-2 lists some of the main reasons why miniaturization presents opportunities for product innovation in many application areas.

Figure 1-5 summarizes the results of 13 market studies published between 1990 and 2000 [28]. The wide disparity in totals comes from the different definitions of what is considered to be MEMS in various studies. A broader, beyond silicon, definition of products, which was used in the NEXUS report, results in the higher number of totals. The silicon-based MEMS products are actually only a small part of the total projected markets, and there is ample room for non-silicon-based products in the future MEMS

markets. According to the latest NEXUS market analysis for MEMS and Microsystems published in 2005, the MEMS market will grow from \$33 billion in 2004 to \$57 billion in 2009 with a growth rate of 11% per year [29]. The main drive for the market growth comes from the increasing consumer needs for read/write heads, micro displays and inkjet heads. Figure 1-6 shows the market breakout for 1st-level-packaged MEMS and MST products [29].

Table 1-2: Advantages of miniaturization technologies [27].

- 
- Minimizing of energy and materials consumption during manufacturing
  - Redundancy and arrays
  - Integration with electronics, simplifying systems
  - Increased sensor selectivity and sensitivity
  - Minimally invasive medical devices
  - Wider dynamic range
  - Exploring new phenomena in the micro domain for applications
  - Improved accuracy and reliability
  - Self-assembly and biomimetics with nanochemistry
  - More intelligent materials with structures at the nanoscale
- 

It is important to note that while MEMS borrows fabrication technologies from the IC world, it has a very different market character. The cost of ICs can be lowered when the quantity of parts numbers in the millions per year. For silicon-based sensors to succeed on the same scale as ICs, one must then concentrate on mass-consumption products such as cars, air conditioners, toys, etc. However, about 50,000 types of sensors exist to measure 100 different physical and chemical parameters, so often only 1,000 to 10,000 units are needed for each type of sensor per year. Therefore fragmentation becomes the characteristic in the sensor or other MEMS category markets [27].

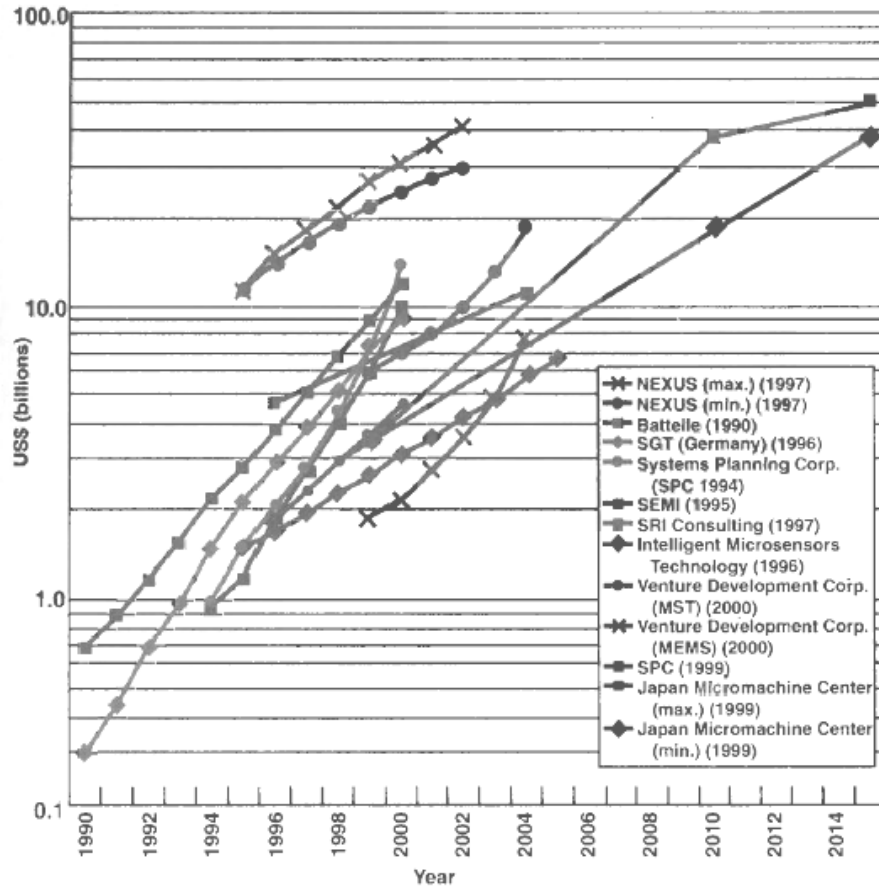


Figure 1-5: Various microsystems market studies from 1990 to 2000 [28].

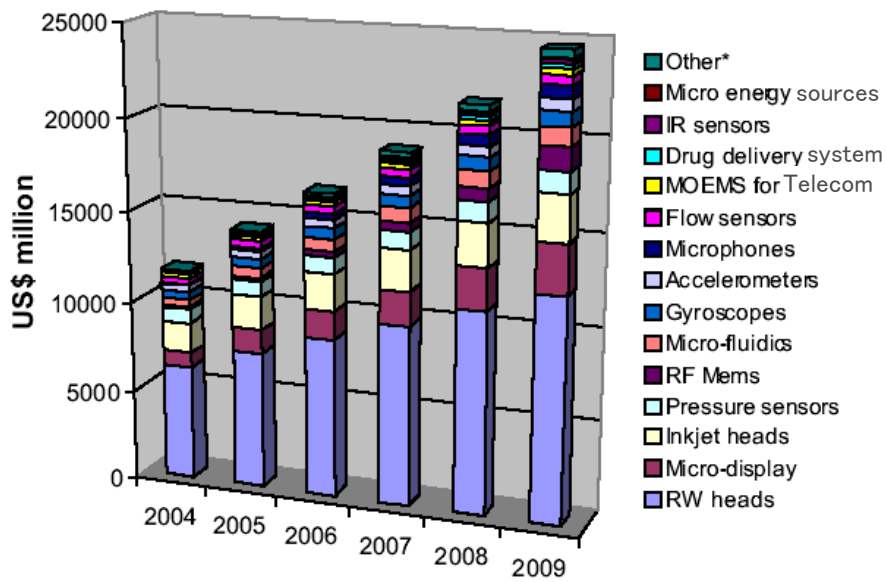


Figure 1-6: Market breakout for 1st-level-packaged MEMS and MST products [29].

## **1.2 Lab-on-a-Chip System by MEMS Technology**

Over the past decade, MEMS has grown rapidly to cover a wide variety of applications in many fields such as MOEMS (Micro-Optical-Electro-Mechanical System), RF-MEMS, Bio-MEMS, and Lab-on-a-Chip System (LOC). Among all MEMS applications, LOC is one of the most exciting and promising fields, which has attracted tremendous research resources from industry and academia.

### **1.2.1 Applications of Lab-on-a-Chip System**

The concept of lab-on-a-chip is the miniaturization and integration of the complete functionality of a chemistry or biology lab, such as sample preparation, reactions, separations, and detection, onto a single chip. The advantages of LOC compared with its desktop counterparts are manyfold. For example, the system physical size is significantly smaller and therefore of much higher portability. Power, sample, reagent consumption and operational costs are greatly reduced [30]. Faster analysis is achievable due to the significantly smaller system fluidic dead/swept volume. Also, because of the large surface to volume ratio in microfluidics, analysis sensitivity and limit of detection can be improved. Finally, the batch-fabrication of LOC using MEMS technology effectively reduces manufacturing cost and accordingly the LOC systems are highly disposable.

The birth date of the first LOC system can be traced back to 1979 when a miniaturized gas chromatography system was demonstrated [31]. Today, LOC has grown tremendously into a large, multidisciplinary field. The field is extensively reviewed in several papers from Manz's group [32-34]. Some major applications of LOC

include proteomics and genomics research, high-throughput screening (HTS) of drug candidates, point-of-care (POC) diagnostics, drug delivery, environment monitoring, industrial online analysis, food safety, bio-defense, etc. Table 1-3 lists some of the prominent LOC companies and their technologies/products [27].

Table 1-3: LOC companies [27].

<b>Company</b>	<b>Product</b>
Aclara Biosciences (Mountain View, CA)	Plastic microfluidic chips (LabCard) for drug screening and genomic applications
Agilent Technologies (Palo Alto, CA)	Manufacturing and marketing instruments for Caliper Technologies' LabChips
Amersham Pharmacia Biotech/Molecular Dynamics (Piscataway, NJ)	Researching microchannel electrophoresis DNA sequencing devices
Applied Biosystems (Foster City, CA)	Collaborating with Aclara Biosciences to develop and market LabCard Systems
Caliper Technologies (Mountain View, CA)	Lab-on-chip devices, moving small volumes of liquids using electrical and pressure; applications include DNA and RNA analysis and protein separations
Cepheid (Sunnyvale, CA)	DNA analysis systems based on microfluidics and microelectronics technology, emphasis on sample preparation and real time PCR
Tecan Boston (Medford, MA)	Lab-on-a-disc technology that uses centripetal force to move liquids; supporting a wide variety of bioanalytical applications
Burstein Technologies (Irvine, CA)	Lab-on-a-disk technology with emphasis on diagnostics
Gyros (Sweden)	Lab-on-a-disk technology that uses centripetal force to move liquids; supporting a wide variety of bioanalytical applications
Orchid Biosciences (Princeton, NJ)	Focusing on a microfluidic system for combinatorial drug synthesis
Micronics (Redmond, WA)	Microfluidics systems for diagnostics, analytical chemistry, and process applications
Nanogen (San Diego, CA)	Developing microfluidics to deliver reagents and samples to its electronic DNA hybridization chips

### 1.2.2 Challenges and Outlooks

While it is clear that LOC systems possess many advantages, producing a commercial LOC system that can readily be used to replace a conventional chemical lab or macro system is surely not an easy task. Some of the major challenges include: 1) on-chip sample preparation, 2) world-to-chip interfacing, 3) on-chip optical detection, and 4) on-chip components integration.

On-chip sample preparation turns out to be an extremely challenging task for all LOC systems. Before any analysis, impurities in the raw sample (underground water, sea water, blood, urine, saliva, etc.) need to be removed so that the target composition can be appropriately processed and analyzed. Those impurities can be dirt particles, cells, proteins, ions, or others. While this sample purification task might be straightforward for manual processing in a conventional chemical lab, it is extremely difficult to carry out on LOC systems. Different impurities require different procedures and facilities to remove and therefore sample preparation needs to be handled on a case by case basis. Trace level impurities that stays with the sample might interfere the sensing of sample species and jeopardize the quantification accuracy and reproducibility. Two reviews on sample preparation in microfluidic systems are given in [35, 36].

Let's assume that raw samples are processed off-chip by conventional procedures and are ready for analysis, the next problem is to deliver/couple the processed samples, reagents, and conventional macro-scale tubing to the LOC system. This procedure is often referred to as "world-to-chip interfacing," which remains a challenging issue for LOC. For example, the sample volume processed in the LOC system can be as small as 1 nL, but it is extremely difficult to precisely deliver this small volume of sample to the

LOC system using the macro tubing and pumps where a fluidic swept/dead volume of a few  $\mu\text{L}$  can be easily found. Also, in the case of high pressure LOC applications such as liquid chromatography, world-to-chip interfacing needs to withstand operational pressure as high as 1,000 psi without leaking or fracture. Any fluidic leak rate larger than 10 nL/min can significantly degrade the overall LOC performance. Therefore, robust and small-swept-volume world-to-chip interfacing technology needs to be developed [37].

Optical detection such as UV absorption and laser-induced fluorescence detection are frequently used sensing tools in chemistry and biology for a broad range of analytes. The limit of detection (LOD) of optical detection is defined by the minimum sensible amount of photons that are collected by the photo detector per unit time. For the microfluidic system, since the sample volume is much smaller than the macrofluidic system, it can be expected that its lowest sensible analyte concentration will be much higher than that of macrofluidic system. To compensate for this drawback, techniques to increase on-chip optical path or analyte concentration need to be developed. Furthermore, many of today's optical detection setups for LOC are still using off-chip light sources and detectors. This introduces complexities in optical alignments between the on-chip microfluidic cell and off-chip optical components. To avoid the alignment issue, light source and detectors need to be fabricated on the chip, which can be quite challenging as well.

Finally, most of the developments in LOC so far have been focused on discrete devices, such as channels, valves, pumps, flow sensors, pressure sensors, and electrochemical sensors, etc. To realize a complete LOC concept, however, all necessary functional components should be integrated in a single process and fabricated on a single

chip. It is understandable that the more components to be integrated on a chip the more difficult and likely lower-yield the process will be. Well, the multichip module (MCM) approach [38] is surely an alternative to be used for complicated systems. The major advantage of it is that the fabrication process for each chip will be much simpler and each component of the system can be designed or replaced individually with maximum flexibility. However, the MCM approach also introduces complexities such as microfluidic coupling between chips. A major goal of this thesis is to demonstrate with real examples (microchip HPLC systems) that reliable MEMS processes can be designed to achieve extensive components integration for LOC applications.

### 1.3 Parylene as a Microstructure Material

#### 1.3.1 Introduction to Parylene

Parylene (poly-para-xylylene) was discovered in 1947 and commercialized by Union Carbide Corporation in 1965. Parylene has been used in several industries because of its unique properties. One of its primary applications is PCB (printed circuit board) coating for the electronics industry, where parylene coating isolates the delicate electronic devices from moisture and corrosive environments. Figure 1-7 shows the chemical structures of the three most frequently used parylene types: parylene N, parylene C, and parylene D.



Figure 1-7: Chemical structures of parylene N, C, and D.

Figure 1-8 shows the parylene deposition procedures, the involved chemical processes, and the instrument. The process starts with placing parylene dimer (di-para-xylylene), a stable compound in granular form, into the vaporizer. The substrate to be coated with parylene is put into the deposition chamber. The whole system is then pumped down to medium vacuum (8-10 mTorr). The dimer is heated in the vaporizer and sublimed into vapor at around 170 °C. The dimer vapor enters the pyrolysis furnace that is maintained at 690 °C, where the dimers are cleaved into identical monomers (para-xylylene). In the room-temperature deposition chamber, the monomers reunite on all exposed surfaces in the form of polymers (poly-para-xylylene). Deposition chamber pressure is around 23 mTorr. Additional components of the system include a mechanical vacuum pump and associated cold trap to take away extra monomer vapor. Although parylene N structure is used in Figure 1-8, the deposition process is almost identical for all three common types of parylene, except for some slight differences in pyrolysis temperature and deposition pressure.

Typical parylene coating thickness in a single deposition run ranges from 0.1 to 20 microns. Sub-micron parylene deposition is trickier because thickness uniformity can be a concern. In general, the coating thickness is in proportion to the amount of dimer used. Chamber condition including cleanness, base pressure, and temperature fluctuation can result in a slight deposition rate change. The normal deposition rate of parylene C under a deposition vapor pressure of 23 mTorr is about 5  $\mu\text{m}$  per hour. The deposition rate is directly proportional to the square of the monomer concentration in the chamber and inversely proportional to the absolute temperature of the substrate on which parylene will be coated [39].

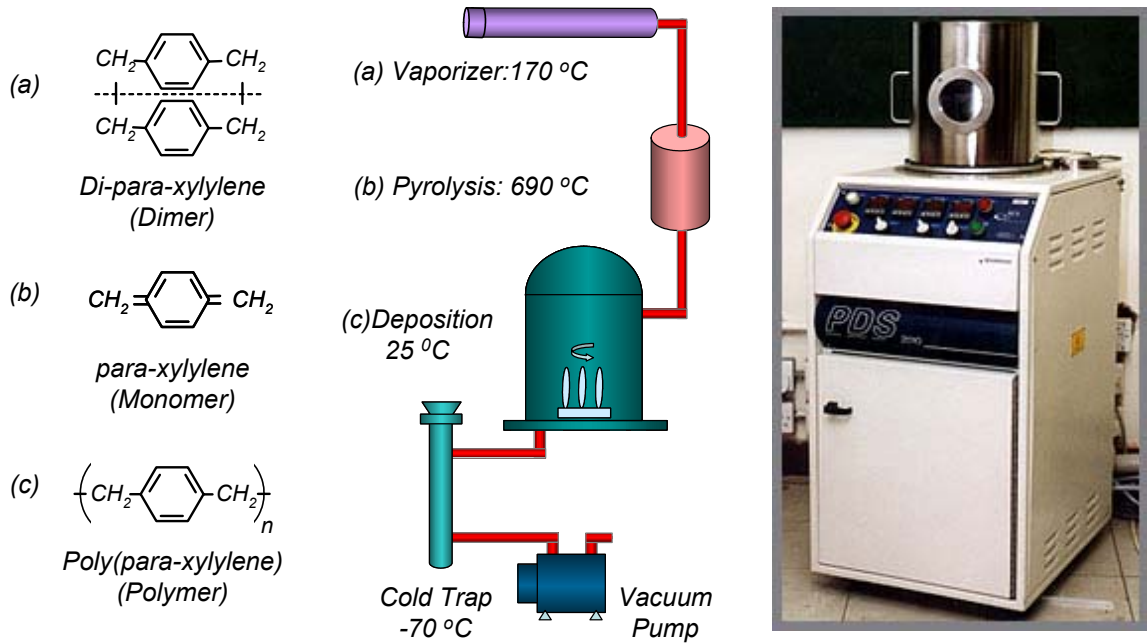


Figure 1-8: Parylene deposition system and the involved chemical processes.

Since parylene thin film is deposited using chemical vapor deposition (CVD), the deposited film is highly conformal. As mentioned earlier, parylene is an excellent barrier to gas and moisture. Compared with PDMS (polydimethylsiloxane), which is another popular material for microfluidic devices, the gas permeability of parylene is more than four orders of magnitude smaller and moisture permeability is ten times smaller. Parylene is extremely inert to most chemicals and solvents used in chemical or biological laboratories. Manufacturer's study [40] shows that solvents have a minor swelling effect on parylene N, C, and D with a 3% maximum increase in film thickness. The swelling is completely reversible after the solvents are removed from parylene by vacuum drying. Furthermore, parylene is biocompatible (USP Class VI), which makes it a good candidate material for making long-term human implants or biomimetic components.

As for mechanical properties, parylene has an elongation break of 200%. This mechanical flexibility makes it a durable material for composing MEMS microfluidic and actuation devices. Parylene is also an excellent electrical and thermal insulator. The electrical breakdown voltage of a 1- $\mu\text{m}$ -thick parylene layer is over 200 volts. The room temperature thermal conductivity of parylene C (0.84 mW/cm-K) is only three times as big as static air (0.30 mW/cm-K). In terms of optical properties, parylene is pretty much transparent in the visible light range. However, parylene begins to absorb light with wavelength shorter than 280 nm significantly, which limits some of its UV applications.

The difference in chemical structures between parylene N, C, and D as shown in Figure 1-7 actually results in different thin-film properties. For example, parylene N has the lowest gas/moisture permeability. However, parylene N also has the lowest deposition rate which is not favorable in a mass production process. In terms of choosing a micromachining material from the three parylene species, parylene C has a good combination of electrical and physical properties plus a low permeability to moisture and other corrosive gases. Parylene C also has higher deposition rate than parylene N, and D. Therefore, parylene C is often chosen to fabricate microstructures. In our lab, parylene C was chosen 99% of the time to build devices and the deposition parameters have been well characterized so to guarantee good thin film qualities which include film transparency, thickness uniformity/accuracy, and adhesion properties to assorted substrates. Parylene C was as well used exclusively in this thesis to build devices.

Detailed electrical, mechanical, thermal, optical, and other properties can be found on a parylene vendor's website [39]. A list of selected properties for parylene N, C, and D is shown in Table 1-4.

Table 1-4: Properties for parylene N, C, and D.

	Parylene N	Parylene C	Parylene D
Breakdown Voltage (V) for 1 $\mu\text{m}$ Film	276	220	217
Dielectric Constant at 1 kHz	2.65	3.10	2.82
Volume Resistivity ( $\times 10^{16}$ $\Omega \cdot \text{cm}$ )	14	8.8	12
Young's Modulus (GPa)	2.42	2.76	2.62
Density ( $\text{g}/\text{cm}^3$ )	1.1	1.3	1.4
Index of Refraction	1.66	1.64	1.67
Strong UV Absorption (nm)	< 280	< 280	NA
Water Absorption (% after 24 hours)	< 0.1	< 0.1	< 0.1
Melting Temperature ( $^{\circ}\text{C}$ )	420	290	380
Glass Transition Temperature ( $^{\circ}\text{C}$ )	NA	80–100	NA
Linear Coefficient of Expansion ( $\text{ppm}/^{\circ}\text{C}$ )	69	35	30–80
Thermal Conductivity at 25 $^{\circ}\text{C}$ ( $\text{mW}/(\text{cm}\cdot\text{K})$ )	1.26	0.84	NA

### 1.3.2 Applications of Parylene Thin Film in MEMS

As mentioned in the previous section, parylene thin film is deposited using a room temperature CVD process that makes parylene deposition a post-CMOS compatible process. Besides, parylene thin film can be easily patterned using a conventional lithography process plus oxygen plasma etching (with photoresist or metal as the mask). Combining with other MEMS surface micromachining technologies introduced earlier, one can build assorted microstructures using parylene as the structural material. The conformal coating characteristics of parylene and its mechanical robustness make it a favorable structural material and technology in microfluidics. Parylene microfluidic devices such as channels, pumps, valves, filters, pressure and flow sensors, mass flow controllers, electrospray nozzles, and gas chromatography columns have been successfully demonstrated (Figure 1-9) [41-46]. It is also verified in those examples that

parylene technology provides a straightforward process solution for integrating various microfluidic components on a single chip. Moreover, the bio-compatibility of parylene makes it a perfect material for building biological sensing or implantable devices [47].

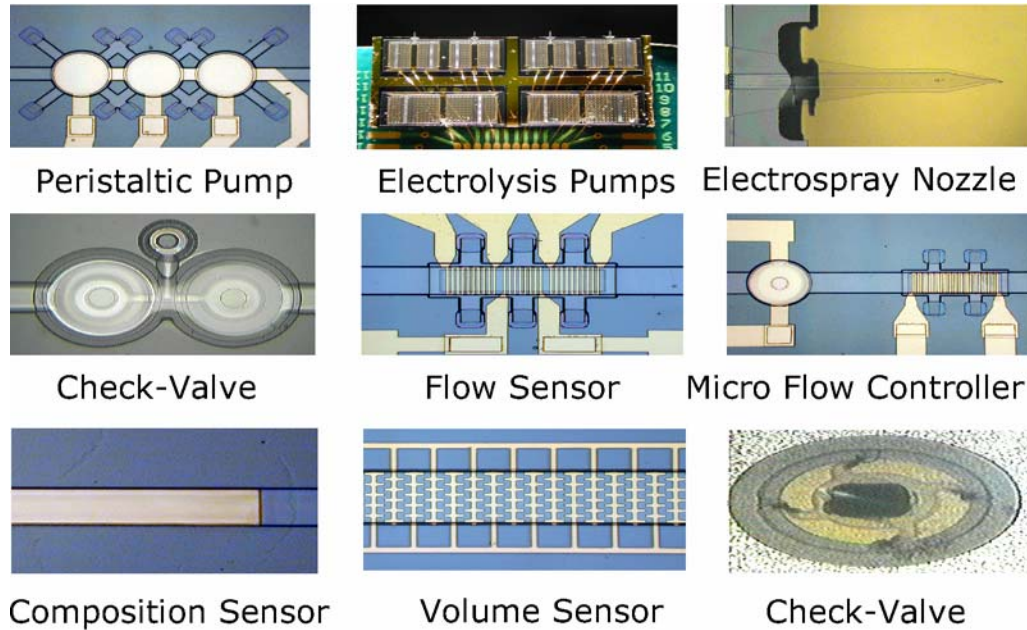


Figure 1-9: Parylene microfluidic devices.

In this thesis, parylene technology is explored thoroughly to build MEMS lab-on-a-chip high-performance liquid chromatography (HPLC) system. Parylene technology is chosen here mainly due to its great chemical resistance, mechanical robustness, optical transparency, and its ease of process integration, which are all crucial factors in making a reliable and fully functional microchip HPLC system.

## 1.4 Bibliography

- [1] K. E. Petersen, "Silicon as a mechanical material," *Proceedings of the IEEE*, vol. 70, pp. 420-457, 1982.
- [2] G. T. A. Kovacs, N. I. Maluf, and K. E. Petersen, "Bulk micromachining of silicon," *Proceedings of the IEEE*, vol. 86, pp. 1536-1551, 1998.
- [3] H. Robbins and B. Schwartz, "Chemical Etching of Silicon 2. The System HF, HNO<sub>3</sub>, H<sub>2</sub>O, and CH<sub>3</sub>COOH," *Journal of the Electrochemical Society*, vol. 107, pp. 108-111, 1960.
- [4] H. F. Winters and J. W. Coburn, "Etching of Silicon with XeF<sub>2</sub> Vapor," *Applied Physics Letters*, vol. 34, pp. 70-73, 1979.
- [5] D. E. Ibbotson, J. A. Mucha, D. L. Flamm, and J. M. Cook, "Plasmaless Dry Etching of Silicon with Fluorine-Containing Compounds," *Journal of Applied Physics*, vol. 56, pp. 2939-2942, 1984.
- [6] X. Q. Wang, X. Yang, K. Walsh, and Y. C. Tai, "Gas phase silicon etching with bromine trifluoride," presented at 9th International Conference on Solid-State Sensors and Actuators (Transducers '97), Chicago, USA, 1997.
- [7] C. Y. Shih, T. A. Harder, and Y. C. Tai, "Yield strength of thin-film parylene-C," *Microsystem Technologies*, vol. 10, pp. 407-411, 2004.
- [8] T. J. Yao, X. Yang, and Y. C. Tai, "BrF<sub>3</sub> dry release technology for large freestanding parylene microstructures and electrostatic actuators," *Sensors and Actuators a-Physical*, vol. 97-8, pp. 771-775, 2002.
- [9] K. E. Bean, "Anisotropic Etching of Silicon," *IEEE Transactions on Electron Devices*, vol. 25, pp. 1185-1193, 1978.

- [10] K. R. Williams and R. S. Muller, "Etch rates for micromachining processing," *Journal of Microelectromechanical Systems*, vol. 5, pp. 256-269, 1996.
- [11] U. Schnakenberg, W. Benecke, and B. Lochel, "Nh4Oh-Based Etchants for Silicon Micromachining," *Sensors and Actuators A-Physical*, vol. 23, pp. 1031-1035, 1990.
- [12] S. A. McAuley, H. Ashraf, L. Atabo, A. Chambers, S. Hall, J. Hopkins, and G. Nicholls, "Silicon micromachining using a high-density plasma source," *Journal of Physics D-Applied Physics*, vol. 34, pp. 2769-2774, 2001.
- [13] M. Last and K. Pister, "2DOF actuated micromirror designed for large DC deflection," presented at the 3rd International Conference on Micro Opto Electro Mechanical Systems (MOEMS '99), Mainz, Germany, 1999.
- [14] E. Spiller, R. Feder, J. Topalian, E. Castellani, L. Romankiw, and M. Heritage, "X-Ray Lithography for Bubble-Devices," *Solid State Technology*, vol. 19, pp. 62, 1976.
- [15] E. W. Becker, W. Ehrfeld, D. Munchmeyer, H. Betz, A. Heuberger, S. Pongratz, W. Glashauser, H. J. Michel, and R. Vonsiemens, "Production of Separation-Nozzle Systems for Uranium Enrichment by a Combination of X-Ray Lithography and Galvanoplastics," *Naturwissenschaften*, vol. 69, pp. 520-523, 1982.
- [16] M. Shimbo, K. Furukawa, K. Fukuda, and K. Tanzawa, "Silicon-to-Silicon Direct Bonding Method," *Journal of Applied Physics*, vol. 60, pp. 2987-2989, 1986.
- [17] T. R. Anthony, "Anodic Bonding of Imperfect Surfaces," *Journal of Applied Physics*, vol. 54, pp. 2419-2428, 1983.

- [18] J. Brook and R. Dandliker, "Submicrometer Holographic Photolithography," *Solid State Technology*, vol. 32, pp. 91-94, 1989.
- [19] E. B. Guitrau, *The EDM Handbook*, 1997.
- [20] R. Srinivasan and V. Maynebantou, "Self-Developing Photoetching of Poly(Ethylene-Terephthalate) Films by Far Ultraviolet Excimer Laser-Radiation," *Applied Physics Letters*, vol. 41, pp. 576-578, 1982.
- [21] P. Haggmann, W. Ehrfeld, and H. Vollmer, "Fabrication of microstructures with extreme structural heights by reaction injection molding," presented at the 1st Meeting of the European Polymer Federation, European Symposium on Polymeric Materials, Lyon, France, 1987.
- [22] M. P. Maher, J. Pine, J. Wright, and Y. C. Tai, "The neurochip: a new multielectrode device for stimulating and recording from cultured neurons," *Journal of Neuroscience Methods*, vol. 87, pp. 45-56, 1999.
- [23] R. P. Feynman, "There's plenty of room at the bottom," *Journal of Microelectromechanical Systems*, vol. 1, pp. 60-66, 1992.
- [24] H. C. Nathanson, W. E. Newell, R. A. Wickstrom, and J. J. R. Davis, "The resonant gate transistor," *IEEE Trans. Electron Devices*, vol. 14, pp. 117- 133, 1967.
- [25] L.-S. Fan, Y.-C. Tai, and R. S. Muller, "IC-processed electrostatic micromotors," *Sensors and Actuators*, vol. 20, pp. 41-47, 1989.
- [26] Y.-C. Tai and R. S. Muller, "IC-processed electrostatic synchronous micromotors," *Sensors and Actuators*, vol. 20, pp. 49-55, 1989.

- [27] M. J. Madou, *Fundamentals of Microfabrication*, 2nd ed. New York: CRC Press, 2002.
- [28] Editors, "Market forecast sees 25% CAGr in MST in 2004," *Micromachine Devices*, vol. 5, pp. 12, 2000.
- [29] NEXUS, "NEXUS market analysis for MEMS and Microsystems III, 2005-2009," 2005.
- [30] J. Xie, Y. N. Miao, J. Shih, Q. He, J. Liu, Y. C. Tai, and T. D. Lee, "An electrochemical pumping system for on-chip gradient generation," *Analytical Chemistry*, vol. 76, pp. 3756-3763, 2004.
- [31] S. C. Terry, J. H. Jerman, and J. B. Angell, "Gas-Chromatographic Air Analyzer Fabricated on a Silicon-Wafer," *IEEE Transactions on Electron Devices*, vol. 26, pp. 1880-1886, 1979.
- [32] D. R. Reyes, D. Iossifidis, P. A. Auroux, and A. Manz, "Micro total analysis systems. 1. Introduction, theory, and technology," *Analytical Chemistry*, vol. 74, pp. 2623-2636, 2002.
- [33] P. A. Auroux, D. Iossifidis, D. R. Reyes, and A. Manz, "Micro total analysis systems. 2. Analytical standard operations and applications," *Analytical Chemistry*, vol. 74, pp. 2637-2652, 2002.
- [34] T. Vilknér, D. Janásek, and A. Manz, "Micro Total Analysis Systems. Recent Developments," *Analytical Chemistry*, vol. 76, pp. 3373-3386, 2004.
- [35] A. J. de Mello and N. Beard, "Dealing with 'real' samples: sample pre-treatment in microfluidic systems," *Lab on a Chip*, vol. 3, pp. 11N-19N, 2003.

- [36] J. Lichtenberg, N. F. de Rooij, and E. Verpoorte, "Sample pretreatment on microfabricated devices," *Talanta*, vol. 56, pp. 233-266, 2002.
- [37] Q. He, C. Pang, Y. C. Tai, and T. D. Lee, "Ion liquid chromatography on-a-chip with beads-packed parylene column," presented at the 17th IEEE International Conference on MicroElectroMechanical Systems (MEMS 2004), Maastricht, The Netherlands, 2004.
- [38] S. Linder, H. Baltes, F. Gnaedinger, and E. Doering, "Fabrication technology for wafer through-hole interconnections and three-dimensional stacks of chips and wafers," presented at the 7th IEEE International Conference on Micro Electro Mechanical Systems (MEMS 1994), Oiso, Japan, 1994.
- [39] [http://www.scscookson.com/parylene\\_knowledge/specifications.cfm](http://www.scscookson.com/parylene_knowledge/specifications.cfm)
- [40] Specialty Coating Systems, "Solvent resistance of the parylene." Trade literature.
- [41] L. Licklider, X. Q. Wang, A. Desai, Y. C. Tai, and T. D. Lee, "A micromachined chip-based electrospray source for mass spectrometry," *Analytical Chemistry*, vol. 72, pp. 367-375, 2000.
- [42] J. Xie, Y. Miao, J. Shih, Q. He, J. Liu, Y. C. Tai, and T. D. Lee, "An Electrochemical Pumping System for On-Chip Gradient Generation," *Analytical Chemistry*, vol. 76, pp. 3756-3763, 2004.
- [43] H. S. Noh, P. J. Hesketh, and G. C. Frye-Mason, "Parylene gas chromatographic column for rapid thermal cycling," *Journal of Microelectromechanical Systems*, vol. 11, pp. 718-725, 2002.

- [44] X. Q. Wang and Y. C. Tai, "Normally closed in-channel micro check valve," presented at the 13th IEEE International Conference on Micro Electro Mechanical Systems (MEMS 2000), Miyazaki, Japan, 2000.
- [45] J. Xie, X. Yang, X. Q. Wang, and Y. C. Tai, "Surface micromachined leakage proof parylene check valve," presented at the 14th IEEE International Conference on Micro Electro Mechanical Systems (MEMS 2001), Interlaken, Switzerland, 2001.
- [46] J. Xie, J. Shih, and Y. C. Tai, "Integrated surface-micromachined mass flow controller," presented at the 16th IEEE International Conference on Micro Electro Mechanical Systems (MEMS 2003), Kyoto, Japan, 2003.
- [47] D. C. Rodger and Y. C. Tai, "Microelectronic packaging for retinal prostheses," *IEEE Engineering in Medicine and Biology Magazine*, vol. 24, pp. 52-57, 2005.

---

# CHAPTER 2

---

## EVOLUTION of HPLC TECHNOLOGY

### 2.1 High-Performance Liquid Chromatography

#### 2.1.1 Introduction

High-Performance Liquid Chromatography (HPLC) is one of the most powerful analysis tools widely used in fields such as the pharmaceutical industry, food industry, chemistry, biology, forensic analysis, and clinical analysis. HPLC provides separation, identification, purification, and quantification of chemical compounds such as proteins, peptides, ions, polymers, and amino acids as long as samples can be prepared in the solution format.

Chromatography in general includes all separation techniques in which analytes partition between different phases that move relative to each other. In most chromatographic techniques, one phase is stationary and the other phase is mobile. If the mobile phase is liquid, then the chromatographic technique is called Liquid

Chromatography (LC). The LC stationary phase is solid or porous with a specific surface property. The surface property of the stationary phase can be adjusted by bonding molecules with desirable chemical functional groups to its surface. HPLC means LC techniques that use a packed bed of stationary phase composed of particles with dimensions smaller than 10  $\mu\text{m}$ . The small particle size creates a large stationary-phase surface which dramatically enhances the chromatography efficiency. The densely packed HPLC column also requires an elevated backpressure to push the mobile phase forward and therefore HPLC is also called high-pressure liquid chromatography.

The chromatography procedures start with sample injection to the separation column. Sample molecules adsorb to the stationary phase in the beginning section of the column and form a narrow sample band. The mobile phase is then injected to elute sample molecules out of the column. Due to the fact that different sample molecules have different adsorption strengths to the stationary phase, molecules will migrate in the column with different speeds and exit the column at different times. A sensor located at the outlet of the separation column is used to quantitatively sense the eluted sample peaks and the output data of the sensor is used to plot chromatograms. This process is illustrated in Figure 2-1.

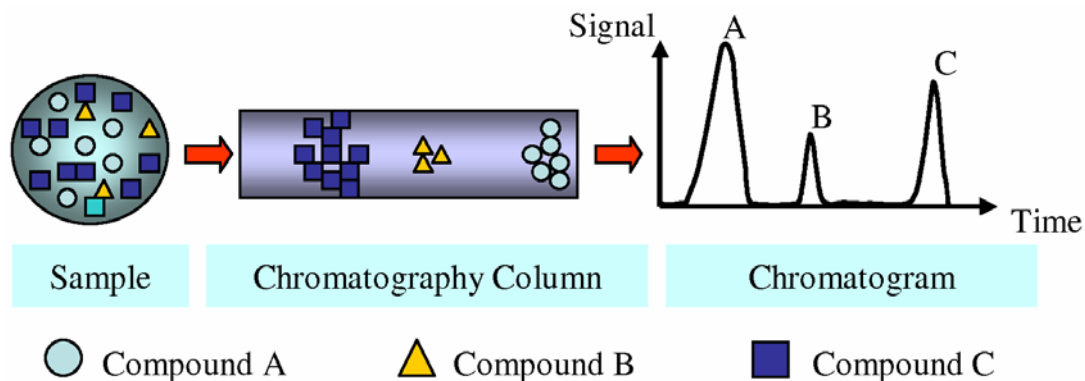


Figure 2-1: Illustration of the chromatographic separation process.

If the mobile phase chemical composition is constant throughout the elution, the elution process is called isocratic elution. Obviously, isocratic elution is most straightforward to carry out compared with other elution strategies where mobile phase conditions change throughout the elution process. However, when a sample mixture contains tens of compounds or more, isocratic elution can be problematic. Early peaks can crowd together with poor peak resolution and late peaks are broad in shape and can take a long time to elute. Using a mobile phase with weaker elution strength can improve early peaks resolution since elution time of each peak will be longer and so are the differences of elution times among peaks. Using a mobile phase with stronger elution strength, on the other hand, can shorten the elution times of the late peaks. Therefore, by starting the elution with a weak mobile phase and gradually increasing the mobile-phase elution strength over the separation process, the chromatography performance can be significantly improved. This elution strategy is called gradient elution. Depending on the elution mechanisms, a gradient elution can be generated by changing the mobile phase parameters such as salt concentration, water/organic solvent ratio, temperature or, pH values over time.

### **2.1.2 History**

The discovery of liquid chromatography can be traced back to 1903 when the Russian botanist Mikhail Twsett (1872-1919) observed that colored plant pigments could be separated on a chalk column where ether was run through as the mobile phase (Figure 2-2) [1]. The separation of pigments appeared as colored bands on the column, which was why he named this technique “chromatography.”

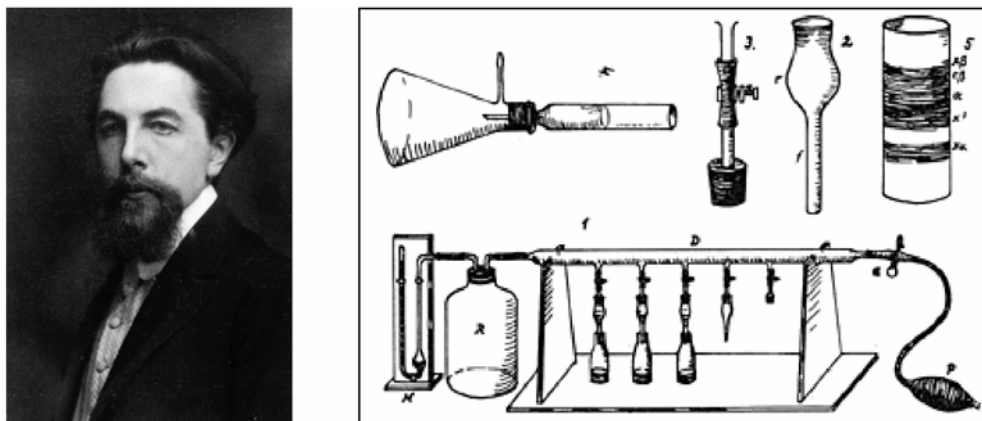


Figure 2-2: The inventor of chromatography, Twsett, and his chromatographic device.

In 1941, Martin and Synge developed the theoretical background for partition chromatography and used mathematical formulae to describe the separation process [2], for which they were awarded the Nobel Prize in chemistry (1952). The development of the open-column chromatography in the 1940s and thin-layer chromatography in the 1950s greatly improved the speed and resolution of LC, but there were still serious limitations compared to modern LC methods in terms of resolution and quantitative analysis capability. By the late 1960s, LC theories and instrumentation were well-established, which led to the first commercially available liquid chromatography system in 1969. In 1973, due to the advances in stationary phase fabrication and packing technologies, high-efficiency columns could be prepared with particle diameters smaller than 10  $\mu\text{m}$  and reproducible separations were achievable. In the same year, modification of silica surfaces via silanization became commercially available. These breakthroughs led to the birth of the first commercial 10  $\mu\text{m}$  reversed-phase HPLC column [3]. Since then, HPLC has grown to become one of the most important analytical tools in chemistry/biology laboratories.

### 2.1.3 Theory

#### 2.1.3.1 Analyte Retention and Chromatogram

Each peak in a chromatogram represents the elution of an analyte species. According to the theory [4], an ideal peak should have a Gaussian curve. The height and area of a peak are proportional to the concentration and total number of molecules of that analyte species in the injected sample, respectively.

The retention time of a peak  $t_R$  is defined as the time length from the beginning of sample injection to the time that peak maximum occurs in the chromatogram as shown in Figure 2-3. The breakthrough time  $t_0$  is defined as the time that the mobile phase takes to travel through the column. If the column length is  $L_c$  and the mobile phase linear flow velocity is  $u$ , then:

$$t_0 = \frac{L_c}{u} \quad (2.1)$$

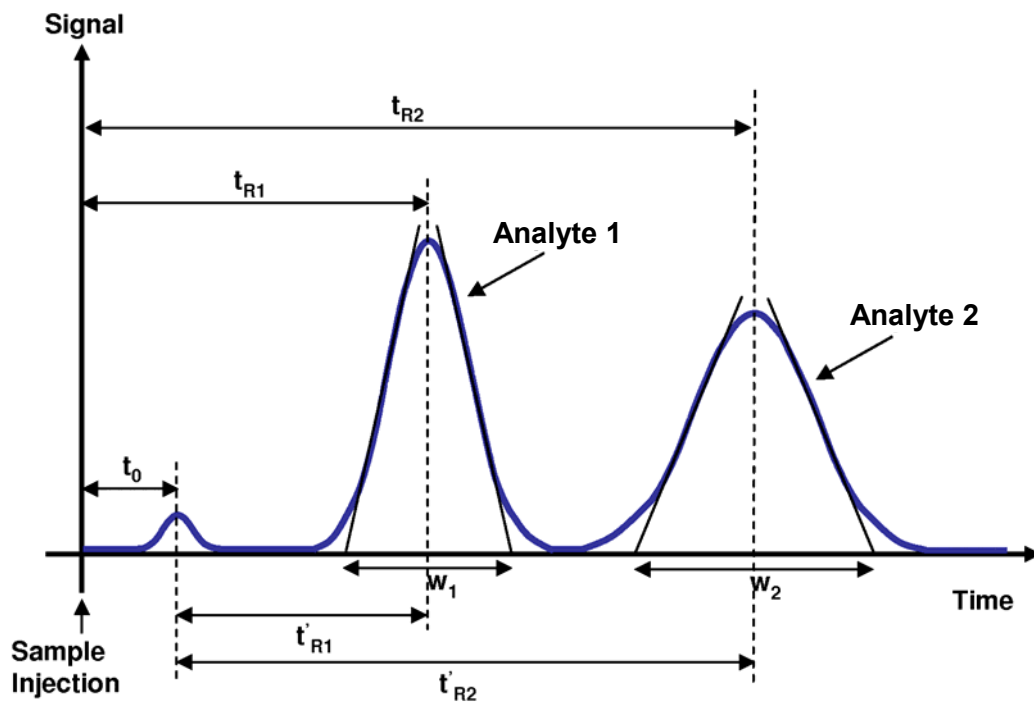


Figure 2-3: Chromatogram and its characteristic features [4].

The mobile phase volumetric flow rate  $F$  is:

$$F = \varepsilon u A_c \quad (2.2)$$

where  $A_c$  is the column cross-sectional area and  $\varepsilon$  is the column porosity. For cylindrical columns with an inner diameter (ID) of  $d_c$ :

$$A_c = \frac{\pi d_c^2}{4} \quad (2.3)$$

The column porosity  $\varepsilon$  is:

$$\varepsilon = \frac{V_{column} - V_{packing}}{V_{column}} \quad (2.4)$$

where  $V_{column}$  is the total volume inside the column and  $V_{packing}$  is the volume occupied by the solid packing material in the column.

As shown in Figure 2-3,  $t'_R$  is the net/adjusted retention time relative to  $t_0$ :

$$t'_R = t_R - t_0 \quad (2.5)$$

$t_0$ , as defined earlier, also represents the time an analyte spends in the mobile phase, which is identical for all analytes assuming all analytes move at speed  $u$  when they are in the mobile phase.  $t'_R$  represents the time an analyte spends in the stationary phase. The longer an analyte stays in the stationary phase, the later it will be eluted. Ideally, any two analytes can be separated and resolved from each other using liquid chromatography techniques as long as their retention times are different and if the separation column is long enough.

The retention factor  $k$  of an analyte is defined as:

$$k \equiv \frac{t'_R}{t_0} = \frac{t_R - t_0}{t_0} \quad (2.6)$$

To characterize an analyte, the retention factor  $k$  is preferred over the retention time, because the retention time depends on column length and mobile-phase flow velocity while retention factor does not. The retention factor is the ratio of the time that an analyte spends in the stationary phase to the time it spends in the mobile phase, which is also the ratio of the number of analyte molecules that are at any time in/on the stationary phase  $N_S$  to the number of analyte molecules that are in the mobile phase  $N_M$ :

$$k = \frac{N_S}{N_M} \quad (2.7)$$

This equation enables us to make the link between the retention factor of an analyte and the thermodynamics of the separation, which will be discussed as follows.

From equation (2.7), we can relate the numbers of molecules in the stationary phase and in the mobile phase to their respective concentrations  $c_M$  and  $c_S$ :

$$k = \frac{N_S}{N_M} = \frac{c_S V_S}{c_M V_M} \quad (2.8)$$

where  $V_M$  and  $V_S$  are the volumes of the mobile phase and stationary phase, respectively.

Their ratio is called the phase ratio  $\beta$ :

$$\beta \equiv \frac{V_S}{V_M} \quad (2.9)$$

The ratio of the concentrations  $c_S$  and  $c_M$  is the partition coefficient  $K$ :

$$K \equiv \frac{c_S}{c_M} \quad (2.10)$$

Therefore the retention factor is the product of the phase ratio and the partition coefficient:

$$k = \beta K \quad (2.11)$$

We also know the relationship between the partition coefficient (equilibrium constant) and the standard Gibbs free-energy change  $\Delta G_0$  associated with this chemical equilibrium ( $\Delta G=0$ ):

$$\Delta G_0 = -RT \ln K \quad (2.12)$$

Therefore, by combining (2.11) and (2.12), the logarithm of the retention factor is a function of the free energy [5]:

$$\ln k = -\frac{\Delta G_0}{RT} + \ln \beta = -\frac{\Delta H_0}{RT} + \frac{\Delta S_0}{R} + \ln \beta \quad (2.13)$$

where  $\Delta H_0$  and  $\Delta S_0$  are the standard enthalpy and entropy changes associated with the transfer of the analyte molecules from the mobile phase to the stationary phase,  $R$  is the gas constant, and  $T$  is the absolute temperature.

The relative retention  $\alpha$  is defined as the ratio of the retention factors of two analytes:

$$\alpha \equiv \frac{k_2}{k_1} = \frac{K_2}{K_1} \quad (2.14)$$

The retention factor of the later-eluting analyte is in the numerator, making the value always larger than one. The relative retention is purely a chemical or thermodynamic entity that does not depend on the physical parameters of the column anymore. One can use it to verify whether the chemistry of a separation remains invariant when transferring the separation from one column to another.

Now we discuss the definition of chromatography peak resolution  $R_S$ . As shown in Figure 2-3,  $w$  is the peak width. When measured at 13.4% of the height of a Gaussian peak,  $w$  equals four times of the standard deviation  $\sigma$  of the peak. The resolution  $R_S$  of

two peaks is defined as the ratio of the two-peak maxima distance to the mean of the two peak widths:

$$R_S \equiv \frac{t_{R2} - t_{R1}}{\frac{1}{2} \cdot (w_1 + w_2)} \quad (2.15)$$

Even though in (2.15) the peak resolution is defined and calculated in the time domain, the peak resolution can as well be defined and calculated in the space domain. In that case, resolution is the ratio of the two-peak maxima distance measured in length units to the mean of the peak widths measured in length units. In reality, the distance between the maximums of two peaks increases with the length that they have migrated in the column while the widths of the peaks increase only with the square root of this length. Therefore, chromatographic resolution increases with the square root of the distance traveled by the peaks [4].

### 2.1.3.2 Height Equivalent to a Theoretical Plate

The height equivalent to a theoretical plate (HETP),  $H$ , can be treated as the distance over which a chromatographic equilibrium cycle is achieved. The smaller the  $H$  value, the higher the column efficiency.

As mentioned earlier, chromatographic band (peak) width is proportional to its Gaussian distribution standard deviation  $\sigma$ . Because  $\sigma$  (in space domain) increases with the square root of the length a peak has traveled in the column,  $L$ , the peak variance  $\sigma^2$  increases linearly with the length it has traveled. The smaller the slope of  $\sigma^2$  vs.  $L$  plot, the slower the peak widens and therefore the higher the column efficiency. In other

words, one can use shorter column length to achieve complete separation of two peaks.

The slope mentioned above (variance per unit length) is defined to be the HETP or  $H$ :

$$H \equiv \frac{\sigma^2}{L} \quad (2.16)$$

The number of theoretical plates (or plate count)  $N$  is calculated by dividing the column length  $L_c$  by  $H$ :

$$N \equiv \frac{L_c}{H} = \frac{L_c^2}{\sigma_c^2} \quad (2.17)$$

where  $\sigma_c$  is the peak standard deviation (in space domain) at the end of the column. In practice, plate count  $N$  can be calculated conveniently from the chromatogram:

$$N = 16 \left( \frac{t_R}{w} \right)^2 \quad (2.18)$$

The plate count  $N$  is a measure of the quality of a separation that is based on a single peak. The plate count obtained from a non-retained peak is a measure of the column packing efficiency. From (2.17) it is clear that higher  $N$  or higher separation capability can be obtained using a longer column or reducing the peak variance. Approaches to reduce peak variance or the band-broadening effect will be discussed in 2.1.3.4.

### 2.1.3.3 Reduced/Dimensionless Parameters

The concepts of reduced/dimensionless parameters such as reduced plate height or reduced velocity are powerful ideas that allow us to compare columns to each other under a broad range of mobile-phase conditions and over a range of stationary-phase particle sizes. The reduced plate height,  $h$ , is defined as:

$$h \equiv \frac{H}{d_p} \quad (2.19)$$

where  $d_p$  is the stationary-phase particle diameter.  $h$  represents the number of layers of stationary-phase particle packing over which a complete chromatographic equilibrium cycle is obtained. A column with good stationary-phase packing usually has an  $h$  value from 2 to 5. The reduced velocity  $v$  is defined as:

$$v \equiv \frac{ud_p}{D_M} \quad (2.20)$$

where  $D_M$  is the analyte diffusion coefficient in the mobile phase.

One of the most frequently used reduced/dimensionless parameters is the dimensionless flow resistance  $\Phi$ , which is used to replace permeability:

$$\Phi \equiv \frac{\Delta P d_p^2}{L_c \eta u} \quad (2.21)$$

where  $\Delta P$  is the pressure drop across the column length,  $\eta$  is the mobile phase viscosity.  $\Phi$  is between 500 (spherical beads) and 1,000 (irregular beads) for slurry-packed columns containing totally porous particles and about 300 if non-porous particles are used [6]. A much greater value of  $\Phi$  (say 5,000) indicates a blockage somewhere in the flow path. This equation can also be rearranged to estimate column backpressure:

$$\Delta P = \frac{\Phi L_c \eta u}{d_p^2} \quad (2.22)$$

#### 2.1.3.4 Band-Broadening Phenomenon

All chromatographic bands or peaks will continue to broaden as the bands move down the column as mentioned earlier. Any band-broadening phenomenon will result in

a larger plate height and or lower column separation efficiency. Therefore, it is important to understand the mechanisms of band-broadening and minimize it in the chromatography system. Four main mechanisms that cause band-broadening in a chromatography process will be discussed in the following.

The first mechanism is eddy diffusion (Figure 2-4 (a)). The separation column is packed with stationary-phase particles and the mobile phase passes through the stationary phase and transports sample molecules with it. Some sample molecules are “lucky” and travel roughly a straight line through the chromatographic bed without much interaction with the stationary phase. They leave the column before most of the others. Other sample molecules (of the same species) leave the column later since they have undergone several diversions and more interaction with the stationary phase along the way.

The second mechanism is flow velocity distribution of the mobile phase. The mobile phase passes in a laminar flow pattern between the stationary-phase particles (Figure 2-4 (b)). The flow is faster in the path center than it is near the particle surfaces. To reduce the band-broadening caused by eddy diffusion and flow velocity distribution, the stationary-phase packing should be composed of particles with as narrow a size distribution as possible. The ratio between the largest and the smallest particle diameters should not exceed 2. Besides, packing with smaller sized particles can reduce gap size between particles and therefore reduce band-broadening from eddy diffusion and flow velocity distribution. The band-broadening effect caused by eddy diffusion and flow velocity distribution is barely affected by the mobile-phase linear flow velocity.

The third mechanism of band-broadening is sample molecule longitudinal diffusion in the mobile phase (Figure 2-4 (c)). Band-broadening caused by this

longitudinal diffusion is significant when small particles ( $< 10 \mu\text{m}$ ) are used, or mobile-phase velocity is low, or the sample molecule diffusion coefficient in the mobile phase is relatively large. This effect can be minimized by choosing an adequate mobile-phase velocity ( $u > 2D_m/d_p$ ) [4].

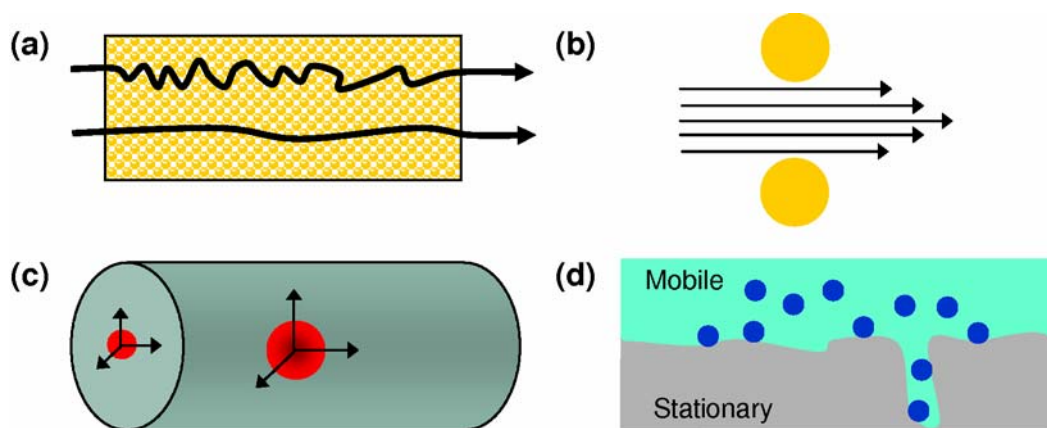


Figure 2-4: Four mechanisms of band broadening [4].

Finally, the fourth mechanism is the mass transfer process between the mobile, the “stagnant mobile,” and the stationary phases (Figure 2-4 (d)). A sample molecule entering a pore of stationary-phase particles (the stagnant mobile phase) pretty much ceases to be transported by the mobile-phase flux and changes its position mainly by diffusion, which is relatively slow. Therefore, some molecules could be stuck in the pores while others continue to move down the column with mobile phase. To reduce the band-broadening by this effect, mobile-phase flow velocity and viscosity should be reduced.

In order to design an optimized mobile-phase linear flow velocity that minimizes band-broadening and maximizes separation efficiency, the van Deemter equation, which

is the simplest among all the equations describing the dependence of HETP on linear flow velocity, can be used:

$$H = A + \frac{B}{u} + Cu \quad (2.23)$$

where the velocity-independent term  $A$  is a function of the inter-particle flow channel size distribution and other non-uniformities in the packed bed (i.e., a function of eddy diffusion and flow velocity distribution effects).  $A$  is proportional to particle size. The second term is inversely proportional to the linear velocity, which describes the sample molecule diffusion in the longitudinal direction. The third term is directly proportional to the linear velocity, which contains all terms related to analyte mass transfer. According to the van Deemter equation, the van Deemter curve can be plotted. As shown in Figure 2-5, curves 1, 2, and 3 describes the effect of the first, second and third term of the van Deemter equation on HETP, respectively. Curve 4 is the complete van Deemter curve, which sums up the other three curves. The optimal  $u$  is chosen to be where the corresponding  $H$  reaches its minimum. For narrow-bored HPLC columns, a rule of thumb optimal  $u$  is around 1 mm/sec.

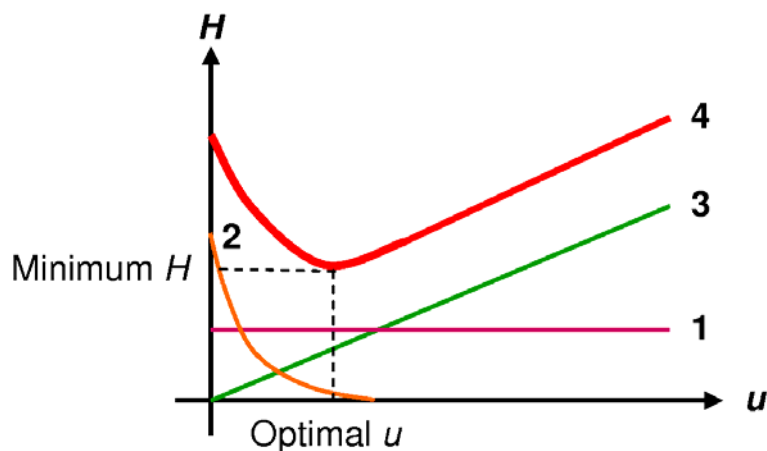


Figure 2-5: Van Deemter Curve [4].

## 2.2 HPLC Instrumentation

All HPLC systems have the following key components: solvent reservoirs, high-pressure solvent pumps, sample injection valve, separation column, analyte detector, and a computer system for chromatogram recording (Figure 2-6). A brief introduction to some of the important components will be given in the following sections.

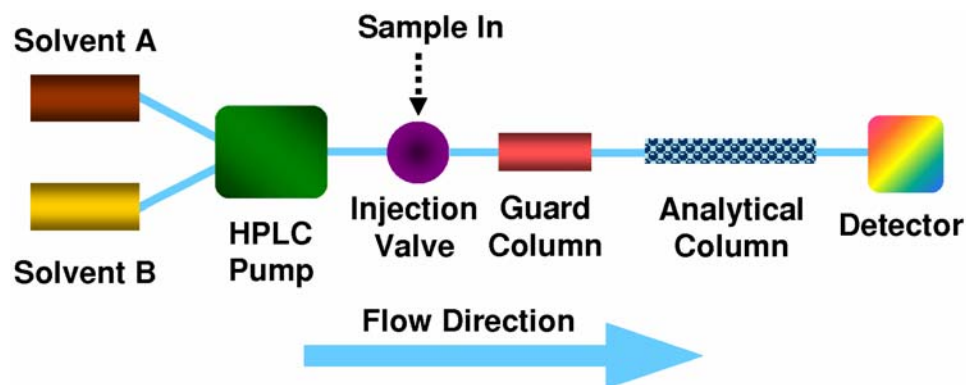


Figure 2-6: Schematic plot for a typical HPLC system.

### 2.2.1 Separation Column

#### 2.2.1.1 Separation Column Tube

Most commercial HPLC column tubes are made of 316-grade stainless steel, which is austenitic chromium-nickel-molybdenum steel, USA standard AISI, resistant to the usual HPLC pressure and also relatively inert to chemical corrosion. The inside of the column should have no rough surfaces, grooves, or microporous structures so the steel tubes must be either precisely drilled or polished after common manufacturing. Silica-fused capillary columns and PEEK columns are getting popular on the markets. Both materials have strong pressure resistance and chemical inertness.

Column dimensions, including column inner diameter (ID) and length, are very important parameters in an HPLC system. Columns with ID 2-5 mm are generally used

for analytical purposes. Wider columns with ID between 10 mm and 1 in are used for preparative work. Capillary HPLC columns made with fused silica have an ID no greater than 1 mm. Narrow-bore columns offer two main advantages compared to wider ones: less solvent consumption and higher signal height-to-sample mass ratio. The peak maximum concentration is inversely proportional to the square of the column ID. In terms of column length, a longer column surely provides a larger plate count and therefore better separation capability. However, backpressure and analysis time will also rise in proportion to the column length. In general, commercial columns of 5 to 30 cm long are common for stationary-phase particle size of 10  $\mu\text{m}$  or smaller.

#### **2.2.1.2 Separation Column Packing Material**

HPLC columns are in general densely packed with micron-sized particles ( $< 10 \mu\text{m}$ ) on which surfaces are chemically modified to have specific interaction with analyte molecules for retention purposes. Porous particles are often desirable since the porous structures significantly increase the overall stationary-phase surface area. Typical particle parameters for HPLC application include particle shape, size, pore size, and porosity. Particle shape is either spherical or irregular. The majority of all columns use spherical beads, since they provide more uniform and dense packing, better flow profiles, less backpressure, and higher separation efficiency. The diameter of most commercial HPLC particles is between 3  $\mu\text{m}$  and 10  $\mu\text{m}$ . As mentioned earlier, smaller particle sizes helps reduce band-broadening and result in higher separation efficiency. However, using smaller particles comes with the expense of significantly higher backpressure, which is inversely proportional to the square of particle diameter.

Particle pore size is the average dimension of the flow channels inside the porous particle. The pore size can range from 60 Å to over 10,000 Å. Molecules smaller than the pore size can enter the pores and fully utilize the internal stationary-phase surface. The particle surface area is determined by the pore size and abundance of pores in it. Higher porosity particles with smaller pores have larger surface area. For example, the surface area of a column packed with 5 µm non-porous particles is only 0.02 m<sup>2</sup>/mL, while that of a totally porous-particle-packed bed is 150 m<sup>2</sup>/mL [3]. Pores that are too small, however, are detrimental to column efficiency, since the internal surface will be difficult to access. For general purpose columns, 10 nm pores are often used. For large molecules like proteins, 100 nm pores are the best choice.

In general, the base material of the particles is a metal-oxide, such as silica and alumina, or a polymeric material, such as polystyrene-divinylbenzene (PS-DVB). Silica is the most popular base material for HPLC column packing, while polymeric materials are gaining popularity. A silica particle has silanol (-OH) groups on its surface, which can be chemically modified into desired functional groups. Figure 2-7 gives one example, where the silanol group is reacted with an alcohol, ROH. R may be an alkyl chain (C18, C8, C4) or other functional group. Depending on the functional groups added to the particle surfaces, particles can be used for different separation mechanisms in HPLC such as normal-phase, reversed-phase, ion-exchange, size-exclusion, hydrophilic-interaction, and hydrophobic-interaction liquid chromatography.

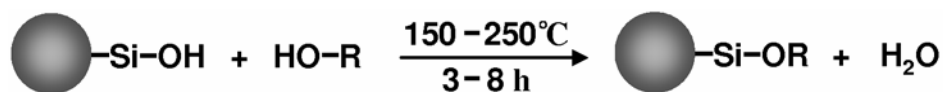


Figure 2-7: Chemical modification of silica surface.

Another type of stationary phase that has gained lots of attention in recent years is monolithic stationary phase [7, 8]. The idea is to synthesize stationary phases that consist of one single piece of porous material such as organic polymer or silica directly inside the separation column. With this concept, the chromatographic bed is not a packing of particles but a porous rod that totally fills the cylindrical volume of the column. Such materials have a porosity of more than 0.8 and their separation performance is similar to the packed bed.

### **2.2.2 Solvent Pumps**

The high-pressure solvent pump is a critical component of the HPLC system. It forces the mobile phase through the sample injector, separation column, detector, and from there on out. A versatile pump should be able to deliver flow rates from 0.1  $\mu\text{L}/\text{min}$  to 10  $\text{mL}/\text{min}$  with a precision of about 1% up to a maximum pressure of around 5000 psi. Two types of pumps can be distinguished: constant flow rate and constant pressure. For constant pressure pumps, flow rate can be affected by the column temperature fluctuation since mobile-phase viscosity changes about 2% per degree centigrade. Constant flow rate pumps are most desirable for reproducible retention times, but these pumps often produce noise in the detector because of the cyclic nature of their pumping action. Any blockage in the LC system will cause a constant flow rate pump to produce increasingly high backpressure, necessitating protection with a pressure relief valve. Most HPLC pumping systems can accommodate three or four solvents. A proportional metering valve can be used to produce accurate mixtures of two, three, or all four solvents. This solvent-mixing capability is necessary for solvent gradient elution.

Commercial HPLC pumps are mostly based on the reciprocating piston design [9]. Recently, a new pump for nano HPLC applications has appeared on the market, which uses compressed air as the pressure source and a flow sensor to perform feedback control to generate precise nanoliter-per-minute flow rates [10].

### 2.2.3 Sample Injection Valves

High-pressure valves are most often used for sample injection in HPLC. A typical valve (Figure 2-8) has six ports and two positions, one for sample loading and one for sample injection to the column. Interchangeable sample loops with calibrated volumes are attached to the valve and are filled with sample solution using a syringe. Sample loop volumes range from 0.25  $\mu\text{L}$  to hundreds of microliters. For smaller sample injection volumes, special valves have been designed with internal sample loop volumes as small as 4 nL and low swept volume connections (Valco Instruments, Houston, TX).

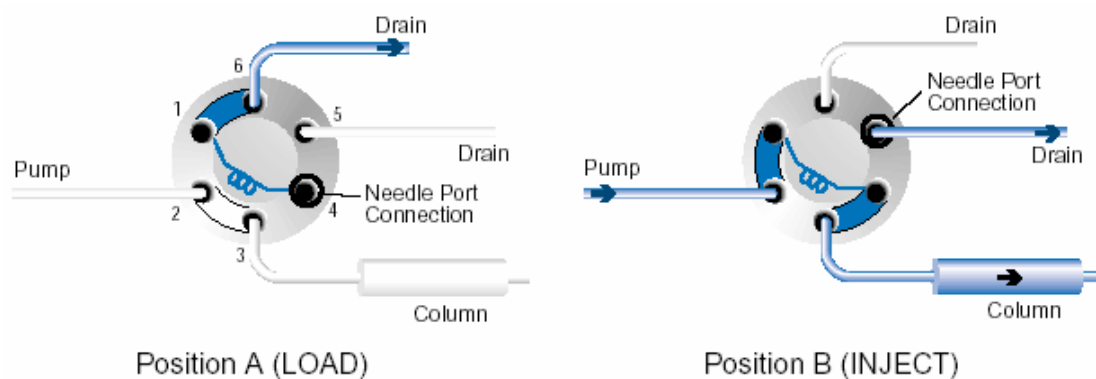


Figure 2-8: A six-port, two-position manual sample injection valve.

### 2.2.4 Analyte Detectors

Besides the separation column, the analyte detector is considered the most important component of an HPLC system. The detector translates the changes in the

chemical composition of the column effluent during the chromatographic run into electrical signals. The signals can then be recorded as chromatograms and processed to give the required information about the sample composition.

The choice of the detector depends on several sample-related factors: the chemical properties of the analytes, the range of analyte concentration, the complexity of the sample matrix, and also the other chromatographic system components performances used for the separation. Table 2-1 summarizes the sensitivity for the most common HPLC detectors [11-13]. Among HPLC detectors, UV-visible absorbance, fluorescence, refractive-index, and mass spectrometry detectors are used in all modes of LC; electrochemical or amperometric detectors are used in reversed-phase LC; conductivity detectors are used mainly in ion-exchange LC. Brief introductions to those sensors are given as follows.

Table 2-1: Typical sensitivity data for common HPLC detectors.

HPLC Detectors	Typical Concentration Sensitivity	Typical Mass Limit of Detection
Refractive Index	10 ppm	1 ng
UV/Visible	1 ppb	10 pg
Conductivity (non-suppressed and suppressed)	10 to 0.1 ppb	1 to 0.1 ng
MS	N/A	< 1 pg
Fluorescence	10 ppt	10 fg

UV-visible absorbance detectors measure the loss of ultraviolet or visible light as the light passes through the HPLC column effluent. The chemicals of interest must contain chromophores that absorb UV or visible light, such as conjugated double bonds

and aromatic rings. The flow cell is usually arranged in a “Z” pattern, in which the flow path is maximized to maximize absorbance that is proportional to the flow path in the detector cell. The absorbance detection method can be used for a large range of analyte species and is quite reliable. However, it is less sensitive than fluorescence, electrochemical, and mass spectrometry detections.

Fluorescence detection captures the fluorescence emission from analytes that are excited by light sources such as lasers with a shorter wavelength. The analytes must have fluorophores, which are compounds that fluoresce after being excited. Fluorescence detection has much better sensitivity than most other methods. One important disadvantage of fluorescence detection is that only a limited number of analyte species have native fluorescence. For analytes that do not fluoresce, a derivatization process needs to be done to put the fluorophore functional groups on the analyte before the separation.

Electrochemical or amperometric detectors sense analytes that are electroactive by having electron transfer between electrodes and molecules. They have pretty good sensitivity and are relatively cheap and simple to make. The drawback of electrochemical detection is that for analytes that are not electroactive, a derivatization process to the analyte is necessary before separation.

Conductivity detectors measure the electrical conductance of the HPLC column effluent. They are especially used for ion-exchange chromatography where the analytes are ionic and have weak UV absorbance. Non-suppressed conductivity detection measures sample signals directly on top of baseline signal contributed from the ionic mobile phase. Suppressed detection removes the ionic background in the effluent after

separation but prior to detection. The sensitivity of suppressed conductivity detection is one to two orders of magnitude better than non-suppressed as illustrated in Table 2-1. One main issue of conductivity detection is the temperature effect on the ion mobility, and thus on the effluent conductivity. Conductivity of an ionic solution rises about 2% for every degree Celsius increase in temperature [14]. Therefore, the detector cell temperature must be precisely maintained to reduce conductivity signal fluctuation.

Mass spectrometry is one of the most sensitive and selective detection methods for HPLC. It is universal and can be used for specific compound identification and quantitative determination. In a mass spectrometer, compounds are vaporized, ionized, separated, and detected according to their mass-to-charge ratio ( $m/z$ ). Electrospray ionization (ESI) [15] is one of the most common ionization techniques used to couple LC to MS analysis especially for high molecular weight samples used in proteomics. Other important interfacing techniques are atmospheric pressure chemical ionization (APCI) and matrix-assisted laser desorption ionization (MALDI) [16, 17]. Disadvantages of MS detection are that the MS system is bulky and expensive, which makes it less available than other detection methods. Also, since MS demands a rather low mobile-phase flow rate on the order of 100 to 1,000 nL/min, it raises challenges on the LC side such as pumping control and swept/dead volume reduction.

## **2.3 Logical Trend of HPLC Instrumentation**

### **2.3.1 Predictions from the Theory**

The logical trend of modern HPLC instrumentation is to miniaturize system components for its benefits in many aspects. For example, the reduction of separation

column inner diameter increases separation sensitivity [4], which is especially critical for modern proteomics where in many cases only a meager amount of sample molecules (hundreds to thousands copies of molecules) is available for analysis; smaller column inner diameter also reduces solvent consumption; smaller stationary-phase particles result in higher separation efficiency [4]; smaller size solvent pumps, valves, and tubes reduce flow path swept and dead volumes, which in turn shortens analysis time and reduces band-broadening effects. An overall miniaturized HPLC system will be portable and therefore many crucial applications such as point-of-use HPLC analysis or hand-held systems for personal health diagnostics are possible.

Except miniaturization, there are assorted targets of improvements for modern HPLC systems. For example: integration of various chromatographic columns with different separation mechanisms to achieve multi-dimensional separation tasks [18] or the high throughput parallel-separation tasks [19]; a reliable low flow rate solvent pump (< 100 nL/min) with smooth flow rate gradient capability for nano HPLC application [20]; an improved sample injection method that reliably delivers a tiny volume (<10 nL) of samples into the LC column without significant sample dispersion [21]; a monolithic stationary-phase packing material with controllable porosity and surface chemical property; an extremely sensitive analyte detector that has a single molecule detection limit [22].

### **2.3.2 Benefits of Microchip HPLC System**

It is conceivable that the need for HPLC miniaturization will lead to realization of constructing of a complete HPLC system on a single chip. Indeed, many unique

advantages are available for the lab-on-a-chip HPLC system compared to the desktop HPLC system as was discussed in earlier sections. Most of all, the unnecessary system fluidic swept/dead volume can be greatly reduced. In desktop HPLC systems, components such as pumps, valves, and columns are connected using macro-sized fittings and tubes. Those fluidic connectors contribute to a sizable swept volume that not only increases the overall analysis time but also degrades the chromatography performance. By integrating all the HPLC components on a single chip, swept/dead volume from connectors can be virtually eliminated.

Another advantage of the lab-on-a-chip HPLC system is the potentially much lower cost. A typical desktop HPLC system can cost around 30 to 40 thousand U.S. dollars. By using MEMS technology, microchip HPLC systems can be mass-produced with silicon or glass wafers, which not only significantly reduce the fabrication cost but also enhances fabrication throughput. It is also a promising thought that by making HPLC a portable and much cheaper (therefore disposable) system, many more applications related to daily life such as health or environmental monitoring will appear and the demand for HPLC will grow exponentially.

## **2.4 Review of Microchip HPLC Systems**

Although many advantages are available in chip-based HPLC systems, one would find it surprising that not much research has been done on this topic [23-29]. Reasons for that are manifold. First, fabrication of on-chip high pressure LC columns turns out to be very challenging [28]. Although various microfluidic channel technologies have been developed in MEMS, very few of them are suitable for HPLC purposes. In chapter 3 of

this thesis, brand new microfluidic channel technologies that are specifically designed for HPLC applications will be discussed. Second, while the solvent pump is a key component for high quality HPLC performance, it is extremely difficult to build reliable on-chip pumps for HPLC applications [29]. Third, on-chip sample injection for HPLC, unlike that for chip-based capillary electrophoresis, is a complicated procedure. In order to maintain the sample plug definition inside the high pressure microfluidic environment, mechanical valving at liquid I/O ports is necessary, which is by all means a challenging task [28]. Fourth, most microfluidic research in MEMS focuses on single component development such as channels, filters, mixers, pumps, or valves, however, for a successful lab-on-a-chip HPLC system, all components must be integrated using a reliable process and fabricated on a single chip. Processes that contain more than ten lithography masks or 50 fabrication steps are often necessary, which are surely not easy tasks. Finally, while packing chip-based LC column with stationary-phase particles seems to be a straightforward procedure, until recently most chip-based LC columns with few exceptions [30] were all made using alternative methods to prepare stationary phase such as open-tubular [26], surface-activated micromachined posts [25], continuous monolithic bed formed by in-situ polymerization [23], and column coated with nanoparticles [27]. In this thesis, all HPLC columns were packed with commercial stationary-phase particles using the conventional slurry-packing technique.

Progresses in making microchip HPLC systems will be discussed as follows. In 2004, Nanostream Inc. (Pasadena, CA) revealed a micro parallel LC cartridge, which was made of polymeric material and had 24 particle-packed microfluidic columns allowing 24 samples to be analyzed in parallel. The samples are injected from off-chip using auto

sampler and detected with 24 UV absorbance detectors off-chip [19]. Also lately, researchers from Agilent Technologies (Palo Alto, CA) presented their chip-based fritless LC column with an electrospray ionization (ESI) nozzle [31, 32]. The chip is made of two polyimide layers bonded together, while the ESI nozzle is fabricated by laser ablative trimming of the bonded chip. The column is packed with C18 beads using a tapered outlet rather than a frit, utilizing a so-called keystone effect [33]. Samples are injected off-chip using an injection valve attached to the back of the chip. A mass spectrometer (MS) is used as the detector.

In 2004, Qing and colleagues from our group reported an integrated ion liquid chromatography system with an on-chip particle-packed separation column, particle filters, sample injection loop, and conductivity detector [28]. The microchip was fabricated using silicon wafers and CMOS-compatible processes. Column pressure capacity was tested up to 800 psi. Using that system, a sample containing a mixture of seven anions was successfully separated. In 2005, a fully integrated gradient elution LC-ESI microchip system was reported by Xie and colleagues from our group [34]. The chip integrated a pair of high-pressure gradient pumps, a sample injection pump, a passive solvent mixer, a particle-packed separation column, and an ESI nozzle. Using that system, successful separation of protein digests by reversed-phase LC (RP-LC) coupled with on-line MS analysis was demonstrated.

## **2.5 Comparisons between LC and CE**

Compared with liquid chromatography (LC), capillary electrophoresis (CE) is a relatively new separation technology. Since its first description in the late 1960s, various

capillary electrophoresis techniques have been demonstrated, including capillary zone electrophoresis (CZE), displacement electrophoresis (isotachopheresis), isoelectric focusing, molecular sieving separations, and others.

Electrophoresis is a separation method in which the separation driving force is the electric field. Electrically charged species dissolved or suspended in an electrolyte and subjected to an electric field are caused to move toward the electrode that carries opposite charges. Separation occurs when cations move in one direction and anions in the other, or when the rates of migration (electrophoretic mobility) of similarly charged ions are different. Electroosmotic flow (EOF), a phenomenon occurs when a high-density-charged surface is put under an electric field, such as that of an uncoated silica-fused capillary tube, is an additional force with which analytes can be transported down the capillary in the presence of an electric field. Separations performed in the presence of EOF exhibit plug-flow characteristics, resulting in a low band-broadening effects and high separation efficiency. This contrasts with the laminar flow properties of LC where the flow distribution results in band-broadening and low separation efficiency.

Table 2-2: Comparisons between LC and CE [35-37].

<b>LC (Liquid Chromatography)</b>	<b>CE (Capillary Electrophoresis)</b>
Pros: <ul style="list-style-type: none"> <li>▪ Much better sensitivity</li> <li>▪ Better reproducibility</li> <li>▪ Versatile stationary phase</li> <li>▪ Well-established methods</li> </ul> Cons: <ul style="list-style-type: none"> <li>▪ Longer analysis time</li> <li>▪ Higher cost</li> </ul>	Pros: <ul style="list-style-type: none"> <li>▪ Simpler and cheaper system</li> <li>▪ Higher separation efficiency</li> <li>▪ Much faster analysis</li> <li>▪ Lower solvent consumption</li> </ul> Cons: <ul style="list-style-type: none"> <li>▪ Lower reproducibility</li> <li>▪ Lower sensitivity</li> </ul>

Because of its many unique advantages (Table 2-2), CE shows great promise as an analytical tool and in some cases it may replace HPLC. However, due to the complementary analyte selectivity of LC and CE [35], it is not likely that CE can totally replace LC. One can expect both separation techniques to exist and continue to improve in the near future.

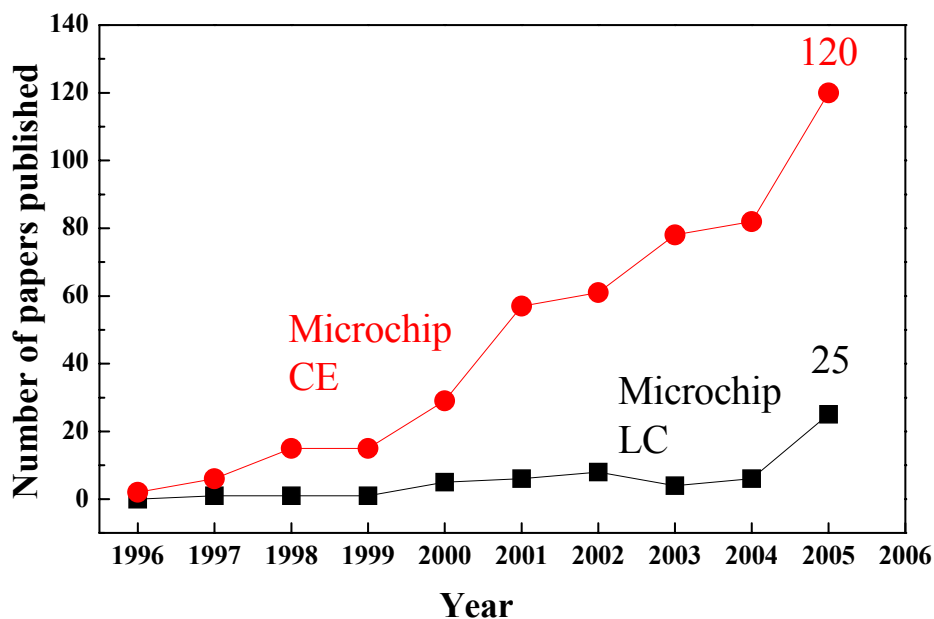


Figure 2-9: Microchip research activities in LC and CE. Only papers cited by Science Citation Index (SCI) were counted in this survey.

Finally, in terms of microchip research, microchip CE has been much more popular than microchip LC in the past decade as shown in Figure 2-9. The main reason for that is the much easier fabrication process for microchip CE systems since sample injection and elution are both driven by electric fields instead of on-chip pumps and no particle packing or high pressure column is necessary [38]. On the other hand, it is clear that microchip LC research has just begun to blossom in recent years. Our group has

been heavily involved in its development aiming to deliver mature fabrication technologies and to speed up its commercialization process.

## **2.6 Conclusions**

The continuous efforts on improving HPLC instrumentation and performances have led to the conclusion of system miniaturization. It makes perfect sense to realize this miniaturization task with the well-developed MEMS technology and fabricate the fully functioned lab-on-a-chip HPLC systems. While the research of microchip HPLC system is still in its early stage and many issues regarding fabrication and separation performance need to be resolved, one can surely see the fast advancement of this field and potential applications that can be accordingly provided. This thesis is therefore aimed to push further the maturity of microchip HPLC development and demonstrate the full potential of this approach.

## 2.6 Bibliography

- [1] L. S. Ettre, "M.S. Twsett and the invention of chromatography," *LC GC North America*, vol. 21, pp. 458, 2003.
- [2] A. J. P. Martin and R. L. M. Synge, "A new form of chromatogram employing two liquid phases," *Biochemical Journal*, vol. 35, pp. 1358-1368, 1941.
- [3] U. D. Neue, *HPLC Columns: Theory, Technology, and Practice*: Wiley-VCH, 1997.
- [4] V. R. Meyer, in *Practical high-performance liquid chromatography*, 3rd ed. New York: Wiley: Chichester, 1998.
- [5] T. Greibrokk and T. Andersen, "Temperature programming in liquid chromatography," *Journal of Separation Science*, vol. 24, pp. 899-909, 2001.
- [6] J. M. Miller, *Chromatography concepts and contrasts*, 2nd ed. New Jersey: Wiley-Interscience, 2005.
- [7] A. M. Siouffi, "Silica gel-based monoliths prepared by the sol-gel method: facts and figures," *Journal of Chromatography A*, vol. 1000, pp. 801-818, 2003.
- [8] S. Miller, "Separations in a monolith," *Analytical Chemistry*, vol. 76, pp. 99A-101A, 2004.
- [9] E. Katz, R. Eksteen, P. Schoenmakers, and N. Miller, *Handbook of HPLC*, vol. 78. New York: Marcel Dekker, 1998.
- [10] <http://www.eksigent.com>
- [11] B. Limpert, L. Consulting, and Bellingham, "Alltech HPLC Detector Seminar Booklet," 1995.

- [12] D. A. Skoog, *Fundamentals of analytical chemistry*, 8th ed. Belmont, CA: Thomson-Brooks/Cole, 2004.
- [13] D. Parriott, *A Practical guide to HPLC detection*. San Diego: Academic Press, 1993.
- [14] J. S. Fritz and D. T. Gjerde, *Ion chromatography*, 3rd, completely rev. and enl. ed. Weinheim [Germany]; New York: Wiley-VCH, 2000.
- [15] C. M. Whitehouse, R. N. Dreyer, M. Yamashita, and J. B. Fenn, "Electrospray Interface for Liquid Chromatographs and Mass Spectrometers," *Analytical Chemistry*, vol. 57, pp. 675-679, 1985.
- [16] A. C. Hogenboom, W. M. A. Niessen, and U. A. T. Brinkman, "Rapid target analysis of microcontaminants in water by on-line single-short-column liquid chromatography combined with atmospheric pressure chemical ionization ion-trap mass spectrometry," *Journal of Chromatography A*, vol. 794, pp. 201-210, 1998.
- [17] W. M. A. Niessen, "Advances in instrumentation in liquid chromatography mass spectrometry and related liquid-introduction techniques," *Journal of Chromatography A*, vol. 794, pp. 407-435, 1998.
- [18] A. Werner, W. Siems, U. Kuckelkorn, T. Grune, and C. Schreiter, "Anion-exchange and size-exclusion chromatography of proteins in mouse ascites-fluid-changes in the protein pattern during tumor-growth in vivo," *Chromatographia*, vol. 29, pp. 351-354, 1990.
- [19] Nanostream, "Brio catridges," 2006.

- [20] K. Sandra, I. Stals, P. Sandra, M. Claeysens, J. Van Beeumen, and B. Devreese, "Combining gel and capillary electrophoresis, nano-LC and mass spectrometry for the elucidation of post-translational modifications of *Trichoderma reesei* cellobiohydrolase I," *Journal of Chromatography A*, vol. 1058, pp. 263-272, 2004.
- [21] J. M. Ramsey, "Nanofabricated fluidic structures for elucidation of molecular information," presented at the 20th International Symposium on Microscale Bioseparations, Amsterdam, the Netherlands, 2006.
- [22] M. Tokeshi, M. Uchida, K. Uchiyama, T. Sawada, and T. Kitamori, "Single- and countable-molecule detection of non-fluorescent molecules in liquid phase," *Journal of Luminescence*, vol. 83-4, pp. 261-264, 1999.
- [23] C. Ericson, J. Holm, T. Ericson, and S. Hjerten, "Electroosmosis- and pressure-driven chromatography in chips using continuous beds," *Analytical Chemistry*, vol. 72, pp. 81-87, 2000.
- [24] C. M. Harris, "Shrinking the LC landscape," *Analytical Chemistry*, vol. 75, pp. 64A-69A, 2003.
- [25] B. He, N. Tait, and F. Regnier, "Fabrication of nanocolumns for liquid chromatography," *Analytical Chemistry*, vol. 70, pp. 3790-3797, 1998.
- [26] A. Manz, Y. Miyahara, J. Miura, Y. Watanabe, H. Miyagi, and K. Sato, "Design of an Open-Tubular Column Liquid Chromatograph Using Silicon Chip Technology," *Sensors and Actuators B-Chemical*, vol. 1, pp. 249-255, 1990.
- [27] J. P. Murrihy, M. C. Breadmore, A. M. Tan, M. McEnery, J. Alderman, C. O'Mathuna, A. P. O'Neill, P. O'Brien, N. Advoldvic, P. R. Haddad, and J. D.

- Glennon, "Ion chromatography on-chip," *Journal of Chromatography A*, vol. 924, pp. 233-238, 2001.
- [28] Q. He, C. Pang, Y. C. Tai, and T. D. Lee, "Ion liquid chromatography on-a-chip with beads-packed parylene column," presented at the 17th IEEE International Conference on Micro Electro Mechanical Systems (MEMS 2004), Maastricht, The Netherlands, 2004.
- [29] J. Xie, J. Shih, Q. He, C. Pang, Y. C. Tai, Y. N. Miao, and T. D. Lee, "An integrated LC-ESI chip with electrochemical-based gradient generation," presented at the 17th IEEE International Conference on Micro Electro Mechanical Systems (MEMS 2004), Maastricht, The Netherlands, 2004.
- [30] G. Ocvirik, E. Verpoorte, A. Manz, M. Grasserbauer, and H. M. Widmer, "High-Performance Liquid-Chromatography Partially Integrated onto a Silicon Chip," *Analytical Methods and Instrumentation*, vol. 2, pp. 74-82, 1995.
- [31] K. Killeen, H. Yin, D. Sobek, R. Brennen, and T. v. d. Goor, "Chip-LC/MS: HPLC-MS using polymer microfluidics," presented at Seventh International Conference on Micro Total Analysis Systems (microTAS 2003), Squaw Valley, California, USA, 2003.
- [32] G. Rozing, "Trends in HPLC column formats-Microbore, nanobore and smaller," *Lc Gc Europe*, vol. 16, pp. 14-19, 2003.
- [33] G. A. Lord, D. B. Gordon, P. Myers, and B. W. King, "Tapers and restrictors for capillary electrochromatography and capillary electrochromatography mass spectrometry," *Journal of Chromatography A*, vol. 768, pp. 9-16, 1997.

- [34] J. Xie, Y. N. Miao, J. Shih, Y. C. Tai, and T. D. Lee, "Microfluidic platform for liquid chromatography-tandem mass spectrometry analyses of complex peptide mixtures," *Analytical Chemistry*, vol. 77, pp. 6947-6953, 2005.
- [35] M. Serwe and G. A. Ross, "A comparison of CE-MS and LC-MS for peptide samples," *Lc Gc North America*, vol. 18, p. 46, 2000.
- [36] M. S. A. Prado, M. Steppe, M. F. M. Tavares, E. R. M. Kedor-Hackmann, and M. I. R. M. Santoro, "Comparison of capillary electrophoresis and reversed-phase liquid chromatography methodologies for determination of diazepam in pharmaceutical tablets," *Journal of Pharmaceutical and Biomedical Analysis*, vol. 37, pp. 273-279, 2005.
- [37] M. C. Carneiro, L. Puignou, and M. T. Galceran, "Comparison of Capillary Electrophoresis and Reversed-Phase Ion-Pair High-Performance Liquid-Chromatography for the Determination of Paraquat, Diquat and Difenzoquat," *Journal of Chromatography A*, vol. 669, pp. 217-224, 1994.
- [38] D. J. Harrison, A. Manz, Z. H. Fan, H. Ludi, and H. M. Widmer, "Capillary Electrophoresis and Sample Injection Systems Integrated on a Planar Glass Chip," *Analytical Chemistry*, vol. 64, pp. 1926-1932, 1992.

---

# CHAPTER 3

---

## HIGH-PRESSURE MICROFLUIDIC CHANNEL TECHNOLOGY

### 3.1 Introduction

The separation column is the key component of any HPLC system. When constructing an HPLC separation column, the top criterion is to have a robust column structure in order to survive the hundreds to thousands of psi inner pressure loading encountered during the stationary-phase particle-packing or the formal chromatography procedures. Conventional silica-fused capillary columns or stainless steel columns are readily made to withstand thousands to tens of thousands psi pressure loading [1]. However, until recently it has been very challenging to build a chip-based high-pressure-rating HPLC column or microfluidic channel that can withstand pressure higher than 1,000 psi [2].

Various materials and technologies have been investigated for building microfluidic channels for applications such as chip-based flow cytometry [3], electrophoresis [4], polymerase chain reaction (PCR) [5], and gas chromatography [6] over the past decade. However, pressure requirements for most of those microfluidic applications are very low. Normally, a pressure capacity of 10 psi is quite enough for those devices. That is why there has so far been few research efforts made for building high-pressure-rating microfluidic channels. In the following sections, a review of the existing microfluidic channel technologies will first be given and then the novel high-pressure parylene microfluidic channel technology will be presented.

## **3.2 Review of Microfluidic Channel Technology**

### **3.2.1 PDMS Microfluidic Channel**

The PDMS (polydimethylsiloxane) microfluidic channel is made using a technique called “soft lithography” [7]. In soft lithography, a master mold is first made by lithographic and etching techniques. Then an elastomeric stamp, such as PDMS, is cast from this master mold. Channel configuration is transferred from the master mold to the PDMS stamp. After removing the PDMS stamp from the master mold, fluidic inlet/outlet to the channel is created by punching through-holes on the PDMS stamp using syringe needles [8]. Finally, the PDMS stamp is put on top of a substrate such as a glass slide to form microfluidic devices (Figure 3-1 (a)). The adhesion between PDMS and the glass substrate is enhanced by surface treatments to both PDMS and glass before bonding. A post-bonding curing process is often used to improve the bonding strength. More fabrication details regarding PDMS microfluidic devices can be found in chapter 6.

The PDMS channel is very easy to fabricate and its cost is pretty low. It also has advantages including optical transparency and bio-compatibility. However, a typical PDMS microfluidic channel has a pressure capacity of less than 30 psi [9]. Besides, the material softness and poor chemical-resistance of PDMS also make it unsuitable for HPLC applications.

### **3.2.2 Thermal-Bonding Microfluidic Channel**

A variety of thermal-bonding techniques to form microfluidic channels have been reported, including field-assisted thermal bonding (anodic bonding), silicon/silicon or silicon/glass or glass/glass fusion bonding (Figure 3-1 (b)), and thermal-bonding with intermediate layers [10]. In general, the thermal-bonding microfluidic channel has great pressure capacity (bonding strength up to 20 MPa or around 3,000 psi has been reported [11]). However, the thermal-bonding procedure requires high temperature ( $> 400\text{ }^{\circ}\text{C}$ ), which makes it not a post-IC compatible process. Also, the bonding procedure requires extremely smooth and flat wafer surfaces for void-free bonding process, which reduces the process flexibility and accordingly the device functionality. Finally, precise alignment (misalignment within  $1\text{ }\mu\text{m}$ ) between two wafers during the thermal-bonding procedure still remains a challenging task.

### **3.2.3 Nitride Microfluidic Channel**

Nitride ( $\text{Si}_3\text{N}_4$ ), silicon dioxide or polysilicon microfluidic channel technologies have been studied in the past (Figure 3-1 (c)) [12, 13]. For example, to fabricate nitride channels, a polysilicon sacrificial layer is first deposited and patterned on top of a silicon

or silicon dioxide surface. A nitride layer is then deposited using LPCVD at 850 °C. Polysilicon is then released using KOH or TMAH [13]. Nitride has excellent adhesion to silicon or oxide surfaces. However, the polysilicon release process produces a large amount of hydrogen gas, which generates high pressure inside the nitride channel and can damage the nitride thin film. The sacrificial layer deposited by LPCVD (polysilicon, nitride, or oxide) in general has a thickness less than 5 μm, which poses a limit to the available channel height. The nitride layer deposited by LPCVD also has high intrinsic stress (tensile), which makes it even more brittle and can easily fracture during processing. Finally, the high temperature LPCVD process makes this type of channel fabrication process not post-IC compatible.

#### **3.2.4 Parylene Microfluidic Channel**

The parylene microfluidic channel is made by first depositing a parylene layer using a room temperature CVD system (Specialty Coating Systems, Indianapolis, IN) on top of a silicon or glass substrate to form the channel bottom wall. A photoresist layer is then deposited and patterned on top of the parylene layer as a sacrificial layer for channel cross-section definition. Another parylene layer is then deposited on top of the photoresist and parylene layers to form the channel top wall. Photoresist is then released by solvents via channel openings (Figure 3-1 (d)) [14]. To enhance the pressure capacity of the microfluidic channel, the first parylene layer top surface can be treated with oxygen plasma followed by 5% HF dipping to roughen and clean the surface, which effectively enhances the bonding strength between parylene layers after the top parylene layer is deposited. Another way to make parylene microfluidic channel is by depositing

and patterning the photoresist layer directly on top of the silicon or silicon dioxide surface without having the bottom parylene layer. The top parylene layer is then deposited followed by photoresist releasing. In this case, channel pressure capacity is controlled by the adhesion strength of parylene to silicon or parylene to silicon dioxide. Although the parylene adhesion to silicon or silicon dioxide in general can be improved by using a chemical adhesion promoter such as A-174 (gamma-methacryloxypropyltrimethoxy silane, Specialty Coating Systems, Indianapolis, IN), this procedure cannot be used on this occasion since A-174 solution can dissolve the photoresist layer, which is used for channel cross-section definition.

The parylene microfluidic channel introduced above has great process flexibility and parylene has excellent chemical-inertness. However, due to the weak adhesion of parylene to most substrate surfaces, the pressure capacity of this type of parylene channel is around 30 psi, which is still way too low for HPLC applications.

### **3.2.5 Buried Microfluidic Channel**

Buried microfluidic channel or buried channel technology (BCT) has been developed and proposed for various biochemical applications [15]. The fabrication starts with etching a trench on the silicon wafer using RIE or DRIE. Sidewalls of the trenches are then coated with a protection layer such as thermal oxide or LPCVD nitride. Coating at the trench bottom is then removed using RIE. Bulk etching of the silicon substrate is then carried out through the trench bottom opening to create the channel cross-section. Finally, the trench is sealed by an LPCVD conformal coating such as polysilicon or nitride (Figure 3-1 (e)).

BCT provides extremely high pressure capacity (thousands of psi), which is perfect for HPLC application. However, burying the channel deep inside the silicon substrate will either make the integration of analyte sensors (whether they are optical or electrical sensors) to the channel difficult or the sensor sensitivities can be extremely low since the sensors are most likely distant from analyte solutions. Also, the proposed technology may encounter difficulty in making well-defined channel cross-section and stationary-phase particle filter because the bulk-etching process cannot be easily monitored in-situ. To resolve these issues, we have developed an embedded-type parylene microfluidic channel technology, which will be discussed in 3.3.2.

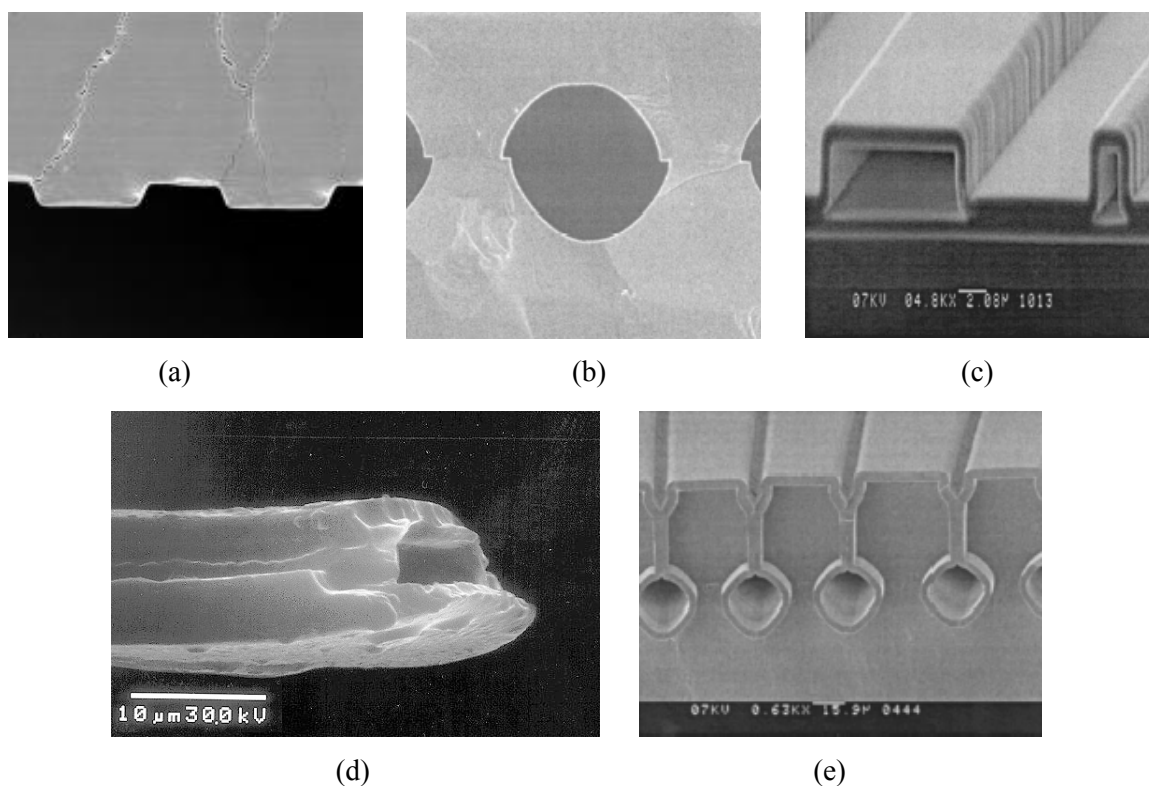


Figure 3-1: Pictures of assorted microfluidic channels. (a) PDMS stamp that shows channel topography, (b) silicon/silicon thermal-bonding channel, (c) nitride channel, (d) parylene channel/nozzle, (e) buried channel [15].

### **3.3 High-Pressure Parylene Microfluidic Channel Technology**

As has been discussed in chapter 1, parylene has been widely used as a structural material in making assorted microfluidic devices. In order to provide enough pressure capacity for parylene-based HPLC devices, we have developed novel parylene microfluidic channel technologies that can withstand pressure loading higher than 1,000 psi. The proposed high-pressure channel technologies can be categorized into anchored-type and embedded-type parylene microfluidic channels and will be discussed as follows.

#### **3.3.1 Anchored-Type Parylene Microfluidic Channel**

In order to enhance the pressure capacity of the parylene channel introduced in 3.2.4, the weak adhesion of the parylene layer to the silicon or parylene substrate must be avoided or improved. The design concept of the anchored-type parylene channel is to mechanically anchor the top parylene layer down to the silicon substrate. Bottom parylene layer is in general not necessary in this design. Two types of mechanical anchoring techniques have been developed previously in our lab as shown in Figure 3-2. Type I: After patterning the sacrificial photoresist, which defines the channel cross-section and before the top parylene deposition, the silicon substrate is roughened using  $\text{XeF}_2$  or  $\text{BrF}_3$ , which generates a silicon surface roughness of a few microns [16]. This surface roughness provides a larger equivalent parylene/silicon contact area and a mechanical locking mechanism, which effectively enhance the top parylene adhesion to the silicon substrate. Testing results have shown the pressure capacity (or burst pressure) of this roughening-anchored parylene channel is around 350 psi [2]. The common failure mode is that parylene layer will detach from the roughened silicon surface at high

pressure. Type II: After patterning the sacrificial photoresist and before the top parylene deposition, a self-aligned DRIE trench (with a mushroom anchoring space in the bottom [17]) lying right next to the sacrificial photoresist can be created. This trench structure provides a larger equivalent parylene/silicon contact area and a mechanical locking mechanism from the mushroom structure, which effectively enhance the top parylene adhesion to the silicon substrate (Figure 3-3). Testing results have shown the pressure capacity of this trench-anchored parylene channel is around 700 psi [2]. The failure modes for the trench-anchored channels can be either parylene peeling from the trenches or parylene-film-bursting at defected locations.

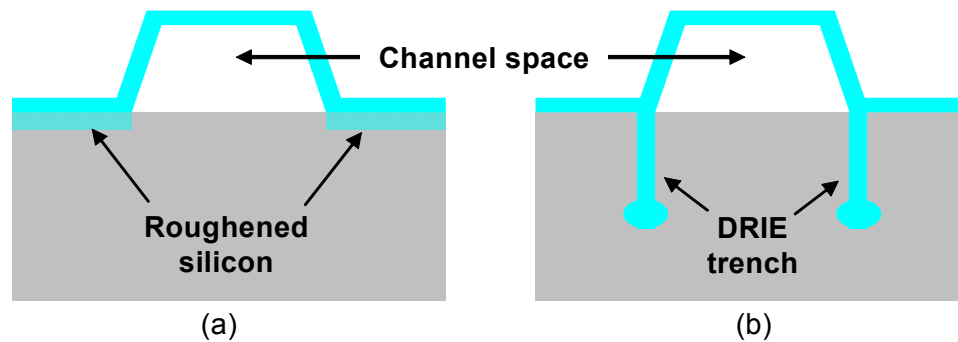


Figure 3-2: Anchored-type parylene channel. (a) Roughening-anchored channel, (b) trench-anchored channel.

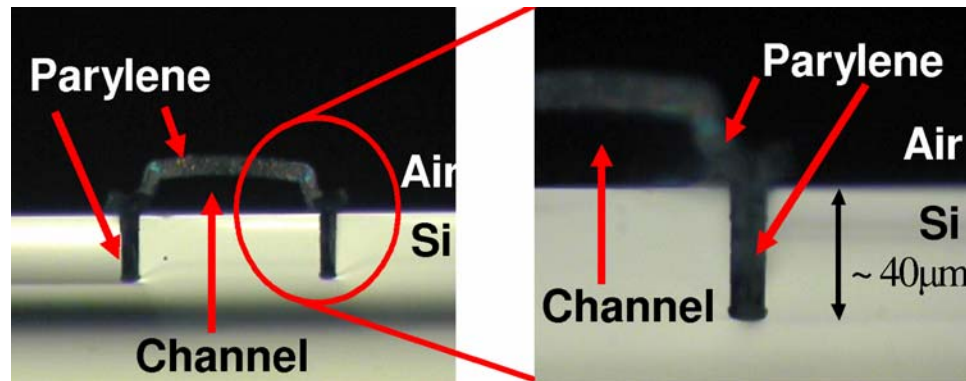


Figure 3-3: Cross-sectional pictures of a trench-anchored parylene channel [2].

### 3.3.2 Embedded-Type Parylene Microfluidic Channel

The design concept of the embedded-type parylene channel is to build the channel space inside the silicon substrate so to obtain high pressure-capacity of the channel. Different from the buried channel technology (BCT) mentioned in 3.2.5, the channel top surface is at the same height as the silicon wafer surface. This channel configuration allows easy integration of optical sensing such as laser-induced fluorescence detection or electrical sensing such as capacitively-coupled contactless conductivity detection ( $C^4D$ ) through the top surface of the channel.

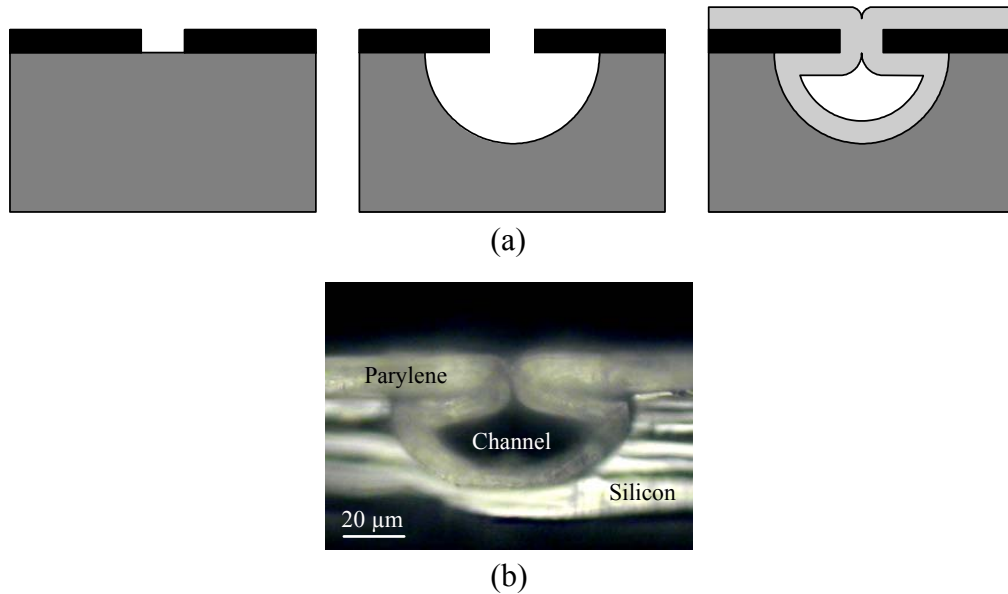


Figure 3-4: Basic embedded-type parylene channel. (a) Fabrication process flow for the basic embedded-type parylene channel, (b) fabricated basic embedded-type parylene channel.

The simplest way to fabricate an embedded-type parylene channel is shown in Figure 3-4 (a). Thermal oxide is first grown on the silicon substrate. The oxide layer is then patterned with buffered HF to create openings for  $XeF_2$  etching.  $XeF_2$  is used to

etch silicon through the oxide opening and create the channel cross-section. Finally, a parylene layer is deposited to seal the oxide opening. Figure 3-4 (b) shows the fabricated channel cross-section [18]. The fabrication process for the basic embedded-type parylene channel is extremely simple. However, the produced channel configuration does have unavoidable drawbacks. First, the channel cross-section is not highly symmetric compared with most commercial LC columns. This unsymmetry can contribute to band-broadening in the chromatographic process due to eddy diffusion or flow distribution. Second, it is more difficult to fabricate a well-defined stationary-phase particle filter using this technology (to be discussed more in chapter 5).

To overcome the issues encountered in the basic embedded-type parylene channel, a more sophisticated process has been developed as shown in Figure 3-5. The fabrication process starts with creating trenches on the silicon substrate using DRIE (Figure 3-5 (a)). The width between trenches defines the initial channel width. The first parylene layer is then deposited, which fills up the trenches. Oxygen plasma is then used to etch back the first parylene layer until the silicon surface reveals. The trenches, however, will still be filled with the first parylene coating. The second parylene layer (around 2  $\mu\text{m}$  in thickness) is then deposited. The second parylene is then patterned with oxygen plasma to create openings for the latter  $\text{XeF}_2$  etching process (Figure 3-5 (b)).  $\text{XeF}_2$  is used to etch away silicon through the parylene opening and create the square-like channel cross-section (Figure 3-5 (c)). The depth of the channel can be monitored during  $\text{XeF}_2$  etching for precise cross-section control. Finally, the third parylene layer is deposited to seal the parylene opening (Figure 3-5 (d)). Figure 3-6 then shows the fabricated channel cross-section [19].

The pressure capacity of the embedded-type parylene channel has been tested to be higher than 1,000 psi without fracture [18]. Moreover, due to the highly planarized chip surface, a direct-top-clamping to the chip with a glass plate can be easily applied to enhance channel pressure capacity to thousands of psi, which will be discussed more in chapter 5.

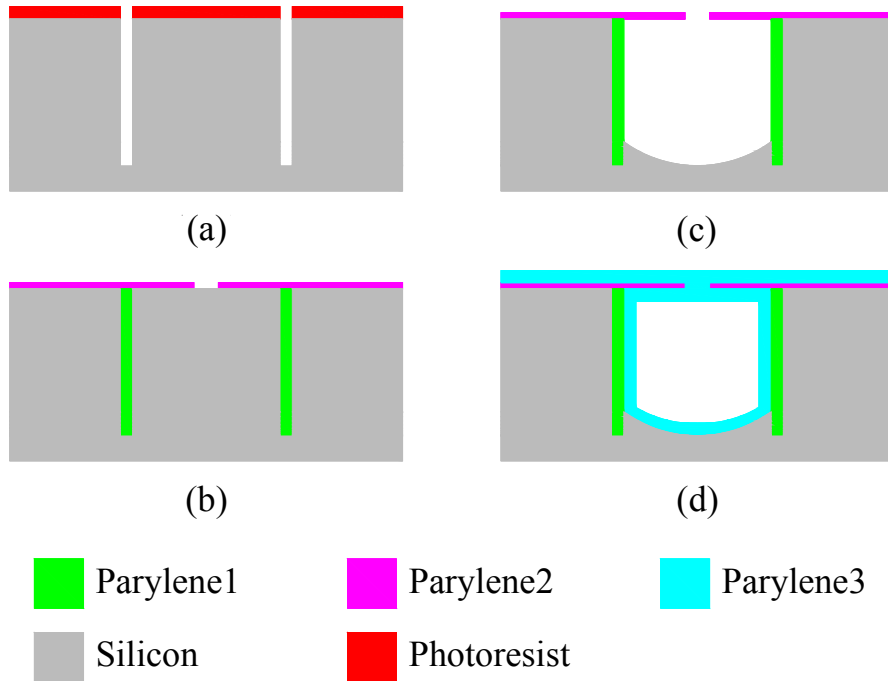


Figure 3-5: Fabrication process flow for the advanced embedded-type parylene channel.

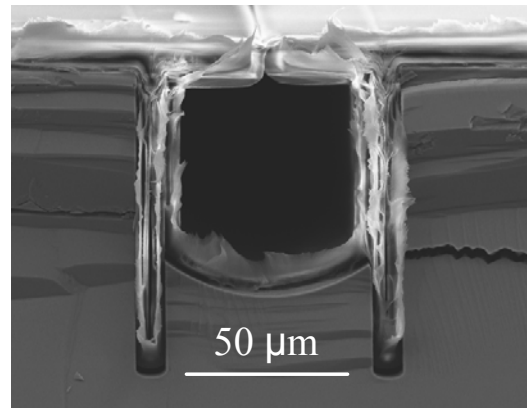


Figure 3-6: SEM of the advanced embedded-type parylene channel.

### 3.3.3 Comparisons

Both anchored-type and embedded-type parylene channels have their unique advantages and disadvantages, which make them suitable for different application needs. For example, the anchored-type channel allows the fabrication of in-channel electrodes that are exposed to the solvents. These electrodes can serve the purposes of electrochemical/conductivity sensing of analytes, electrolysis, or ionization of solvents [2, 20]. On the other hand, the in-channel electrodes of the anchored-type channel will always be covered by the third parylene coating and therefore the electrodes will not be in direct contact with the analytes or solvents. The embedded-type channel does have higher pressure capacity than the anchored-type channel, especially when the glass-plate-clamping technique is applied to the planarized chip surface. The embedded-type channel has a square-like cross-section while the anchored-type channel normally has a rectangular cross-section that can contribute to band-broadening and degrade the chromatography performance. Characteristics of each channel technology will be further discussed in chapters 4 and 5, respectively.

## 3.4 Conclusions

In this chapter, a review of existing microfluidic channel technologies was provided to evaluate their feasibility for microchip HPLC applications. It is clear that all the existing technologies have their own limitations and can compromise the functionality or chromatographic performances of the microchip HPLC systems. We therefore developed and illustrated in this chapter two types of novel high-pressure parylene microfluidic channel technologies, i.e., anchored-type and embedded-type

channels, which showed unique characteristics for microchip HPLC purposes. The developed parylene microfluidic channel technologies were used to build microchip HPLC systems that will be introduced in chapters 4 and 5.

### 3.5 Bibliography

- [1] U. D. Neue, *HPLC columns, theory, technology, and practice*. New York: Wiley-VCH, 1997.
- [2] Q. He, C. Pang, Y. C. Tai, and T. D. Lee, "Ion liquid chromatography on-a-chip with beads-packed parylene column," presented at the 17th IEEE International Conference on Micro Electro Mechanical Systems (MEMS 2004), Maastricht, The Netherlands, 2004.
- [3] D. P. Schrum, C. T. Culbertson, S. C. Jacobson, and J. M. Ramsey, "Microchip flow cytometry using electrokinetic focusing," *Analytical Chemistry*, vol. 71, pp. 4173-4177, 1999.
- [4] S. C. Jacobson, L. B. Koutny, R. Hergenroder, A. W. Moore, and J. M. Ramsey, "Microchip Capillary Electrophoresis with an Integrated Postcolumn Reactor," *Analytical Chemistry*, vol. 66, pp. 3472-3476, 1994.
- [5] B. C. Giordano, J. Ferrance, S. Swedberg, A. F. R. Huhmer, and J. P. Landers, "Polymerase chain reaction in polymeric microchips: DNA amplification in less than 240 seconds," *Analytical Biochemistry*, vol. 291, pp. 124-132, 2001.
- [6] H. S. Noh, P. J. Hesketh, and G. C. Frye-Mason, "Parylene gas chromatographic column for rapid thermal cycling," *Journal of Microelectromechanical Systems*, vol. 11, pp. 718-725, 2002.
- [7] O. J. A. Schueller, S. T. Brittain, and G. M. Whitesides, "Fabrication of glassy carbon microstructures by soft lithography," *Sensors and Actuators A-Physical*, vol. 72, pp. 125-139, 1999.

- [8] M. A. Unger, H. P. Chou, T. Thorsen, A. Scherer, and S. R. Quake, "Monolithic microfabricated valves and pumps by multilayer soft lithography," *Science*, vol. 288, pp. 113-116, 2000.
- [9] C. Y. Shih, S. Zheng, E. Meng, Y. C. Tai, Y. Liu, and J. F. Stoddart, "Nano-to-micro self-assembly using shear flow devices," presented at the 17th IEEE International Conference on Micro Electro Mechanical Systems (MEMS 2004), Maastricht, the Netherlands, 2004.
- [10] M. J. Madou, *Fundamentals of Microfabrication*, 2nd ed. New York: CRC Press, 2002.
- [11] G. Kissinger and W. Kissinger, "Void-Free Silicon-Wafer-Bond Strengthening in the 200-400 Degrees-C Range," *Sensors and Actuators A-Physical*, vol. 36, pp. 149-156, 1993.
- [12] R. T. Howe, "Surface Micromachining for Microsensors and Microactuators," *Journal of Vacuum Science & Technology B*, vol. 6, pp. 1809-1813, 1988.
- [13] A. Desai, "Micromachined devices for an airborne bio-particle analysis system," in *Electrical Engineering*. Pasadena: California Institute of Technology, 2000.
- [14] X. Q. Wang, A. Desai, Y. C. Tai, L. Licklider, and T. D. Lee, "Polymer-based electrospray chips for mass spectrometry," presented at the 12th IEEE International Conference on Micro Electro Mechanical Systems (MEMS 1999), Orlando, Florida, 1999.
- [15] M. J. de Boer, R. W. Tjerkstra, J. W. Berenschot, H. V. Jansen, C. J. Burger, J. G. E. Gardeniers, M. Elwenspoek, and A. van den Berg, "Micromachining of buried

- micro channels in silicon," *Journal of Microelectromechanical Systems*, vol. 9, pp. 94-103, 2000.
- [16] X.-Q. Wang, X. Yang, K. Walsh, and Y.-C. Tai, "Gas-phase silicon etching with bromine trifluoride," presented at Proceedings of the 1997 International Conference on Solid-State Sensors and Actuators. Part 2 (of 2), Chicago, IL, USA, 1997.
- [17] M. Liger, D. C. Rodger, and Y. C. Tai, "Robust parylene-to-silicon mechanical anchoring," presented at the 16th IEEE International Conference on Micro Electro Mechanical Systems (MEMS 2003), Kyoto, Japan, 2003.
- [18] C. Y. Shih and Y. C. Tai, "Single-mask technology for on-chip high-pressure HPLC system," presented at the 9th International Conference on Miniaturized Systems for Chemistry and Life Sciences, Boston, USA, 2005.
- [19] C. Y. Shih, W. Li, and Y. C. Tai, "A novel embedded liquid chromatography system with submicron-sized filter structure and capacitively-coupled contactless conductivity detector," presented at the 20th International Symposium on Microscale Bioseparations, Amsterdam, the Netherlands, 2006.
- [20] J. Xie, Y. N. Miao, J. Shih, Y. C. Tai, and T. D. Lee, "Microfluidic platform for liquid chromatography-tandem mass spectrometry analyses of complex peptide mixtures," *Analytical Chemistry*, vol. 77, pp. 6947-6953, 2005.

---

# CHAPTER 4

---

## TEMPERATURE-CONTROLLED MICROCHIP HPLC SYSTEM

### 4.1 Temperature Gradient Interaction Chromatography

Solvent gradient reversed-phase LC (RP-LC) is one of the most popular separation strategies utilized in proteomics or macromolecule separations [1]. Building a reliable and easy-to-use microchip RP-LC system is, however, a very challenging task. For example, in order to generate a high quality solvent gradient, the on-chip mobile-phase pumps need to output low and smoothly changing flow rates (<100 nL/min), which contribute to the right solvent gradient profile for separation. In order to achieve that, on-chip flow sensors need to be built for flow rate feedback control [1]. Also, thorough mixing among mobile phase solvents needs to be done in the micro scale within a relatively short time (less than a few seconds) [2].

On the other hand, it was found that a temporal temperature gradient (i.e., changing the LC column's temperature as a function of time) could be as effective as a solvent gradient in terms of mobile phase elution strength modulation. In other words, for exothermic interaction ( $\Delta H_0 < 0$ ) for the analyte molecules to transfer from the mobile phase to the stationary phase of the separation column, low temperature elution is equivalent to polar solvent elution and high temperature elution is equivalent to non-polar solvent elution. This phenomenon can be understood from the temperature  $T$  dependence of the analyte retention factor  $k$  as expressed in (4.1) (see 2.1.3.1 for derivation details) [3]:

$$\ln k = -\frac{\Delta G_0}{RT} + \ln \beta = -\frac{\Delta H_0}{RT} + \frac{\Delta S_0}{R} + \ln \beta \quad (4.1)$$

Besides, since analyte mass transfer efficiency can be improved by carrying out elution at higher temperature, the band-broadening effect caused by low mass-transfer efficiency can therefore be reduced. Furthermore, the chromatography backpressure can be reduced due to the smaller solvent viscosity at high temperature.

Using a temperature gradient to achieve or improve analyte separation is categorized as Temperature Gradient Interaction Chromatography (TGIC) [3-10]. Figure 4-1 shows the working principle of TGIC. When a chromatogram is carried out with isocratic elution at fixed temperature, it may occur that in the early elution period many peaks crowd together due to their small differences in retention times. It may also happen that some peaks take a long time to come out and show a significant band-broadening effect (Figure 4-1 (a)). Now, when the chromatogram is redone with a temporal temperature gradient (Figure 4-1 (b)), early peaks can separate better at low temperature due to the larger retention times and retention time differences among peaks

(according to (4.1)). Also, late peaks will come out faster at high temperature and have a reduced band-broadening effect.

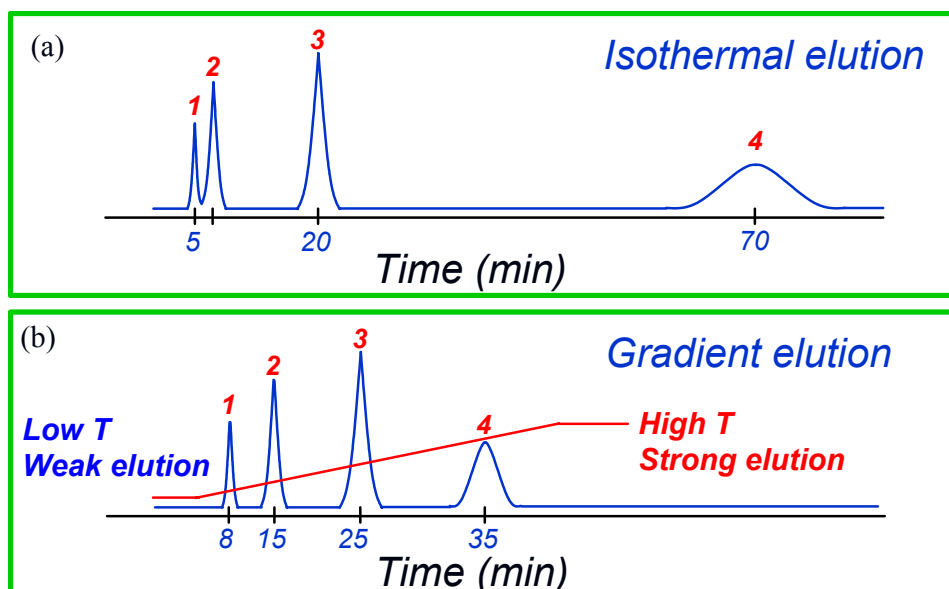


Figure 4-1: Working principles of TGIC. (a) Isothermal elution where temperature is fixed throughout the elution process. (b) Temperature gradient elution where elution temperature increases linearly from low temperature to high temperature.

Compared with a solvent gradient, a temperature gradient is much easier to carry out on a microchip HPLC system. On-chip heaters instead of on-chip pumps will be used to generate the gradient elution. Also, compared with a desktop TGIC system, which uses a column oven to control column temperature, microchip TGIC has much lower power consumption and much faster thermal response. In fact, chip-based TGIC system is extremely attractive [11] because of the fast and accurate on-chip temperature control by MEMS technology as has been demonstrated in microchip polymerase chain reaction (PCR) [12, 13]. Importantly, chip-based TGIC has never been demonstrated before. In this chapter, we introduce the integrated TGIC systems with a particle-packed separation

column, an electrochemical analyte sensor, a resistive heater for column temperature control, and thermal isolation structure for power-consumption reduction. Using the developed systems, we have successfully demonstrated the first microchip TGIC of amino acids.

## **4.2 Chip Design, Fabrication, and Characterization**

Two versions of TGIC microchips were designed to be used for different chromatography criteria. The first version microchip was designed to operate at lower power consumption (71 mW at 100 °C) and lower chromatographic backpressure (180 psi). The second version microchip was designed to operate at higher power consumption (400 mW at 100 °C) and higher chromatographic backpressure (600 psi).

### **4.2.1 Low-Power, Low-Pressure-Capacity System**

#### **4.2.1.1 Design and Fabrication**

The focus of this design is to minimize the power consumption of the temperature gradient operation. To achieve that, we have fabricated a freestanding LC column with an embedded heater using the process flow as shown in Fig. 4-2. The fabrication process starts with growing a 1.1- $\mu\text{m}$ -thick  $\text{SiO}_2$  layer on both sides of 4-inch silicon wafers (thickness: 525  $\pm$  25  $\mu\text{m}$ ) by thermal oxidation. Front side oxide is then patterned with buffer HF (Transene, Danvers, MA). 300 Å-titanium/2000 Å-platinum/1000 Å-gold is e-beam evaporated on wafer front side. Backside oxide is then patterned with buffer HF to define the 100- $\mu\text{m}$ -diameter liquid access holes. Using backside photoresist again as the mask, DRIE is used to etch backside silicon for 500  $\mu\text{m}$  and leave only a 50- $\mu\text{m}$ -thick

silicon membrane. Gold is then patterned with wet etchant (Transene, Danvers, MA). Here the gold layer is used to provide a surface for easy gold-wire bonding. Ti/Pt is then patterned with wet etchants (home-made aqua regia for Pt etching) to define the resistive heater and electrochemical sensor. 3.5- $\mu\text{m}$ -thick first parylene layer (Specialty Coating Systems, Indianapolis, IN) is deposited and patterned with oxygen plasma on the wafer front side as the column bottom wall. 25  $\mu\text{m}$  photoresist AZ4620 (Clariant, Somerville, NJ) is deposited and patterned on wafer front side to form a two-level photoresist structure using a double-exposure method [14]: one full exposure (first mask) and one partial exposure (second mask) are performed prior to developing the photoresist; particles filters and electrochemical sensing areas were partially exposed so to leave a 4- $\mu\text{m}$ -thick photoresist layer after developing; the unexposed photoresist forms the 25- $\mu\text{m}$ -thick sacrificial layer for the cross-section definition of the LC column and liquid inlet/outlet chambers; photoresist is then developed and a 100  $^{\circ}\text{C}$ -3 hr baking is carried out to avoid photoresist bubbling during latter thermal treatment where the photoresist is covered by a top parylene layer. Front side photoresist is then used as the DRIE mask to etch down silicon for a 15- $\mu\text{m}$ -wide, 30- $\mu\text{m}$ -deep trench with a mushroom profile in the trench bottom (by a modified DRIE Bosch process [15]). The trench-mushroom structure here is used as the anchoring space for parylene thin film deposition. A 10- $\mu\text{m}$ -thick second parylene layer is then conformally deposited on wafer front side, filling up the trenches and covering photoresist structures. Parylene is then patterned to create openings for later  $\text{XeF}_2$  etching. DRIE is carried out on wafer backside again to etch through the silicon wafer on the liquid-access-hole sites.  $\text{XeF}_2$  is then used on wafer front side (back side is protected with a glass wafer) to dry-etch silicon through parylene

openings and make the LC column freestanding. A 10- $\mu\text{m}$ -thick third parylene layer is then deposited on wafer front side to wrap up the freestanding column to enhance its pressure capacity. The wafer is then diced into 1.1 cm $\times$ 1.1 cm chips and photoresist inside the column is dissolved by 60  $^{\circ}\text{C}$ -24 hr acetone bath through liquid access holes. Parylene is then patterned with a silicon shadow mask to reveal gold contact pad on the chip front side. Fig. 4-3 shows the fabricated device.

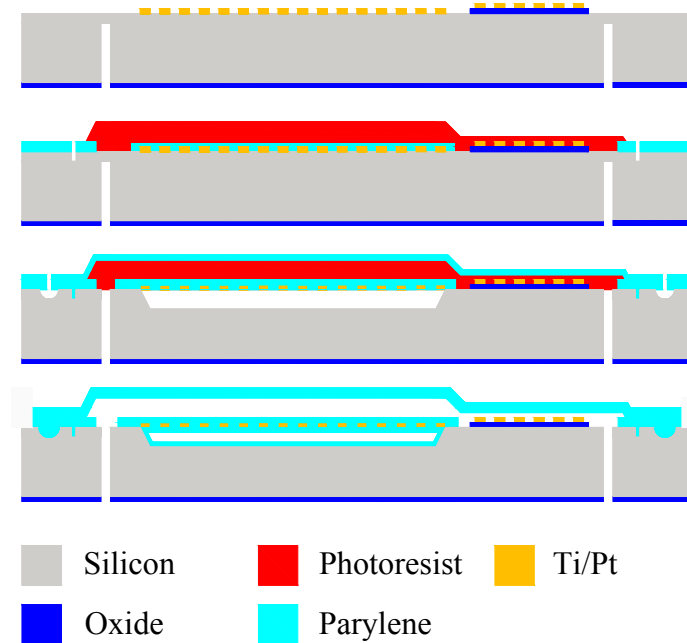


Figure 4-2: Process flow for the low-power, low-pressure-capacity TGIC microchip.

#### 4.2.1.2 System Characterization

The pressure capacity of this freestanding-type LC column was studied. In this channel configuration, the pressure-capacity weak point occurs at the parylene layer interface inside the freestanding column supporting beams (Figure 4-4). To achieve highest pressure capacity, several beam structures have been fabricated and tested. The design with the highest pressure capacity is shown in Figure 4-4, where the second

parlylene layer cuts through the first parlylene layer and avoids direct liquid penetration through the first/second parlylene interface under high pressure. This channel configuration provides highest pressure capacity of 180 psi. Channel failures come from the leakage or breaking around the channel supporting beams.

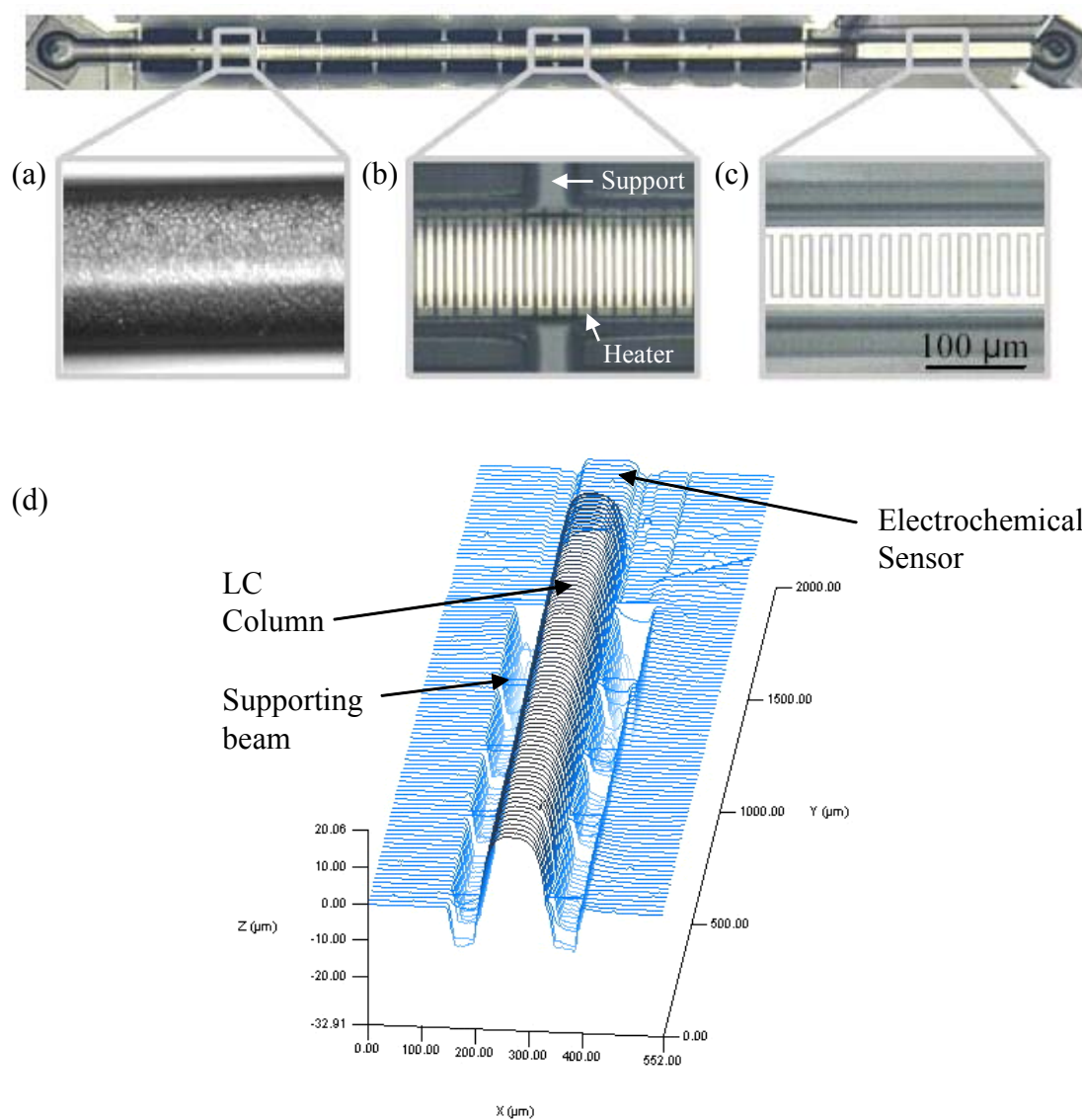


Figure 4-3: Photographs of the fabricated low-power, low-pressure-capacity TGIC device: (a) column section packed with 5- $\mu\text{m}$ -C18 silica particles, (b) freestanding column with imbedded heater and column supports, (c) interdigitated electrochemical sensor, (d) device topography taken by Tencor P15 surface profiler.

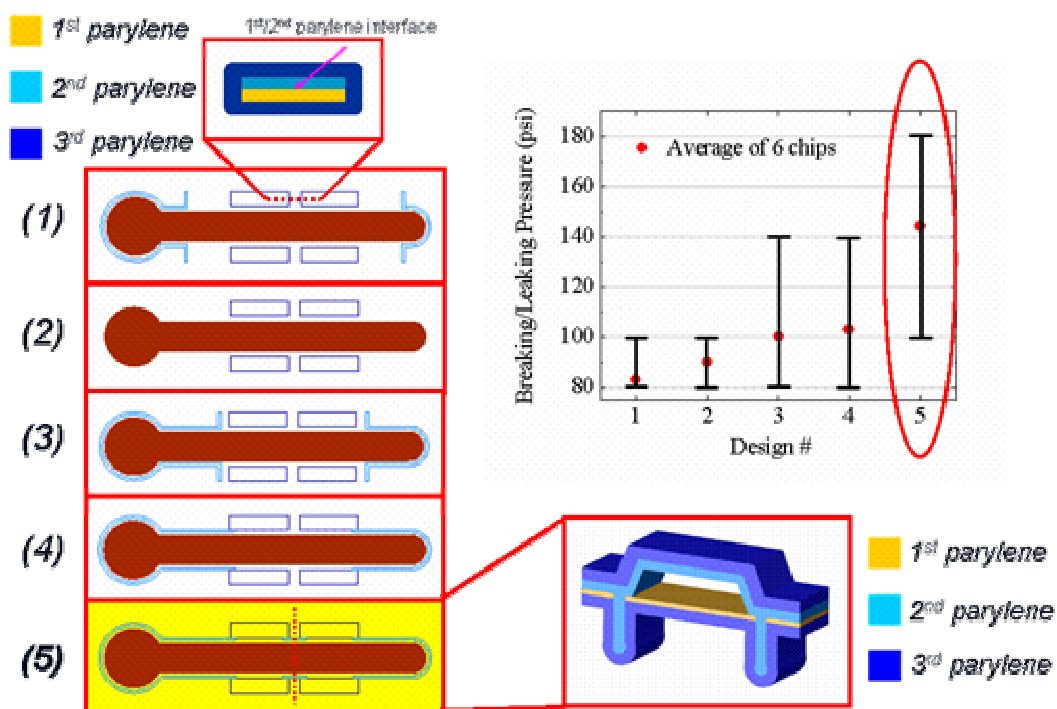


Figure 4-4: Different channel configurations for pressure capacity study. Design #5 provides highest pressure capacity up to 180 psi. Water was used in the testing as the loading solvent.

In order to determine the column temperature, the resistive platinum heater was used as a temperature sensor as well [16]. Since the heater is embedded in the bottom of the LC column, it is appropriate to assume the column temperature to be the same as the heater temperature. Based on the TCR (Temperature Coefficient of Resistance) experimental data of the platinum heater as shown in Figure 4-5, heater temperature can be derived from the heater resistance. The measured TCR is  $0.21\% \text{ K}^{-1}$  (with a reference resistance value obtained at  $20 \text{ }^{\circ}\text{C}$ ). Figure 4-6 then shows the column temperature versus power consumption curve. To operate at  $100 \text{ }^{\circ}\text{C}$  (under appropriate chromatographic packaging), the microchip consumes 71 mW.

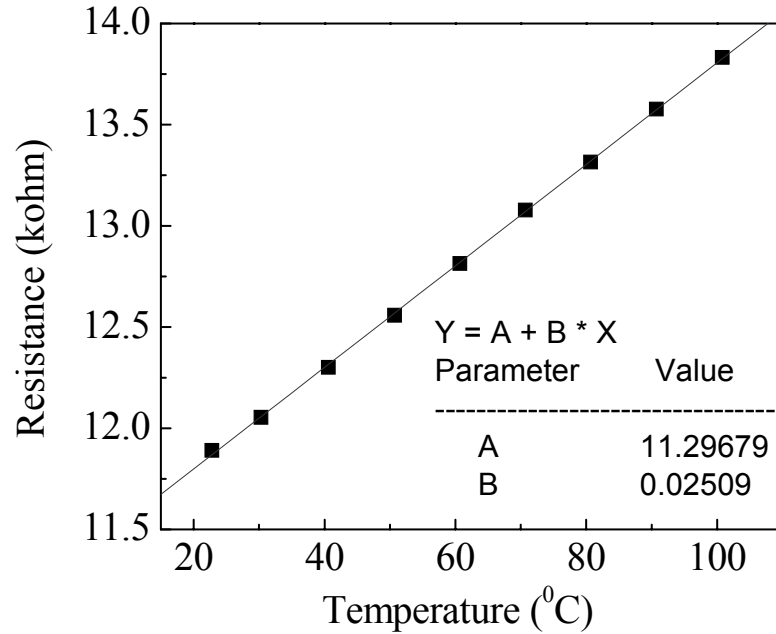


Figure 4-5: Temperature coefficient of resistance (TCR) characterization of Ti/Pt resistive heater.

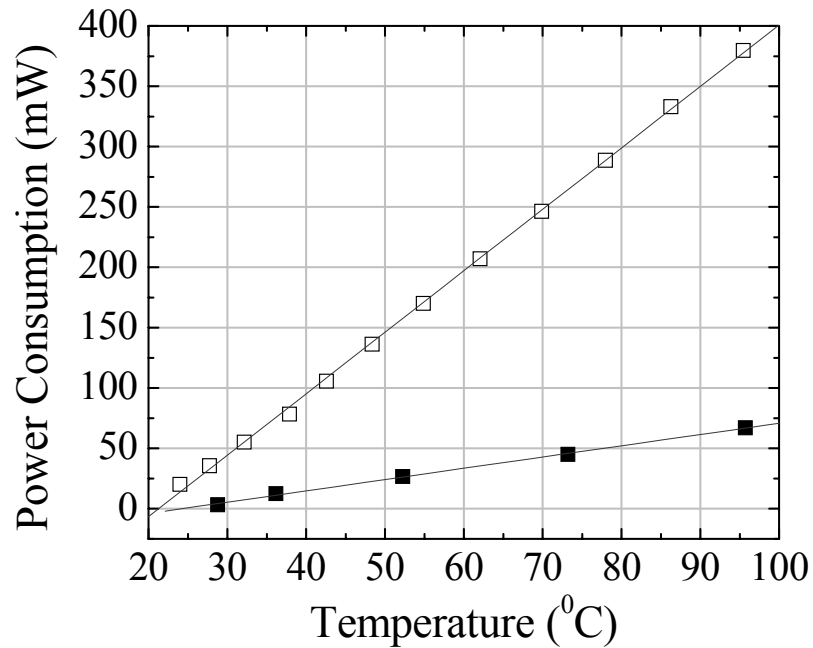


Figure 4-6: Power consumption comparison: (■) low-power-consumption device, (□) high-power-consumption device, which will be introduced in 4.2.2.

## 4.2.2 High-Power, High-Pressure-Capacity System

### 4.2.2.1 Design and Fabrication

The focus of this design is to have high pressure capacity (700 psi) for the LC column. To achieve that, the anchored-type parylene channel technology (introduced in 3.3.1) is used to compose the LC column. Due to the fact that the LC column is in contact with the silicon substrate, power consumption of this design is higher compared to the freestanding-type column design. To reduce power consumption, a novel parylene-strengthened air-gap thermal isolation structure is used that effectively reduces the power consumption by 58% [17].

As shown in Figure 4-7, the fabrication process starts with growing 1.1- $\mu\text{m}$ -thick  $\text{SiO}_2$  layer on both sides of 4-inch silicon wafers (thickness:  $525 \pm 25 \mu\text{m}$ ) by thermal oxidation. Double-layered photoresist composing the first layer of liftoff photoresist LOR3B (Microchem, Newton, MA) and the second layer of AZ1518 (Clariant, Somerville, NJ) is deposited on the wafer front side. Photoresist is patterned to define heater and electrochemical sensor patterns. 300 Å-titanium/2000 Å-platinum/1000 Å-gold is e-beam evaporated on wafer front side. Metal is then lifted off by dissolving photoresist in photoresist stripper (ATMI, San Jose, CA) at 60 °C for 2 hr. Gold is then patterned with a wet etchant (Transene, Danvers, MA). Again, gold is only used to provide a surface for easy gold-wire bonding. Backside oxide is then patterned with buffer HF (Transene, Danvers, MA), which defines the 100- $\mu\text{m}$ -diameter liquid access holes and 150- $\mu\text{m}$ -wide air gap for thermal isolation. Without removing photoresist on top of the backside oxide, DRIE is used to etch backside silicon for 450  $\mu\text{m}$ . Front side oxide is then patterned. 25  $\mu\text{m}$  photoresist AZ4620 (Clariant, Somerville, NJ) is

deposited and patterned on wafer front side to form a two-level photoresist structure using a double-exposure method introduced earlier. A 100 °C-3 hr baking is carried out to avoid photoresist bubbling during latter thermal treatment where photoresist is covered by a parylene layer. Front side oxide and photoresist are then used together as DRIE mask to etch down silicon for a 30- $\mu\text{m}$ -deep, 15- $\mu\text{m}$ -wide trench with a mushroom profile in the trench bottom (by a modified DRIE Bosch process [15]). 10- $\mu\text{m}$ -thick parylene is then conformally deposited on wafer front side, filling up the trenches and covering photoresist structures. Parylene is then patterned with oxygen plasma. DRIE is carried out on wafer backside again to etch through the silicon wafer for liquid access channels and thermal-isolation air gaps. Finally, the wafer is diced into 1.1 cm $\times$ 1.1 cm chips and photoresist inside the column was dissolved by 60 °C-24 hr acetone bath through liquid access holes. Figure 4-8 shows the details of the fabricated devices.

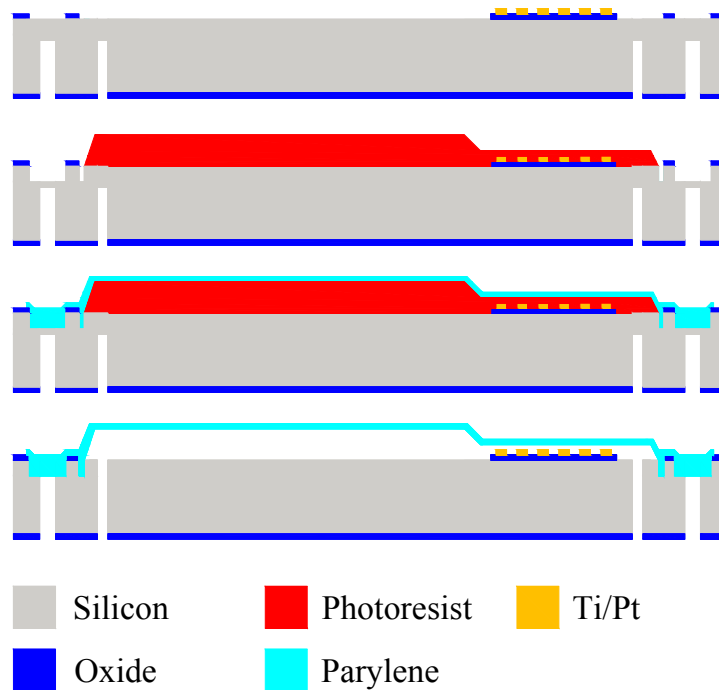


Figure 4-7: Process flow for the high-power, high-pressure-capacity TGIC microchip.

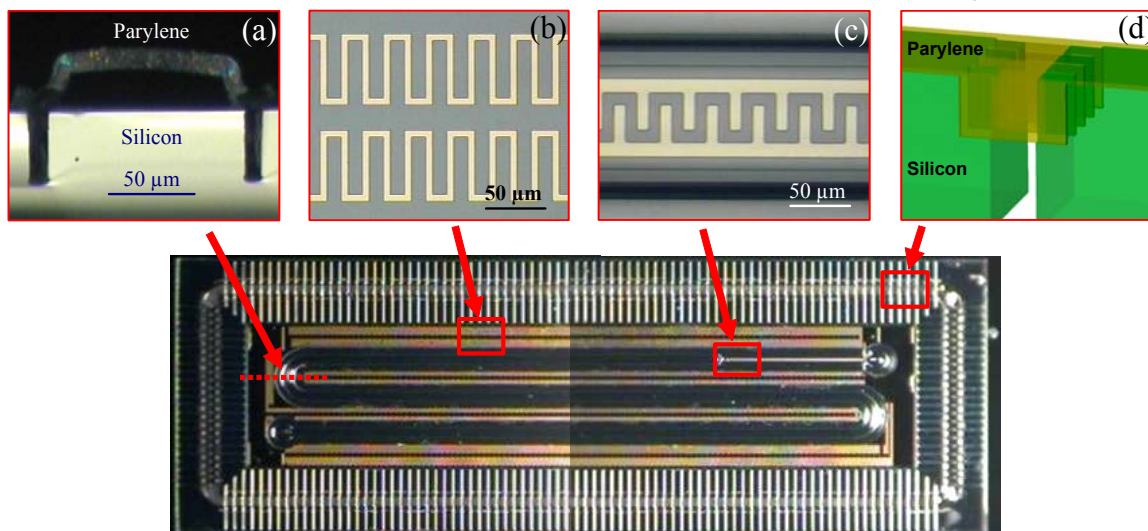


Figure 4-8: Photographs of the fabricated high-power, high-pressure-capacity TGIC device. (a) Column cross-section, (b) resistive heater, (c) electrochemical sensor, and (d) thermal isolation structure.

The sensor cell is 100- $\mu\text{m}$ -wide, 4- $\mu\text{m}$ -high and 1650- $\mu\text{m}$ -long, which corresponds to a cell volume of 0.66 nL. The interdigitated Ti/Pt electrode fingers are 10- $\mu\text{m}$ -wide with 10- $\mu\text{m}$ -wide intervals. The length of each finger is 30  $\mu\text{m}$ . The electrochemical sensor geometry was designed according to the principle that the total electrode area was maximized so to increase the possibility that analyte molecules diffuse to the electrode surface where the electrochemical reaction happens before the analyte molecules are flushed out from the sensor area. Based on this principle, the space between electrode fingers was minimized and the finger length, sensor length were maximized as much as possible. While the sensor length is relatively long (20% of the separation column length), the analyte molecules spend only 19.8 msec to pass through the sensor area given a flow rate of 2  $\mu\text{L}/\text{min}$  and therefore no significant band-broadening will be caused by this sensor geometry. The distributed Ti/Pt resistive heater

runs between parylene columns and has a 10  $\mu\text{m}$  line width and a total resistance of about 12  $\text{k}\Omega$  at 25  $^{\circ}\text{C}$ .

The parylene-anchoring technique mentioned earlier was also used to provide a robust cross-linking support to the air-gap-surrounded column area (island) as shown in Figure 4-9. Robust mechanical support to the island is necessary in order to withstand the stress generated on the chip during chip-packaging and wire-bonding procedures. Since parylene has a very low thermal conductivity of 0.08  $\text{W/m}\cdot\text{K}$  (compared with 0.03  $\text{W/m}\cdot\text{K}$  of static air) and a high elongation limit of 200%, parylene-cross-linking structure provides a durable mechanical support to the column island while not much heat is conducted through itself during temperature gradient operation.

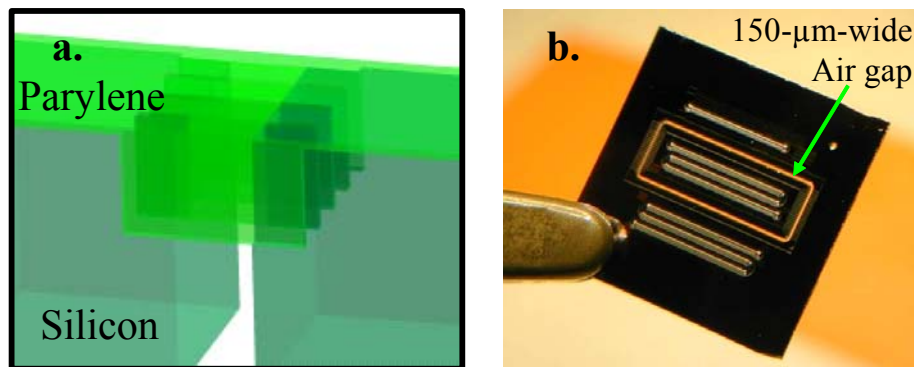


Figure 4-9: (a) Illustration of parylene-cross-linking structure, (b) a photograph showing the fabricated 150- $\mu\text{m}$ -wide, wafer-thickness air gap and the thermally isolated silicon temperature zone (center piece).

#### 4.2.2.2 System Characterization

From earlier studies we have verified that the anchored parylene column structure can stand an inner pressure of 700 psi without fracture [14]. To further make sure that parylene thin film will not reach the plastic deformation regime during high pressure

operation such as particle-packing, we studied the stress distribution inside the parylene column wall under a 200 psi uniform pressure loading with a FEMLAB simulation (Figure 4-10). Results show that the maximum stress is 50 MPa, which occurs around the inner corner of the column wall. Since parylene thin-film yield stress is 59 MPa [18], we are assured that the parylene column will not have plastic deformation during particle-packing or separation tasks when operated under 200 psi.

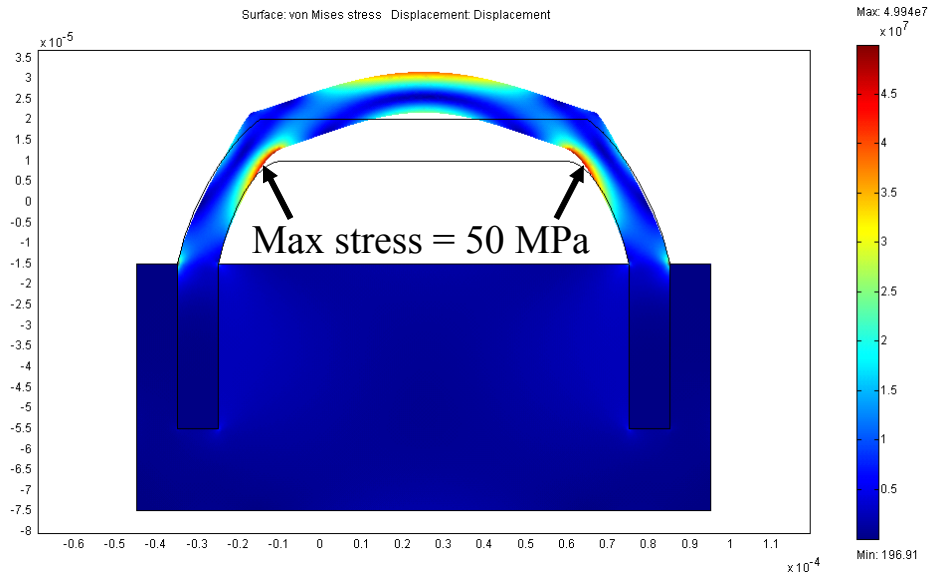


Figure 4-10: FEMLAB simulation showing stress distribution inside the 10- $\mu\text{m}$ -thick parylene column wall under a 200 psi uniform pressure loading.

Thermal isolation efficiency of the parylene-strengthened air-gap structure was further studied. Results show that heater power consumption is reduced by 58% when the column is surrounded by the air-gap thermal isolation structure (Figure 4-11). Also, the temperature rise around the off-island area was greatly reduced by 67% compared with the on-island area during temperature gradient operation (Figure 4-12). With the off-island cooling feature available, it is feasible to lay out the electrochemical sensor in

the cooling area if sensing needs to be done at low temperature. Chip thermal performance can be further improved by either increasing the air-gap width (better thermal isolation) or reducing the island overall area (reduced thermal mass).

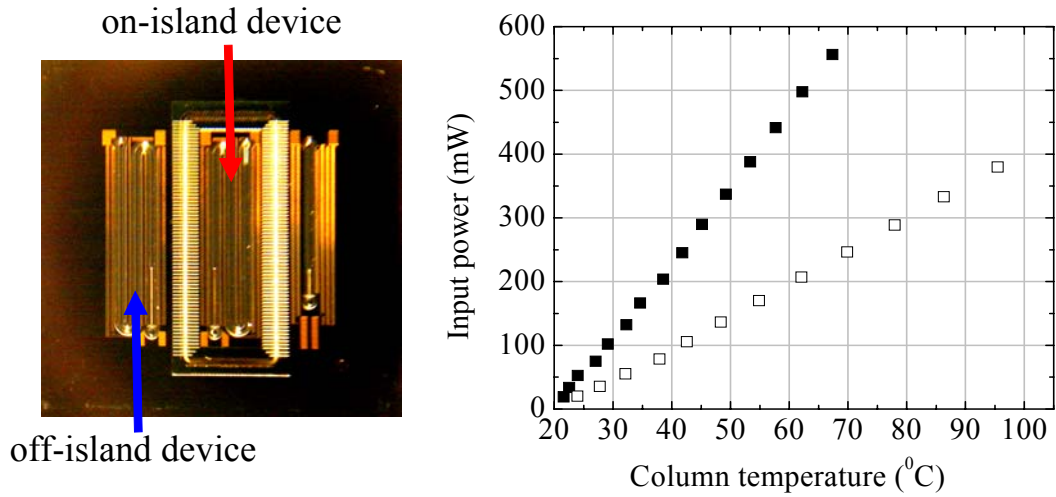


Figure 4-11: Power consumption comparison: (■) column without thermal isolation structure (off-island device), (□) column surrounded by parylene-strengthened air-gap thermal isolation structure (on-island device).

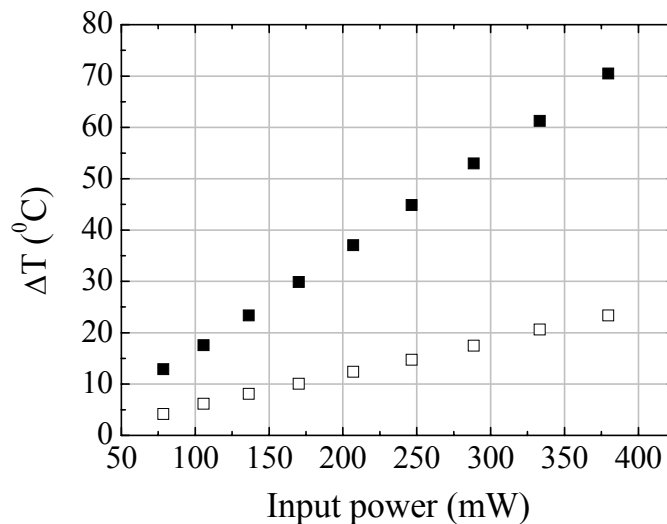


Figure 4-12: On-chip temperature rise ( $\Delta T$ ) spatial distribution during temperature gradient operation: (■) air-gap-surrounded island area, (□) off-island area.

A FEMLAB simulation was used to study the mechanical rigidity of the parylene-strengthened thermal isolation structure. A uniform pressure loading of 100 psi is applied to the bottom of the thermally isolated silicon piece, which is supported by parylene cross-linking structure as shown in Figure 4-13. The island is 1-mm-wide and 2-mm-long; thermal isolation air-gap width is 100  $\mu\text{m}$  and DRIE trench width is chosen as the variable with an interval size between trenches of 100  $\mu\text{m}$ . Real geometries from the chip are not used in this simulation due to the fact that much higher computation power will be necessary for that simulation. Results indicate that vertical displacement of the silicon island decreases exponentially with increasing DRIE trench depth as shown in Figure 4-14. In addition to increasing DRIE trench depth, the structure rigidity can also be enhanced by reducing air-gap width or DRIE trench interval size.

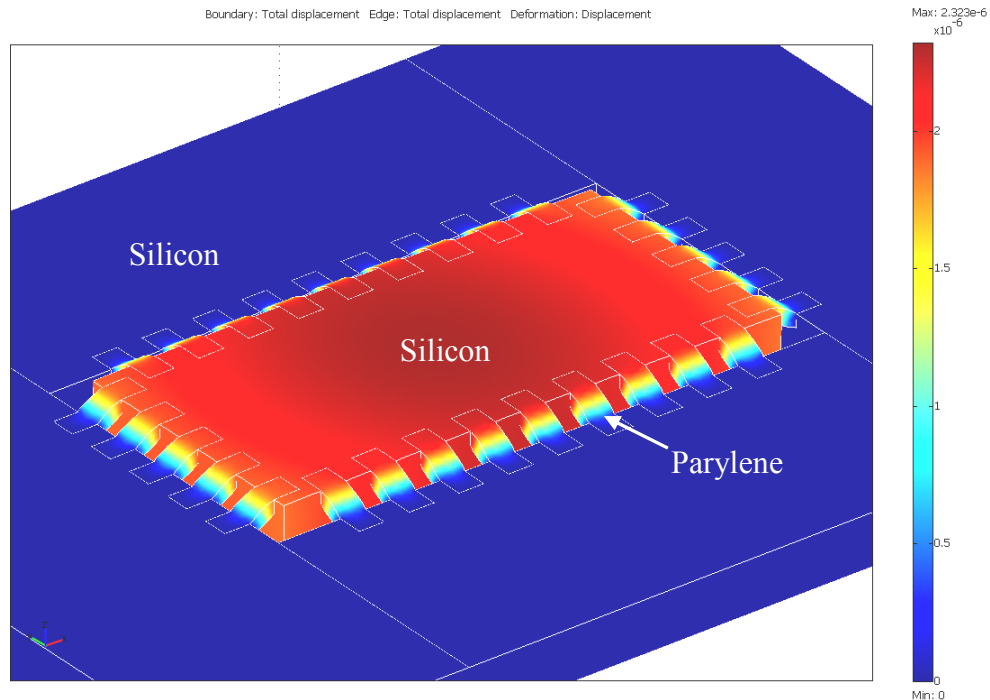


Figure 4-13: FEMLAB simulation showing an exaggerated vertical displacement of the thermally isolated silicon island loaded with uniform pressure from underneath.

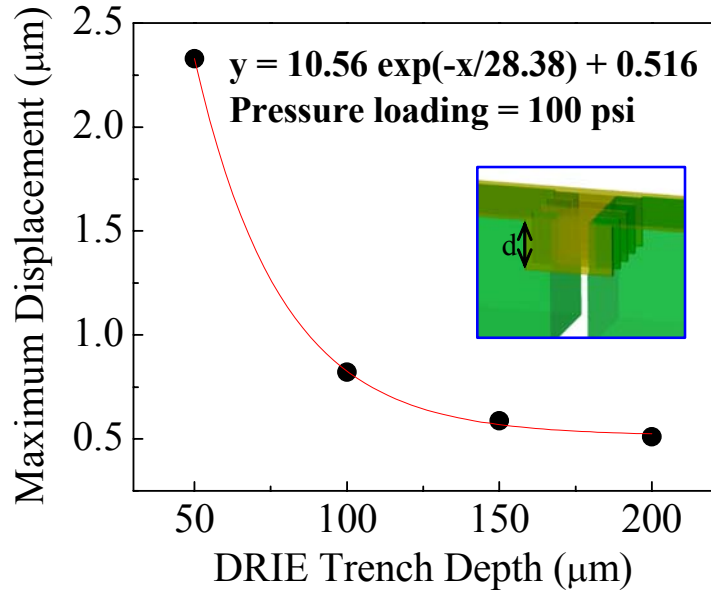


Figure 4-14: FEMLAB simulation showing vertical displacement of the thermally-isolated silicon island as a function of DRIE trench depth “d”. Pressure loading to the island bottom was 100 psi.

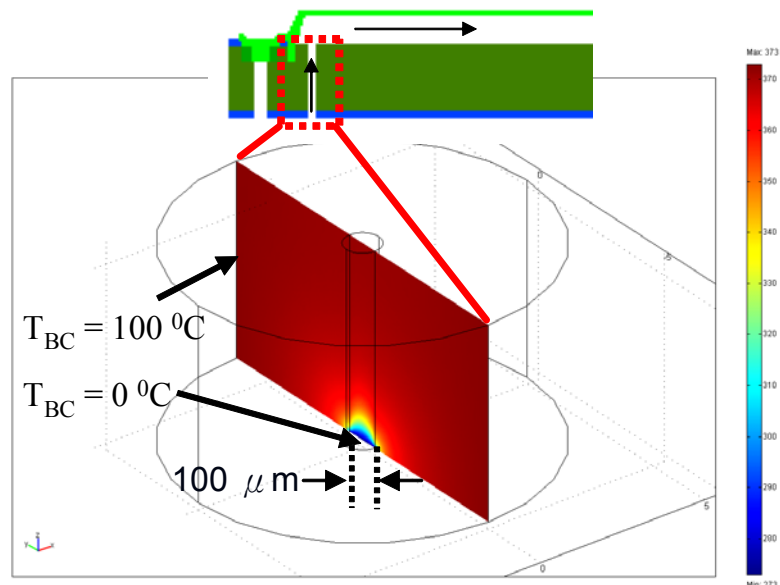


Figure 4-15: FEMLAB simulation showing flow-preheating around the silicon-made liquid access channel. Linear flow velocity used is 4.2 mm/sec and liquid is water.  $T_{BC}$  is the temperature boundary condition used in the simulation.

One important factor to achieve quality TGIC performance is the mobile-phase solvent temperature control. In other words, mobile-phase solvent should be heated up to the desired gradient temperature before it enters the separation column. For a conventional HPLC system to achieve solvent preheating, an extra solvent-preheating column is required [19, 20]. For our microchip TGIC system, however, solvent-preheating is automatically achieved. Based on the FEMLAB simulation result as shown in Figure 4-15, solvent is heated up to the desired temperature inside the silicon-made liquid access channel far before it enters the HPLC column.

#### **4.2.2.3 Application of Parylene Thermal Isolation Technology**

Silicon is a fundamental structural material in MEMS with a very high thermal conductivity of 148 W/m-K (compared with 73 W/m-K of iron). This specific thermal property guarantees great on-chip temperature uniformity; however it also generates design complexity for applications where multiple temperature zones are required on a single silicon chip. Some representative lab-on-a-chip applications that require multiple on-chip temperature zones are continuous-flow polymerase chain reaction [21] and micro-bioreactor [22]. Ideally, for best temperature uniformity of each temperature zone on the silicon substrate, no silicon connection should remain between temperature zones and therefore a wafer-thickness-deep, temperature-zone-surrounding thermal isolation structure needs to be built on the chip. Moreover, electrical and fluidic connection among temperature zones should be available for versatile application needs. While several thermal isolation technologies have been developed (Figure 4-16), the aerogel or porous silicon approach in general provides only vertical direction thermal isolation [23];

the floating membrane structure, which uses thin dielectric layer to hold freestanding temperature zone, is mechanically fragile and cannot stand much stress and strain encountered during device fabrication or testing procedures [24]; the oxide-filled trench structure has only limited thermal isolation efficiency due to the still high thermal conductivity of oxide (1.4 W/m-K for silicon dioxide) and the limited oxide thickness [25]. Our parylene-strengthened thermal isolation technology introduced earlier in this chapter provides a solution to those issues.

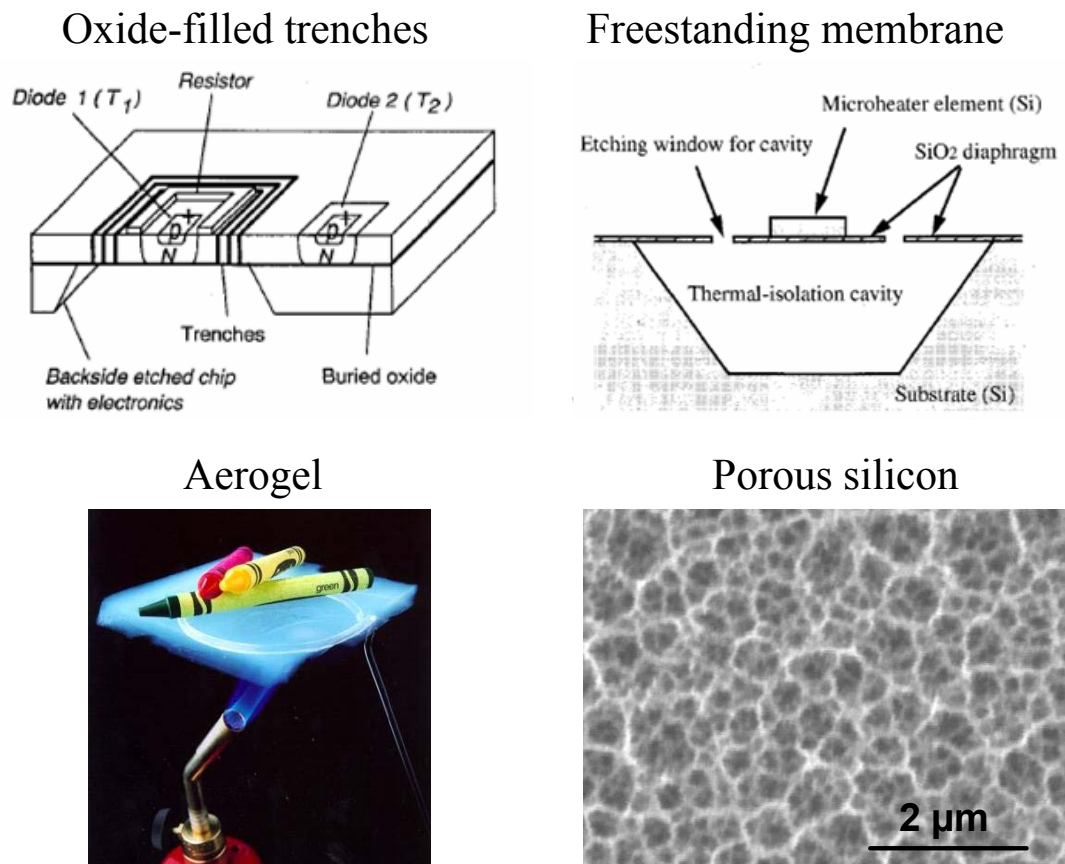


Figure 4-16: Some representative thermal-isolation technologies.

As follows is another example showing how our parylene-strengthened thermal isolation technology can be used. The continuous-flow polymerase chain reaction

requires the DNA sample solution to periodically pass through three temperature zones including the high temperature zone (94 °C) for double-strand DNA (dsDNA) melting, the low temperature zone (60 °C) for primer annealing, and the medium temperature zone (72 °C) for primer extension [21]. With our thermal isolation technology, three temperature zones defined by air gaps were created on the silicon substrate as shown in Figure 4-17. Each temperature zone had its individual resistive heater for independent and precise temperature control. In our design, 10 PCR cycles were prepared on a 8 mm×8 mm chip area with a flowing-through time ratio among three temperature zones of 1:1:1.5 (melting : annealing : extension). The PCR-time-ratio among temperature zones was defined by the fluidic-channel-length-ratio among temperature zones. The absolute flowing-through time can be controlled by the off-chip pumping flow rate. Figure 4-18 then shows the thermal image of the powered-up PCR temperature zones taken by an IR microscope (InfraScope™). While it is true that 10 cycles are in general not enough for PCR applications, our technology can be easily scaled up to have twenty or more cycles by using a larger chip space for fluidic channel routing.

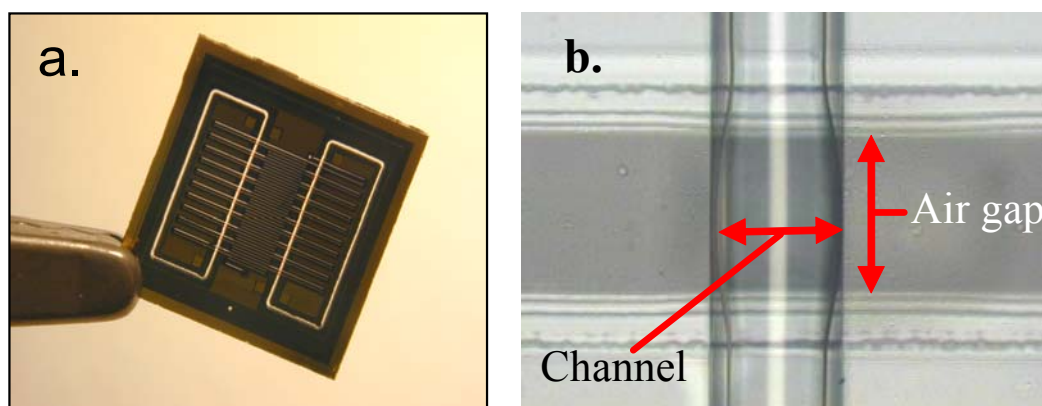


Figure 4-17: (a) Three temperature zones created by two air-gap rings on a silicon substrate for continuous-flow PCR applications, (b) a photograph showing the microfluidic channel crossing the air gap between temperature zones.

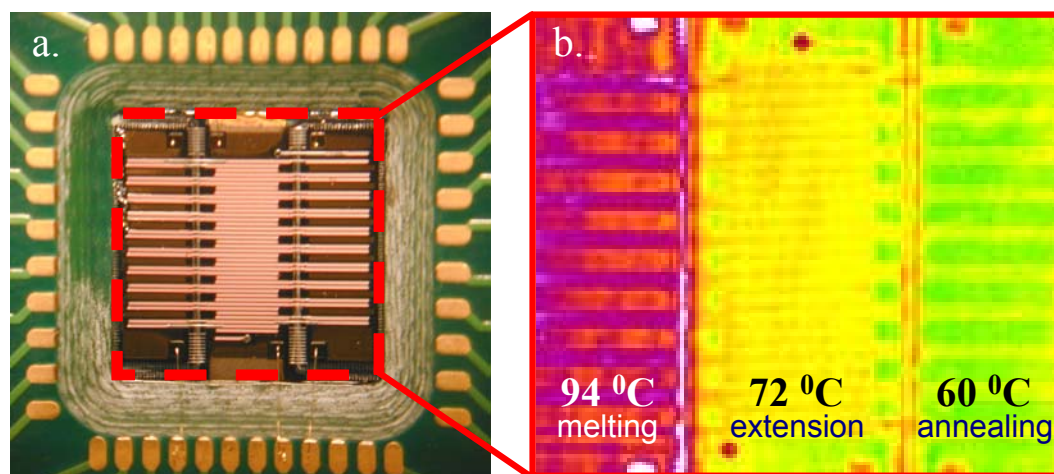


Figure 4-18: (a) The packaged continuous-flow PCR device with 10 PCR cycles, (b) thermal image of the powered-up PCR device. Temperatures were read out from heater resistances via their TCR data.

### 4.3 TGIC Chip Packaging

Fluidic and electrical access to the TGIC chip was achieved with a custom-made microfluidic jig and printed circuit board (PCB) as shown in Figure 4-19. The jig was made of PEEK (polyetheretherketone) purchased from McMaster-Carr (Los Angeles, CA), which is inert to most chemicals/solvents used in HPLC and is suitable for precise microfluidic-port machining. Fluidic tubing and fittings were purchased from Upchurch Scientific (Oak Harbor, WA). O-rings with an inner diameter of 0.5 mm and an outer diameter of 1.5 mm were purchased from Apple Rubber Products (Lancaster, NY). After O-rings and TGIC chip are placed in the recesses of the PEEK jig, PCB is screwed down to press on the chip against O-rings and results in gas-tight sealing around the interfaces. Pressure capacity of this chip packaging has been tested up to 1,000 psi with negligible fluidic leak rate. Electrical access to the chip is made by wire-bonding from the PCB to

the chip. Peltier cooler (Melcor, Trenton, NJ) can be optionally put on top of PCB to provide chip cooling when low background temperature is required [26].

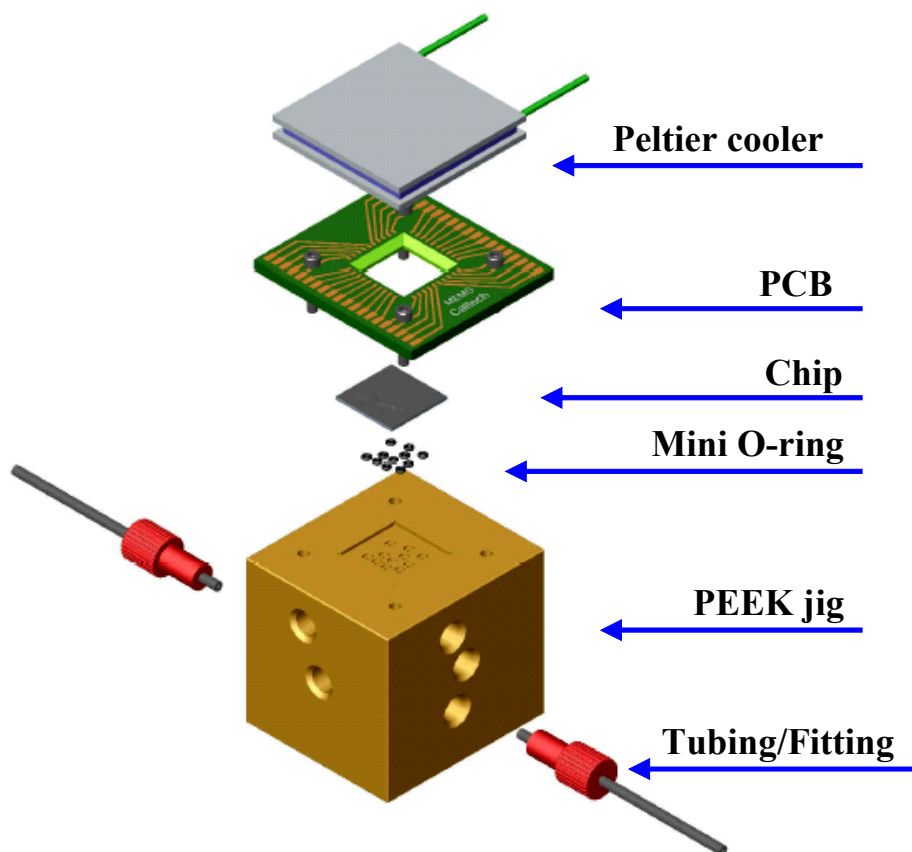


Figure 4-19: Exploded view of chip-packaging for chromatography tasks.

#### 4.4 Stationary-Phase Particle Packing

Column particle-packing was achieved with a conventional slurry-packing technique [14]. In order to get quality and repeatable separation, column packing has to be uniform and void-free, which means packing needs to be done with high pressure (200 psi in this work for an 8 mm column length [14]). The packing slurry is prepared by mixing 5- $\mu\text{m}$ -C18 silica particles (Grace Vydac, Anaheim, CA) with IPA, followed by agitating the mixture with a vortexer (Scientific Industries, Bohemia, NY) to homogenize

the solution. The slurry is sucked into a Teflon tubing section via a syringe. The tubing is then connected to the jig microfluidic port in one end and the other end is connected to a 200 psi filtered nitrogen gas pressure source. The slurry is then injected to the column where the particles are stopped by the 4- $\mu\text{m}$ -high filter structure and start to pack in the column as shown in Figure 4-20. The column lengths packed with particles in this chapter were 8 mm.

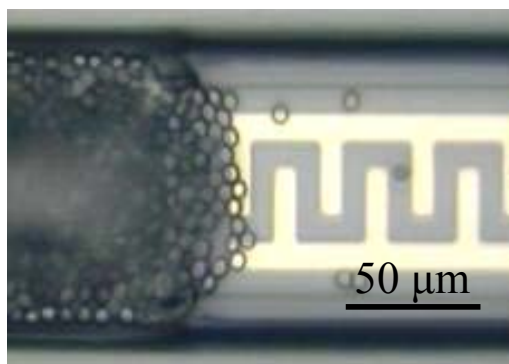


Figure 4-20: Parylene column packed with 5- $\mu\text{m}$ -C18 silica particles using 200 psi nitrogen gas pressure source. Particles got filtered by the 4- $\mu\text{m}$ -high filter structure.

#### 4.5 Chip Temperature Programming

For basic TGIC operation, a constant temporal temperature gradient should be generated in the separation column. To do so, a power that increased linearly with time was input to the on-chip distributed heater. In this chapter, a LABVIEW program was used to control a Keithley 230 function generator to output a linear power to the heater (Figure 4-21) and generate the desired constant temperature gradient. The temperature programming used here does not have feedback control or much temperature-programming flexibility. A much more advanced temperature-control LABVIEW program will be introduced in chapter 5.

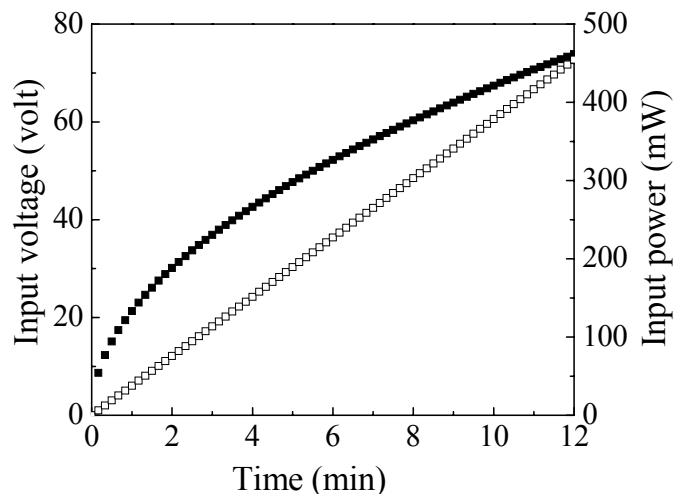


Figure 4-21: Power/voltage input profile to generate on-chip constant temperature gradient: (■) input voltage,  $V = (c \cdot R \cdot t)^{1/2}$ , where  $R$  is the heater resistance ( $\sim 12 \text{ k}\Omega$ ),  $t$  is time and  $c$  is a constant related to power slope, (□) input power,  $P = c \cdot t$ .

## 4.6 Examples of Separation

In this section, we demonstrate two examples using the fabricated TGIC microchips (the high-pressure-capacity version devices) to separate biomolecules. The first example is amino acid separation and the second example is low density lipoprotein separation.

### 4.6.1 Amino Acid Separation

#### 4.6.1.1 Introduction

Amino acid analysis has an important role in the study of the composition of proteins, foods, and feedstuff. Free amino acids are also determined in biological material, such as plasma and urine. When it is performed on a pure protein, amino acid analysis is capable of identifying the protein. It is also a useful method for quantitating

the amount of protein in a sample and gives more accurate results than colorimetric methods [27]. Being able to carry out amino acid analysis using a microchip HPLC system and a simple chromatographic procedure like TGIC therefore has important application values.

#### **4.6.1.2 Sample Preparation**

Amino acids, Iodoacetamide (IAA), o-phthaldialdehyde (OPA), 2-methyl-2-propanethiol (tert-butyl thiol), boric acid, and all buffer salts were purchased from Sigma-Aldrich (St. Louis, MO) of the highest purity available. HPLC-grade water, acetonitrile, and methanol were used for solution preparation. Solution preparation [28]: the 0.4 M borate buffer was made by dissolving 0.371 g of boric acid and 0.226 g of NaOH in 15 mL of water. The 0.05 M phosphate buffer was made by dissolving 0.218 g of  $\text{NaH}_2\text{PO}_4 \cdot \text{H}_2\text{O}$ , 0.318 g of  $\text{Na}_2\text{HPO}_4 \cdot 7\text{H}_2\text{O}$  and 14.9 mg of EDTA in 40 mL of water. OPA/tert-butyl thiol solution was made by adding 21.5 mg of OPA and 2.25  $\mu\text{L}$  of tert-butyl thiol into a solution containing 2 mL of borate buffer and 2 mL of methanol. IAA solution was made by dissolving 0.79 g of IAA into 4 mL of methanol. Sulfite solution was made by mixing 74.8 mg of cysteic acid, 50.4 mg of  $\text{Na}_2\text{SO}_3$ , and 4 mL of borate buffer. All solutions were made and stored in pre-cleaned plastic tubes. Derivatization [28]: the 12.5 mM amino acid sample was made by first adding 35.6 mg of ALA, 30.0 mg of GLY, 42.0 mg of SER, 47.7 mg of THR, and 72.5 mg of TYR into 20 mL of phosphate buffer. 4 mL of OPA/tert-butyl thiol solution was then added into the sample to start the derivatization. After 2 min, 4 mL of IAA solution was added to the sample when the amino acids were fully derivatized. After 4 min, 4 mL of sulfite solution was

added when the excess tert-butyl-thiol had been scavenged by IAA and the sample was allowed to sit for another 10 min before usage.

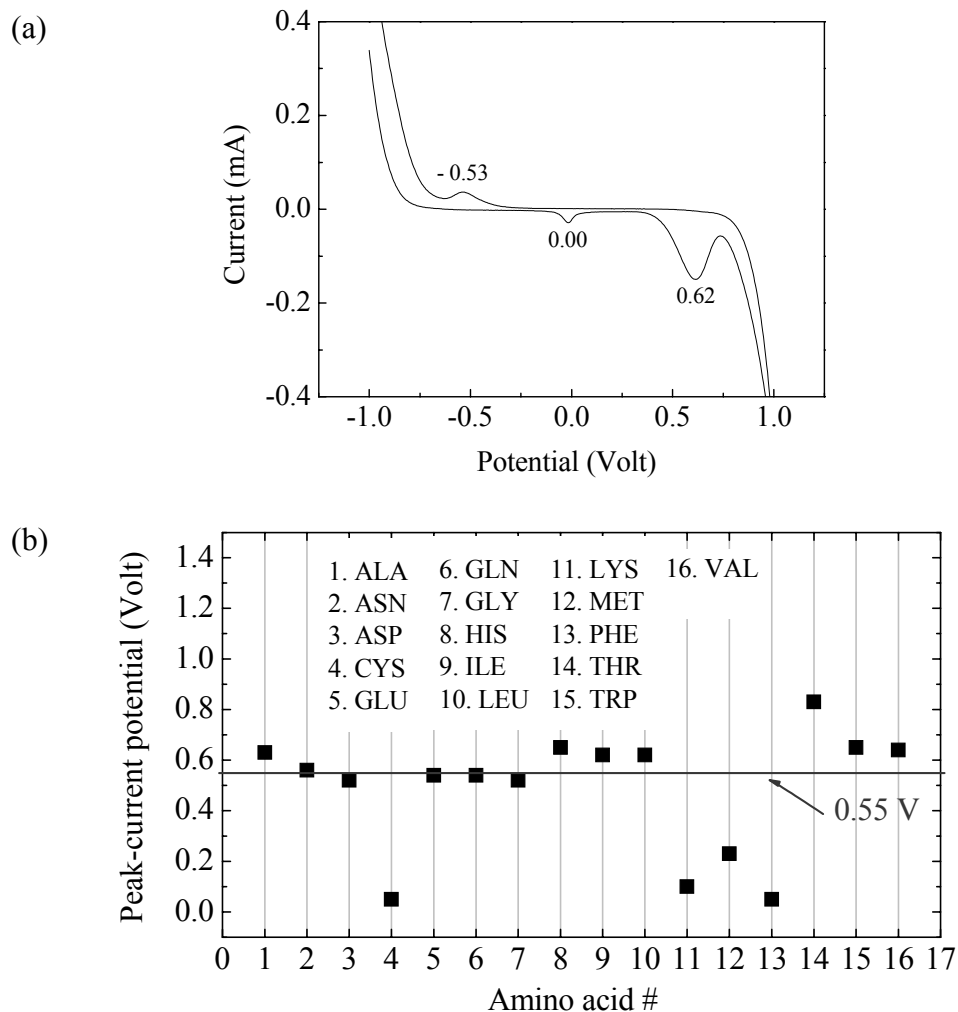


Figure 4-22: Cyclic voltammetry characterization of the derivatized amino acids. (a) Typical cyclic voltammetry of derivatized amino acid at 23 °C. A peak-current potential of 0.62 V was obtained from this CV for ALA. A sample solution that contained 12.5 mM ALA was prepared according to the procedure described in 4.6.1.2. The electrochemical cell was a two-wire-platinum-electrode cell with wires separated by 5 mm. Potential scan rate was 50 mV/s. (b) CV peak-current potential statistics of derivatized amino acids.

#### 4.6.1.3 Electrochemical Detection

To make sure that the derivatized amino acids were electroactive, cyclic voltammetry (CV) of derivatized amino acids was carried out by a potentialstat (EG&G, Princeton, NJ) as shown in Figure 4-22 (a). An average peak-current potential of 0.55 V was obtained from CVs of derivatized amino acids (Figure 4-22(b)) and was used as the input voltage to the microchip electrochemical sensor during the separation test.

#### 4.6.1.4 Separation Results and Comments

High-pressure-capacity HPLC microchips introduced in 4.2.2 were used in the amino acid separation test. The column was packed with 5  $\mu\text{m}$ -C18 porous particles and the dimensions were 25 $\mu\text{m}$ x100 $\mu\text{m}$ x8mm. Phosphate buffer as prepared in 4.6.1.2 with a pH value of 6.5 was used as the separation mobile phase. 20  $\mu\text{L}$  of derivatized amino acid sample that contained 12.5 mM of ALA, GLY, SER, THR, and TYR was first injected to the separation column with a flow rate of 2.0  $\mu\text{L}/\text{min}$  by a syringe pump (Harvard Apparatus, Holliston, MA). Sample volume was defined by the sample injection valve with a 20  $\mu\text{L}$  sample loop (Rheodyne, Rohnert Park, CA). The mobile phase was then injected to the column at 2.0  $\mu\text{L}/\text{min}$  for 10 min before temperature gradient was applied. Column temperature ramped up from 25  $^{\circ}\text{C}$  to 65  $^{\circ}\text{C}$  with a ramping rate of 3.6  $^{\circ}\text{C}/\text{min}$  during the separation test. As shown in Figure 4-23, the electrochemical sensor formed a circuit loop with the 0.55 V DC voltage source and the HP34970A data acquisition unit, which has an internal resistance of 10 M $\Omega$  under DC voltage measurement mode. When an amino acid peak passed through the electrochemical sensor, sensor resistance decreased due to the electrochemical reaction

and therefore more voltage drop was left on the internal resistance of the HP34970A data acquisition unit. HP34970A detected the voltage drop across its internal resistance and output the reading to a personal computer where chromatograms were recorded. As shown in Figure 4-24, we successfully demonstrated the first microchip TGIC of amino acids. Peak assignments in the chromatogram were based on the hydrophobicity ranking of the derivatized amino acids [28].

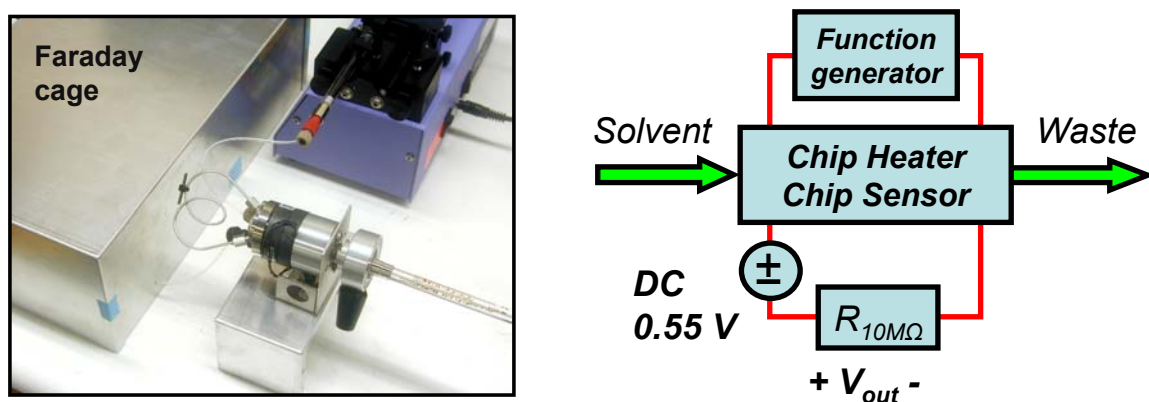


Figure 4-23: System setup for amino acid separation.

It should be noted from Figure 4-24 that serious band-broadening of peaks occurred in the separation process, which was mainly caused by the large sample injection volume (20  $\mu\text{L}$ ) and high sample concentration (12.5 mM). The separation performance can be improved by optimizing chromatographic parameters including sample volume, sample concentration, mobile-phase flow rate, and mobile-phase composition. Also, the reasons that the peak intensity (as well as peak area) varied a lot from one amino acid to another while the species concentrations were the same for all amino acid species are manifold. First, the electrochemical reactivity of the OPA-derivatized amino acid differs from one species to the other under the same electrochemical potential (0.55 V) since each derivatized amino acid has different peak-

current potential from our CV data. Second, the electrochemical reaction constant as well as the chemical structure stability of OPA-derivatized amino acids were both functions of the temperature; therefore during the temperature gradient period the overall electrochemical reactivity for each amino acid species can vary as well.

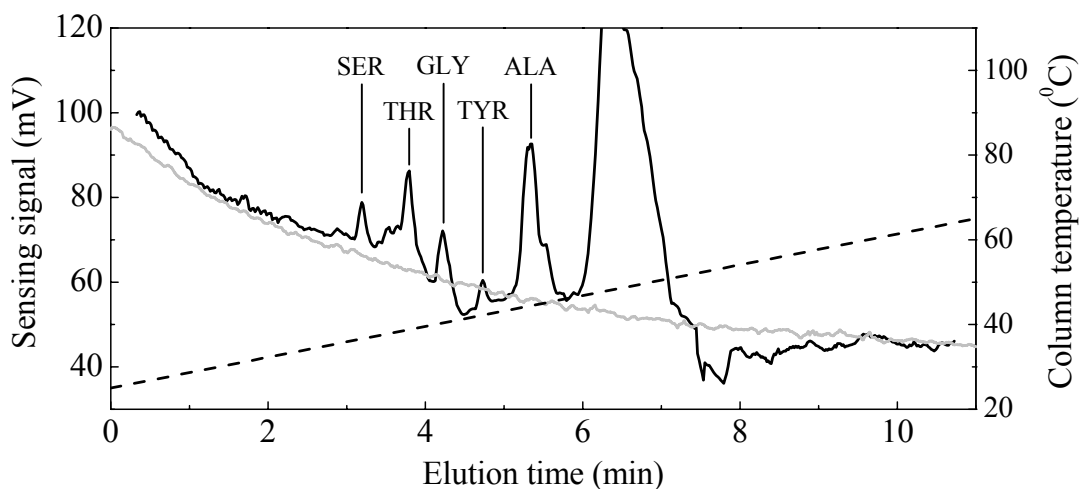


Figure 4-24: Chromatogram showing derivatized amino acids separated using temperature gradient elution: (black line) temperature gradient elution, (gray line) isothermal elution with column temperature fixed at 25 °C throughout the separation; no peak was eluted for isothermal elution, which was likely due to the large retention factor of derivatized amino acids in C18 column at room temperature, (dashed line) temporal temperature gradient, which was applied to the column during separation.

Even though in this work the amino acid derivatization procedure was carried out manually using off-chip procedures, it is feasible to integrate the derivatization functionality to the chip and simplify the sample preparation process [29]. Also, while analyte derivatization is not rare in HPLC, the amino acid derivatization procedure here might be considered time-consuming and complicated. To resolve this concern, it is

possible to use the pulsed-amperometric detection method where a multi-step electrical potential is input to the electrochemical sensor for non-derivatized amino acid detection [30].

## **4.6.2 Low Density Lipoprotein Separation**

### **4.6.2.1 Introduction**

Cardiovascular disease remains the leading cause of mortality in the United States (Table 4-1). It is well-known that atherosclerosis is the key mechanism that leads to various types of cardiovascular diseases, and currently analysis of low density lipoprotein (LDL) is one of the most widely used diagnostic tools to evaluate or predict atherosclerosis risk. While the levels of LDL and other lipoproteins are usually of limited predictive value due to many factors that can affect LDL concentrations in the arterial wall, the proportion of the LDL subfraction appears to have strong predictive value for the progression of atherosclerosis [31]. A large number of clinical studies support the hypothesis that the risk for atherosclerosis is associated with the proportion of different LDL subfractions in blood. Increased LDL<sup>-</sup> (oxidative modification of the native LDL) levels are found in subjects with coronary artery disease, particularly in diabetics and patients undergoing hemodialysis (HD). Therefore, it is important to have an easy way to analyze the proportion of LDL subfractions.

LDL particle populations are heterogeneous and can be separated on the basis of their different densities [31] or charges [33]. For example, ion-exchange chromatography can be used to separate LDL particles into at least two fractions [33]: the major fraction, native LDL (nLDL), which represents ~ 90–98% of plasma LDL; the second fraction, a

mildly oxidized LDL ( $\text{LDL}^-$ ), which usually represents up to 10% of plasma LDL. Figure 4-25 shows the schematic illustration of LDL particles which has sizes of around 22 nm. So far, only the conventional desktop HPLC system has been used to separate LDL subfraction. Our goal is to carry out LDL separation using microchip HPLC system with a hope that in the future LDL diagnosis can be done using portable devices with much lower costs of time and money. As follows we demonstrate the first work using microchip ion-exchange chromatography [34] and conductivity sensing for LDL subfraction separation.

Table 4-1: Cardiovascular disease in the United States [32].

Disease	Number of people effected in US
High Blood Pressure	50,000,000
Acute Heart Attack	7,700,000
Angina (chest pain)	6,300,000
Stroke	4,400,000
Rheumatic Heart Disease	1,800,000

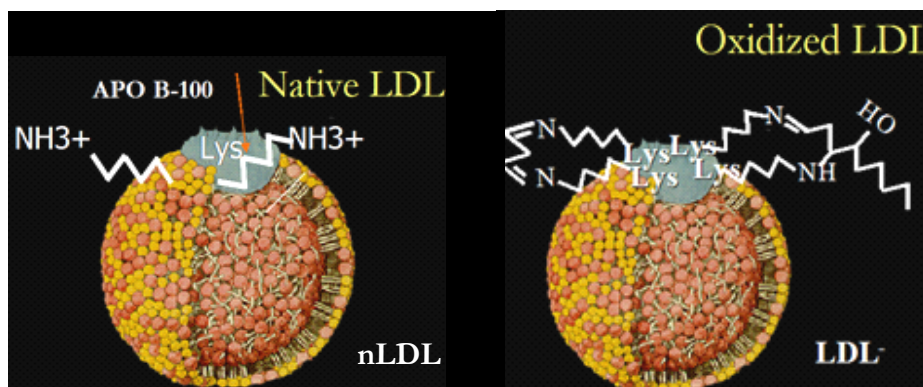


Figure 4-25: Schematic illustration of nLDL/ $\text{LDL}^-$  molecular structures.

#### 4.6.2.2 Sample Preparation

Purified LDL samples suspended in PBS solution were extracted from human blood plasma using a two-step centrifugation process at the Atherosclerosis Research Unit at the University of Southern California and were stored at 8 °C. LDL concentration in the sample was 200 µg/mL (85% native LDL, 15% oxidized LDL).

Two types of buffer solutions were prepared. Buffer A: aqueous solution containing 20 mM TRIS with a pH value of 7.2. Buffer B: aqueous solution containing 20 mM TRIS and 1M NaCl with a pH value of 7.2. Buffer solutions were used for salt gradient elution as well as isocratic elution of LDL samples.

#### 4.6.2.3 Conductivity Detection

Since native LDL and oxidized LDL are both charged molecules, it makes perfect sense to use conductivity detection for sensing of those molecules. In conductivity detection, the baseline conductance signal is generated by the eluent. When sample peak enters the detector, a change of conductance ( $\Delta G$ ) can be measured. For anion-exchange ion chromatography, the magnitude of this change is expressed in the following equation, assuming the samples and eluent are completely ionized [35]:

$$\Delta G = \frac{1}{10^{-3} K_{cell}} (\lambda_{S^-} - \lambda_{E^-}) C_S \quad (4.2)$$

where  $\lambda_{S^-}$  and  $\lambda_{E^-}$  are the equivalent conductance for the sample and eluent anions,  $C_S$  is the concentration of the sample anion, and  $K_{cell}$  is the conductivity sensor cell constant. The conductance change ratio on sample elution is usually very small, only a few percents of the background conductivity as shown in (4.3):

$$\frac{\Delta G}{G_{Background}} = \frac{(\lambda_{S^-} - \lambda_{E^-})C_S}{(\lambda_{E^+} + \lambda_{E^-})C_E} \approx \frac{C_S}{C_E} \approx 1\% \quad (4.3)$$

where  $C_E$  is the concentration of eluent anions. The sensitivity of conductivity detection is affected by the conductance noise level, sample injection volume, system dead volume, and the detector sensitivity. The conductance noise is mainly contributed from the temperature-fluctuation-induced background conductance change. In general, a 1 °C temperature change will result in a 2% conductance change [36]. Several approaches are available to increase the sensitivity for conductivity detection. First, suppressing the background conductance by using a suppressor column inserted after the separation column [37]. Second, increasing the sample plug concentration by using a sample preconcentration techniques [36]. Third, reducing sample injection volume and system dead volume. Fourth, reduce the sensor cell constant  $K_{cell}$ , which is especially achievable using MEMS technology [14]. The detection limit of conductivity detection can be found in 2.2.4.

The electrochemical sensor used for amino acid sensing in 4.6.1 was used here as a conductivity sensor for LDL. The difference is that AC signal instead of DC signal was input to the sensor for conductivity detection. Output current from the cell was sent to an op-amp circuit to convert the current signal into a voltage signal, which was recorded with the HP34970A data acquisition unit (RMS-DC mode). The sensor cell resistance during LDL separation was calculated and plotted against time to compose the chromatogram. Since LDL particles have a lower equivalent electrophoretic mobility than that of the anions in the eluent (chlorides), the conductivity of the sensor cell will drop when an LDL peak passes by. More details regarding the design principles and sensitivity of microchip conductivity sensor can be found in [35].

#### 4.6.2.4 Separation Results and Comments

High-pressure-capacity HPLC microchips introduced in 4.2.2 were used here for LDL separation. Because of the large size of LDL particles (~ 22 nm in diameter), superficial porous anion-exchange particles (Hamilton PRP-X500) were used to pack the separation column to avoid serious band-broadening effect caused by LDL trapping in the stationary phase. As a reference, LDL separation was first carried out using the conventional HPLC system with salt gradient elution and UV detection as shown in Figure 4-26. LDL subfractions were separated by anion exchange chromatography into nLDL (native LDL) and LDL<sup>-</sup>/LDL<sup>2-</sup> (oxidized LDL).

Figure 4-27 shows the LDL chromatogram obtained by microchip HPLC system with isocratic elution and on-chip conductivity sensing. Sample volume was defined by the sample injection valve with a 20  $\mu$ L sample loop (Rheodyne, Rohnert Park, CA). The preliminary data successfully demonstrates the separation and detection of 800 ng LDL (680 ng of native LDL and 120 ng of oxidized LDL). The limit of detection (LOD), calculated based on the signal-to-noise ratio in the chromatogram which is around 50, will be 80 ng assuming a signal-to-noise ratio of 5 is acceptable for analysis. The LOD of 80 ng corresponds to an original sample concentration LOD of 20  $\mu$ g/mL if the sample injection volume is still 20  $\mu$ L.

The relatively big band-broadening effect and long elution time observed in the microchip HPLC compared with the conventional HPLC were mainly caused by the large off-chip system dead/swept volume (~ 10  $\mu$ L), large sample injection volume, as well as the weak elution strength of the mobile phase used for the isocratic elution. Those factors, however, can be improved with more efforts on the chromatography method development.

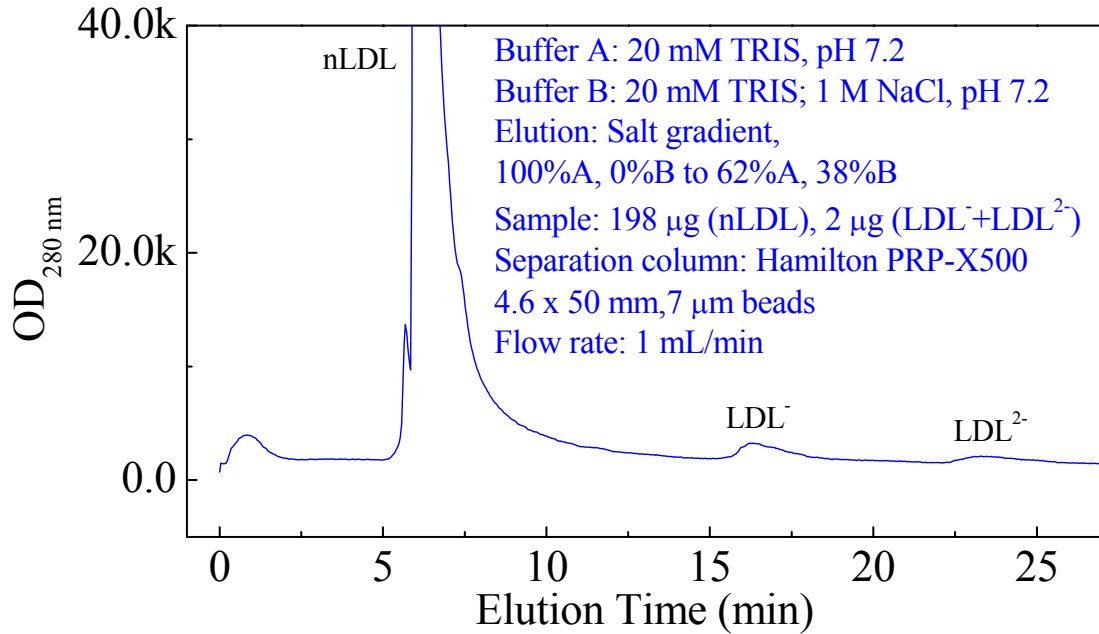


Figure 4-26: LDL separation obtained by conventional HPLC with salt gradient elution and UV detection.

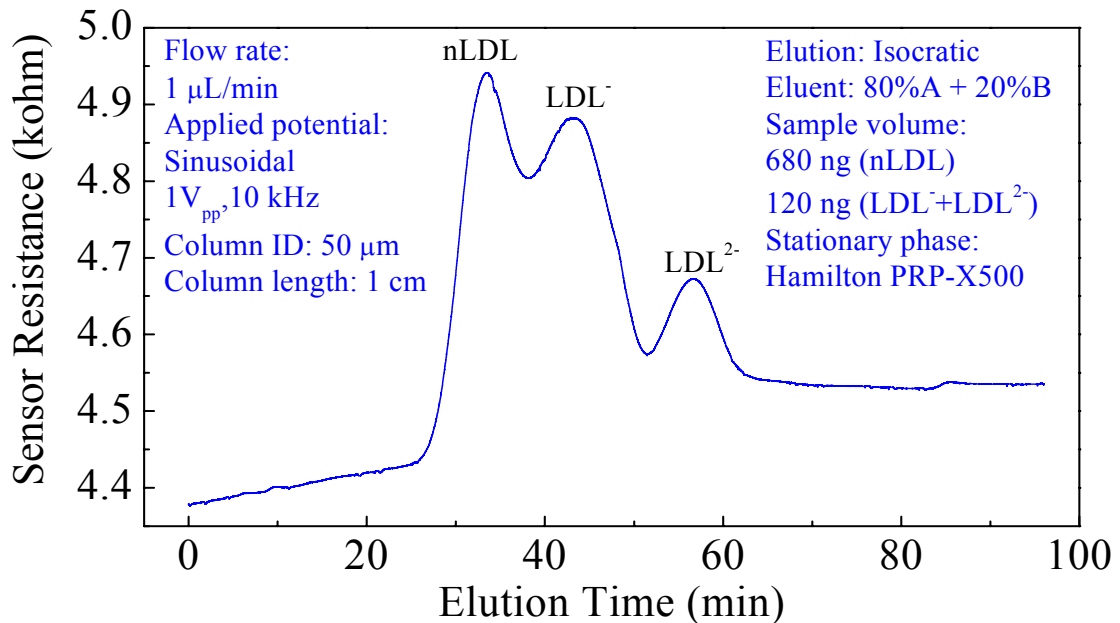


Figure 4-27: LDL separation obtained by microchip HPLC with isocratic elution at room temperature and conductivity detection.

## 4.7 Conclusions

Temperature is an important parameter in liquid chromatography that can be used to improve chromatographic performance or to replace complicated analyte elution mechanisms such as solvent gradient elution. It is therefore quite an attractive idea to add the temperature-control functionality to the microchip HPLC system since temperature-control in the micro scale is much more efficient than it is in the macro scale. In this chapter, we introduced the first microchip TGIC systems with a particle-packed separation column (based on the anchored-type parylene channel technology), an electrochemical analyte sensor, a resistive heater for column temperature control, and a thermal isolation structure for power consumption reduction. System performance, including pressure capacity, power consumption, and solvent temperature controllability were evaluated. Using the developed systems, we have successfully demonstrated the first microchip TGIC of amino acids. Separation of LDL subfraction for atherosclerosis diagnosis was as well demonstrated.

## 4.8 Bibliography

- [1] J. Xie, Y. N. Miao, J. Shih, Y. C. Tai, and T. D. Lee, "Microfluidic platform for liquid chromatography-tandem mass spectrometry analyses of complex peptide mixtures," *Analytical Chemistry*, vol. 77, pp. 6947-6953, 2005.
- [2] J. Xie, J. Shih, Q. He, C. Pang, Y. C. Tai, Y. N. Miao, and T. D. Lee, "An integrated LC-ESI chip with electrochemical-based gradient generation," presented at the 17th IEEE International Conference on Micro Electro Mechanical Systems (MEMS 2004), Maastricht, The Netherlands, 2004.
- [3] T. Greibrokk, "Heating or cooling LC columns," *Analytical Chemistry*, vol. 74, pp. 374A-378A, 2002.
- [4] T. Greibrokk and T. Andersen, "Temperature programming in liquid chromatography," *Journal of Separation Science*, vol. 24, pp. 899-909, 2001.
- [5] T. Greibrokk and T. Andersen, "High-temperature liquid chromatography," *Journal of Chromatography A*, vol. 1000, pp. 743-755, 2003.
- [6] G. Hesse and H. Engelhar, "Temperaturprogrammierung Bei Der Adsorptionschromatographie Von Losungen," *Journal of Chromatography*, vol. 21, pp. 228-&, 1966.
- [7] Y. Hirata and E. Sumiya, "Temperature-Programmed Reversed-Phase Liquid-Chromatography with Packed Fused-Silica Columns," *Journal of Chromatography*, vol. 267, pp. 125-131, 1983.

- [8] K. Jinno, J. B. Phillips, and D. P. Carney, "Temperature-Controlled High-Speed Microcolumn Liquid-Chromatography," *Analytical Chemistry*, vol. 57, pp. 574-576, 1985.
- [9] H. H. Strain, "Conditions Affecting the Sequence of Organic Compounds in Twsett Adsorption Columns," *Industrial and Engineering Chemistry-Analytical Edition*, vol. 18, pp. 605-609, 1946.
- [10] R. Trones, A. Iveland, and T. Greibrokk, "High-Temperature Liquid-Chromatography on Packed Capillary Columns with Nonaqueous Mobile Phases," *Journal of Microcolumn Separations*, vol. 7, pp. 505-512, 1995.
- [11] C. Y. Shih, Y. Chen, J. Xie, Q. He, and Y. C. Tai, "On-chip temperature gradient liquid chromatography," presented at the 18th IEEE International Conference on Micro Electro Mechanical Systems (MEMS 2005), Miami, USA, 2005.
- [12] L. J. Kricka and P. Wilding, "Microchip PCR," *Analytical and Bioanalytical Chemistry*, vol. 377, pp. 820-825, 2003.
- [13] K. Sun, A. Yamaguchi, Y. Ishida, S. Matsuo, and H. Misawa, "A heater-integrated transparent microchannel chip for continuous-flow PCR," *Sensors and Actuators B-Chemical*, vol. 84, pp. 283-289, 2002.
- [14] Q. He, C. Pang, Y. C. Tai, and T. D. Lee, "Ion liquid chromatography on-a-chip with beads-packed parylene column," presented at the 17th IEEE International Conference on Micro Electro Mechanical Systems (MEMS 2004), Maastricht, The Netherlands, 2004.

- [15] M. Liger, D. C. Rodger, and Y. C. Tai, "Robust parylene-to-silicon mechanical anchoring," presented at the 16th IEEE International Conference on Micro Electro Mechanical Systems (MEMS2003), Kyoto, Japan, 2003.
- [16] E. Meng and Y. C. Tai, "A Parylene MEMS Flow Sensing Array," presented at Proceedings of the 12th International Conference on Solid-State Sensors, Actuators and Microsystems, Boston, USA, 2003.
- [17] C. Y. Shih, Y. Chen, and Y. C. Tai, "Parylene-strengthened thermal isolation technology for microfluidic system-on-chip applications," presented at the 13th International Conference on Solid-State Sensors, Actuators and Microsystems, Seoul, Korea, 2005.
- [18] C. Y. Shih, T. A. Harder, and Y. C. Tai, "Yield strength of thin-film parylene-C," *Microsystem Technologies-Micro-and Nanosystems-Information Storage and Processing Systems*, vol. 10, pp. 407-411, 2004.
- [19] F. Houdiere, P. W. J. Fowler, and N. M. Djordjevic, "Combination of column temperature gradient and mobile phase flow gradient in microcolumn and capillary column high-performance liquid chromatography," *Analytical Chemistry*, vol. 69, pp. 2589-2593, 1997.
- [20] R. G. Wolcott, J. W. Dolan, L. R. Snyder, S. R. Bakalyar, M. A. Arnold, and J. A. Nichols, "Control of column temperature in reversed-phase liquid chromatography," *Journal of Chromatography A*, vol. 869, pp. 211-230, 2000.
- [21] M. U. Kopp, A. J. de Mello, and A. Manz, "Chemical amplification: Continuous-flow PCR on a chip," *Science*, vol. 280, pp. 1046-1048, 1998.

- [22] Z. Zhang, P. Boccazzi, H. Choi, N. Szita, A. J. Sinskey, and K. F. Jensen, "A microchemostat–continuous cell culture in microbioreactors," presented at the 8th International Conference on Miniaturized Systems in Chemistry and Life Sciences, Malmo, Sweden, 2004.
- [23] J. A. Ruffner, P. G. Clem, B. A. Tuttle, C. J. Brinker, C. S. Sriram, and J. A. Bullington, "Uncooled thin film infrared imaging device with aerogel thermal isolation: deposition and planarization techniques," *Thin Solid Films*, vol. 332, pp. 356-361, 1998.
- [24] B. W. Vanoudheusden and A. W. Vanherwaarden, "High-Sensitivity 2-D Flow Sensor with an Etched Thermal Isolation Structure," *Sensors and Actuators A-Physical*, vol. 22, pp. 425-430, 1990.
- [25] R. Kersjes and W. Mokwa, "A Fast Liquid Flow Sensor with Thermal Isolation by Oxide-Filled Trenches," *Sensors and Actuators A-Physical*, vol. 47, pp. 373-379, 1995.
- [26] T. Y. Chang, W. Lee, H. C. Lee, D. H. Cho, and S. Park, "Polymer characterization by non-size exclusion chromatography: Temperature gradient interaction chromatography," *American Laboratory*, vol. 34, pp. 39-+, 2002.
- [27] C. Cooper, N. Packer, and K. Williams, *Amino acid analysis protocols*, vol. 159. Totowa, New Jersey: Humana Press, 2001.
- [28] B. W. Boyd, S. R. Witowski, and R. T. Kennedy, "Trace-level amino acid analysis by capillary liquid chromatography and application to in vivo microdialysis sampling with 10-s temporal resolution," *Analytical Chemistry*, vol. 72, pp. 865-871, 2000.

- [29] J. Wang, M. P. Chatrathi, and B. Tian, "Micromachined separation chips with a precolumn reactor and end-column electrochemical detector," *Analytical chemistry*, vol. 72, pp. 5774-5778, 2000.
- [30] C. D. Garcia and C. S. Henry, "Direct determination of carbohydrates, amino acids, and antibiotics by microchip electrophoresis with pulsed amperometric detection," *Analytical chemistry*, vol. 75, pp. 4778-4783, 2003.
- [31] M. A. Austin, J. L. Breslow, C. H. Hennekens, J. E. Buring, W. C. Willett, and R. M. Krauss, "Low-Density Lipoprotein Subclass Patterns and Risk of Myocardial-Infarction," *Jama-Journal of the American Medical Association*, vol. 260, pp. 1917-1921, 1988.
- [32] <http://www.healthauthority.com>
- [33] G. Cazzolato, P. Avogaro, and G. Bittolobon, "Characterization of a More Electronegatively Charged Ldl Subfraction by Ion-Exchange Hplc," *Free Radical Biology and Medicine*, vol. 11, pp. 247-253, 1991.
- [34] C. Y. Shih, Q. He, Y. C. Tai, C. Lin, T. Hsiai, and J. Hwang, "MEMS HPLC system for on-chip subfraction detection," presented at the 29th International Symposium on High Performance Liquid Phase Separations and Related Techniques, Stockholm, Sweden, 2005.
- [35] Q. He, "Integrated nano liquid chromatography system on-a-chip," in *Electrical Engineering*. Pasadena: California Institute of Technology, 2005.
- [36] J. S. Fritz and D. T. Gjerde, *Ion chromatography*, 3rd ed. New York: Wiley-VCH, 2000.

- [37] F. Laugere, M. J. Vellekoop, T. Bastemeijer, P. M. Sarro, G. Van der Steen, and A. Bossche, "Electronic baseline-suppression for liquid conductivity detection in a capillary electrophoresis microchip," presented at the 1st IEEE International Conference on Sensors (IEEE Sensors 2002), Orlando, United States, 2002.

---

# CHAPTER 5

---

## EMBEDDED HPLC SYSTEM

### 5.1 Introduction

As has been mentioned previously in chapter 3, the embedded-type parylene microfluidic channel has very high pressure capacity (higher than 1000 psi). Since column robustness is crucial for any HPLC system, it is intuitive to build a microchip HPLC system, which contains separation column, stationary-phase particle filter, analyte sensors, basing on the embedded-type parylene channel technology. The prospect is to have a microchip HPLC system that can withstand pressure up to 10,000 psi. With that pressure capacity, a long chip-based separation column (longer than 10 cm) can be made and challenging separations that require large number of theoretical plates (> 1 million plates) can be done with microchip HPLC system. Besides, since photoresist sacrificial

layer is not necessary for embedded-channel technology, device fabrication throughput as well as column reliability can be dramatically improved.

In this chapter we will demonstrate the design and fabrication of novel embedded microchip HPLC systems. Different in fabrication complexity and device functionality, two versions of embedded systems are proposed, the single-mask system and multiple-mask system. Various sensing methods, including LIF detection and capacitively-coupled contactless conductivity detection ( $C^4D$ ) have been studied to be used with the proposed embedded systems. A complete LABVIEW program was developed to execute fully automatic chromatography tasks with on-chip temperature control. System characterization and successful separation examples will be presented as well.

## **5.2 Single-Mask Embedded HPLC System**

### **5.2.1 Design and Fabrication**

The design motivation of the single-mask embedded HPLC system is to have a high-throughput and low-cost fabrication process that produces robust microchip HPLC columns good for replacing conventional capillary HPLC columns [1].

The fabrication process starts with growing 0.5  $\mu\text{m}$  oxide on both sides of a silicon wafer. Front side oxide is patterned with buffered HF to define liquid inlet/outlet, particle filter, separation column and LIF detection cell patterns.  $\text{XeF}_2$  is then used to etch down and undercut silicon through oxide openings to create channel cross-section. A 15  $\mu\text{m}$  parylene layer is then conformally deposited on wafer front side to form fluidic channel wall and seal the oxide openings. Due to the predetermined oxide opening size differences, column/filter sections are sealed from the top by parylene deposition but

liquid inlet/outlet remains open as shown in Figure 5-1. Particle-filter structure is formed by two mechanisms. First, due to mass transport limitation of  $\text{XeF}_2$ , silicon etching rate is a function of oxide opening size (Figure 5-2). Therefore, smaller oxide opening around the filter section, compared with column section, results in a smaller  $\text{XeF}_2$ -etched channel cross-section. Second, after oxide opening around the filter section is sealed by parylene deposition, filter cross-section continues to shrink due to the parylene coating to its inner surface through the neighboring oxide opening in the column section. Figure 5-3 shows that, with the particle-filter structure introduced above, 5  $\mu\text{m}$  fluorescent particles were successfully packed into the separation column via the conventional slurry-packing technique.

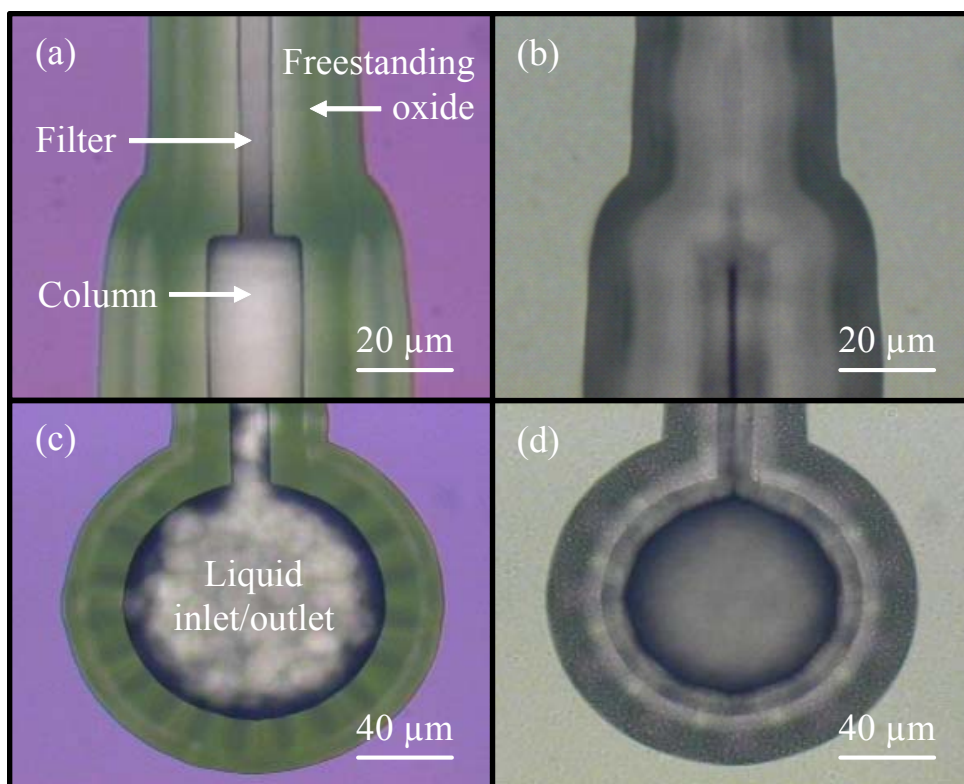


Figure 5-1: Top view of the 15  $\mu\text{m}$  parylene coating process. (a, b) Filter/column section, (c, d) liquid inlet/outlet before and after parylene coating.

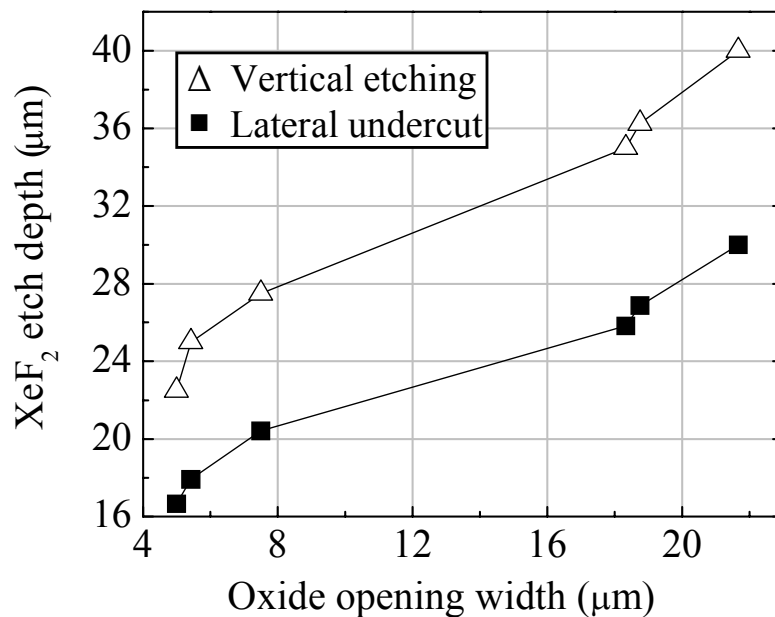


Figure 5-2: XeF<sub>2</sub> etching size-effect study. 18 loops of XeF<sub>2</sub> etching were used on a single silicon wafer (~5% of wafer area was exposed for silicon etching).

Due to the single-mask process criterion, no sophisticated on-chip sensor can be fabricated on this microchip HPLC system as shown in Figure 5-4. However, LIF detection can be applied using off-chip optics (will be discussed more in 5.4). Here, the on-chip LIF detection cell is composed of a closely meandering fluidic channel matrix for convenient laser spot alignment (Figure 5-4(c)) [1].

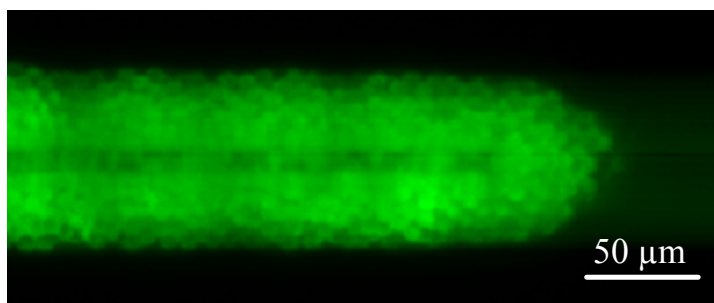


Figure 5-3: 5 μm fluorescent particles packed into an embedded parylene column by slurry-packing.

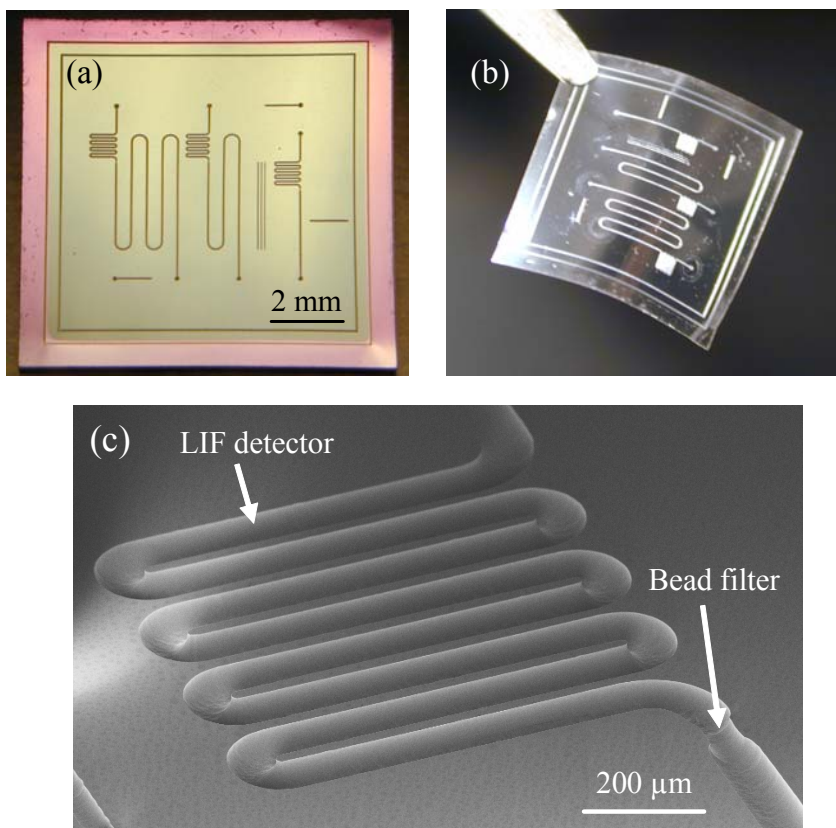


Figure 5-4: (a) Fabricated single-mask HPLC chip, (b) thin-film (skin) HPLC device by peeling parylene membrane from (a), (c) SEM picture of LIF detector channel profile. Parylene/oxide layer was peeled off.

### 5.2.2 System Characterization

The pressure capacity of the fabricated device was studied. Testing results showed that the embedded parylene channel withstood at least 1,000 psi without fracture (Figure 5-5), which is crucial for on-chip chromatography application and has not been achieved by non-embedded MEMS HPLC technology [2]. Stress distribution in the parylene column wall under inner pressure loading was analyzed by a FEMLAB simulation that shows the embedded-channel boundary condition reduces the maximum stress by 34% compared with a freestanding channel boundary condition (Figure 5-6).

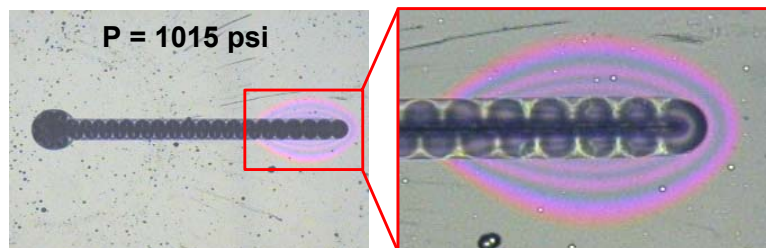


Figure 5-5: Embedded parylene channel loaded with 1,015 psi inner pressure without fracture. The Newton rings appeared due to the local parylene-peeling from the silicon substrate (likely caused by channel surface buckling), which did not affect column integrity.

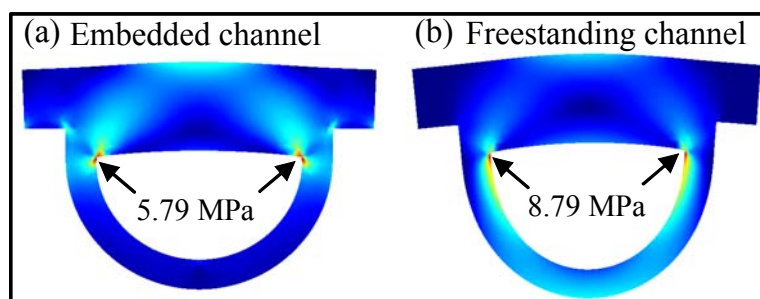


Figure 5-6: Parylene column stress analysis under 100 psi inner pressure loading. Values are maximum stresses. (a) Embedded boundary condition where channel bottom is secured by the silicon substrate, (b) freestanding boundary condition.

The single-mask design as mentioned above, although fairly simple to fabricate, does have its own limitation on HPLC functionality. For example, no on-chip sensor such as an electrochemical sensor is available. Liquid access holes and separation column are on the same side of the wafer, which makes integration of off-chip optics for LIF detection difficult. Also, the channel cross-section is not quite symmetric and has “dead corners” as discussed in 3.3.2, which may enhance the band-broadening in separation. Finally, it is hard for this process to have well-defined particle-filter structure

since many factors such as mass transportation efficiency in silicon etching or parylene coating process need to be carefully controlled.

### **5.3 Multiple-Mask Embedded HPLC System**

#### **5.3.1 Design and Fabrication**

The design motivation of the multiple-mask embedded HPLC system is to remove the drawbacks encountered in the single-mask system mentioned above at the expense of using a more complicated fabrication process [3].

Figure 5-7 shows the simplified fabrication process flow of the multiple-mask embedded HPLC system (heater and sensor are not displayed). Fabrication starts by growing 1- $\mu\text{m}$ -thick thermal oxide on 4-inch silicon wafers. 200 nm-Au/30 nm-Cr is deposited on wafer front side using thermal evaporation. Au and Cr are then patterned to form resistive heater and interdigitated conductivity sensor using wet etching. Backside oxide is patterned using BHF to define liquid access holes. DRIE is then used to etch silicon from wafer backside until a 50- $\mu\text{m}$ -thick silicon membrane is left on the wafer front side. DRIE is used to create 6- $\mu\text{m}$ -wide, 80- $\mu\text{m}$ -deep trenches to define fluidic channel boundaries as shown in Figure 5-7 (a). First parylene layer (5  $\mu\text{m}$ ) is deposited on the wafer front side and fills up DRIE trenches. Parylene is then etched back using oxygen plasma until silicon surface reveals on wafer front side. After treating the silicon surface with A174 parylene adhesion promoter, a second parylene layer (2  $\mu\text{m}$ ) is deposited and patterned to create openings for  $\text{XeF}_2$  silicon etching. This thin parylene layer (2  $\mu\text{m}$ ) is used instead of the first thick parylene layer (5  $\mu\text{m}$ ) for the reason that it is much easier to have precise patterning on thin parylene layer.  $\text{XeF}_2$  is then used to etch

front side silicon and create square-like channel cross-section (Figure 5-7 (e)). At the same time, liquid access holes are opened by this etching process. Third parylene layer (7  $\mu\text{m}$ ) is then deposited to seal the second parylene layer openings and complete the embedded parylene channel as well as the particle filter structures. During this final parylene coating process, wafer backside is covered by a backing wafer with a spacing ring in between so that parylene will not come in from wafer backside holes and parylene from the front side openings will not seal the back side holes. Parylene is then patterned to reveal electrical contact pads. Wafers are then diced into 1.1 cm x 1.1 cm chips.

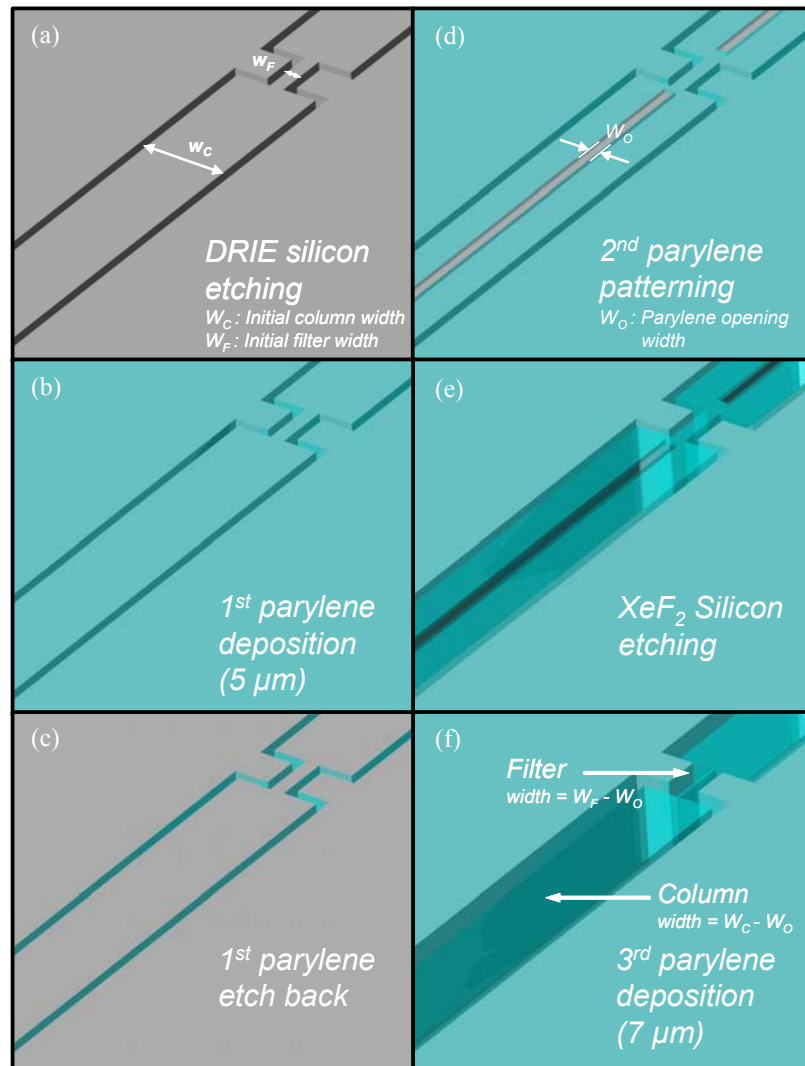


Figure 5-7: Fabrication process flow for the multiple-mask embedded HPLC system.

As shown in Figure 5-7, particle filters for stationary-phase packing are fabricated. The filter size is determined as follows. First, a smaller channel width  $W_F$  ( $W_F = 12 \mu\text{m}$ ,  $W_C = 60 \mu\text{m}$ ) around the filter position is defined by the front side DRIE trench, which is latter filled with the first parylene layer. The filter width is further reduced by the third parylene layer coating through the second parylene layer openings (opening width  $W_O$ ) to a final size ( $W_F - W_O$ ), which is only a couple of microns. Figure 5-8 then shows the actual device pictures. This technology produces repeatable filter sizes for packing stationary-phase particles with a diameter of  $3 \mu\text{m}$  or larger as shown in Figure 5-9.

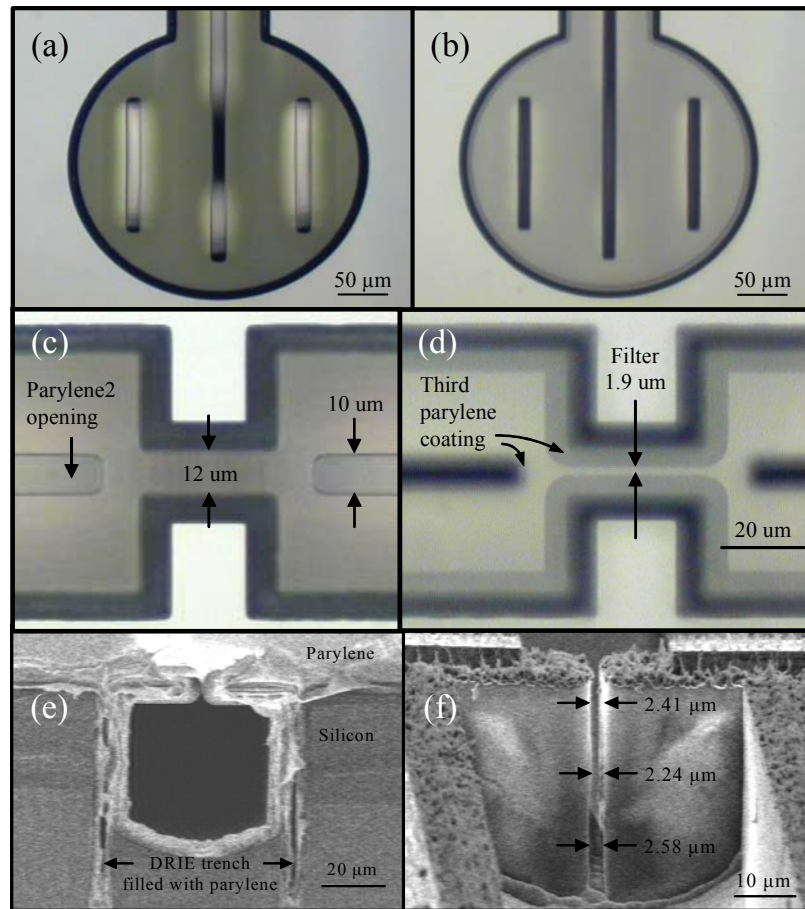


Figure 5-8: (a, b) Top view of liquid access hole before and after the third parylene coating, (c, d) top view of the particle filter before and after the third parylene coating, (e) column cross-section, (f) filter cross-section after etching away top parylene layer.

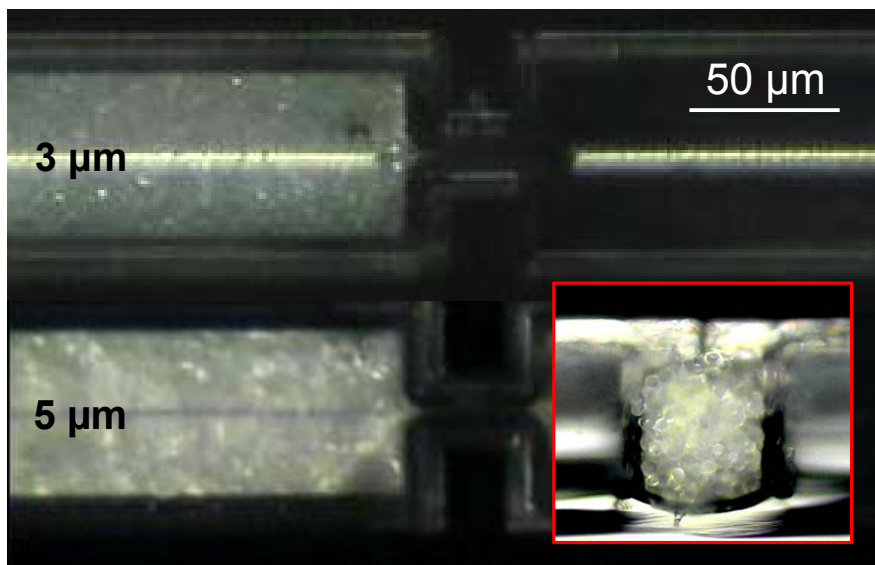


Figure 5-9: Embedded parylene column packed with 3  $\mu\text{m}$  (top) and 5  $\mu\text{m}$  (bottom) porous C18 silica particles using slurry-packing technique. The inset shows the cross-section of the column packed with 5  $\mu\text{m}$  particles.

Furthermore, in order to pack the state-of-the-art submicron-sized particles into the separation column [4], we have developed a reliable submicron-filter-formation mechanism as described in Figure 5-10. A dummy filter structure which has a larger second parylene layer opening is put across the channel to the working filter as shown in the step 1. After the micron-sized working filter is formed as shown in the step 2, the working filter size is continuously reduced by diffusive-parylene-coating through the dummy filter parylene opening to the submicron range when dummy filter is finally sealed by the third parylene coating. Figure 5-10(b) confirms that the proposed mechanism reliably generates a submicron-sized filter. It is a pity that currently no submicron-sized stationary phase particles are commercially available, and therefore no packing results of this filter is demonstrated here.

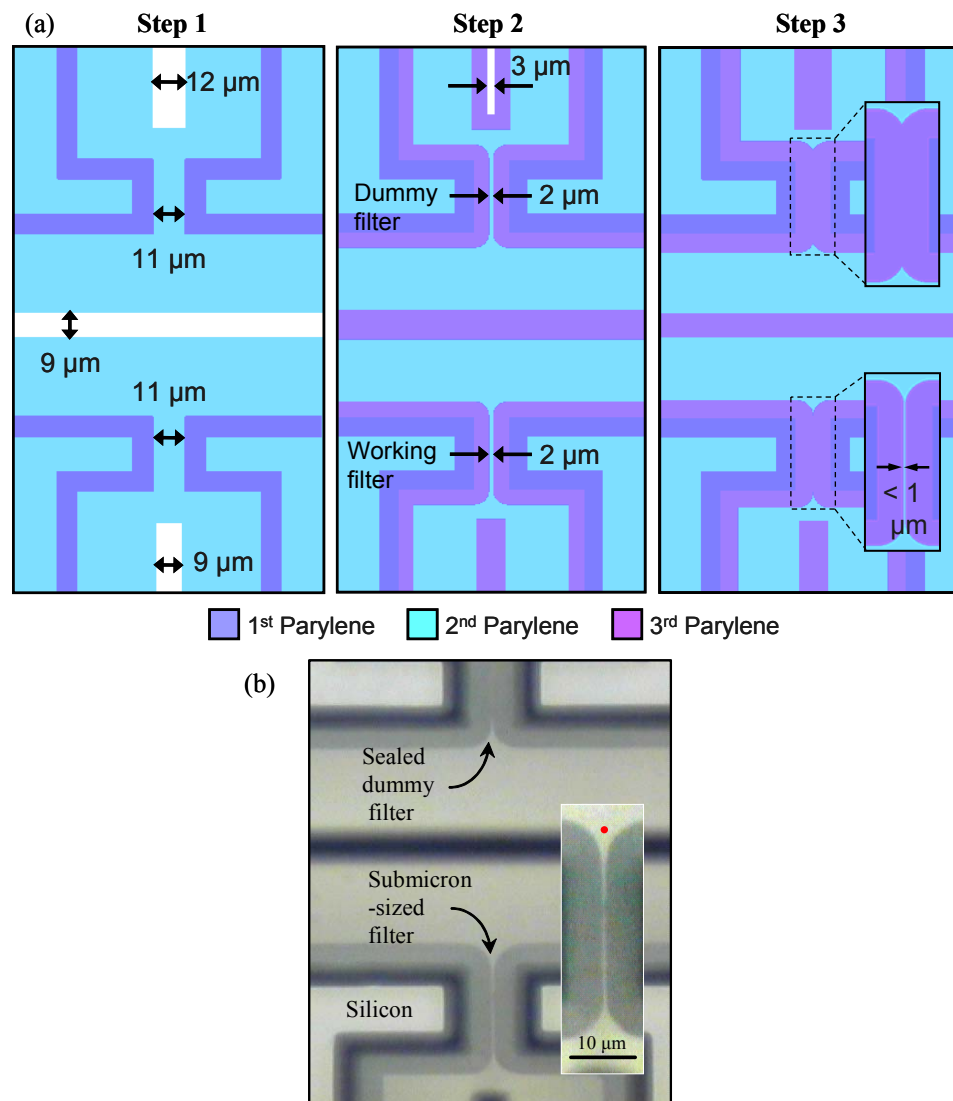


Figure 5-10: (a) Formation mechanism for submicron-sized particle filter. (b) Actual picture of the submicron-sized particle filter; the red spot symbolizes a 1- $\mu\text{m}$ -sized particle.

### 5.3.2 System Characterization

Figure 5-11(a) shows the fabricated multiple-mask embedded HPLC microchip. Chip surface topography was examined using the Tencor P15 surface profiler as shown in Figure 5-11(b). Results show that the height variation across the 1.1 cm x 1.1 cm chip

area is only a couple of microns. The pressure capacity of the embedded-type parylene channel has been tested to be higher than 1,000 psi without fracture. Moreover, due to the highly planarized chip topography, a direct-top-clamping procedure using a glass plate can be easily applied to enhance channel pressure capacity to thousands of psi as shown in Figure 5-11(c).

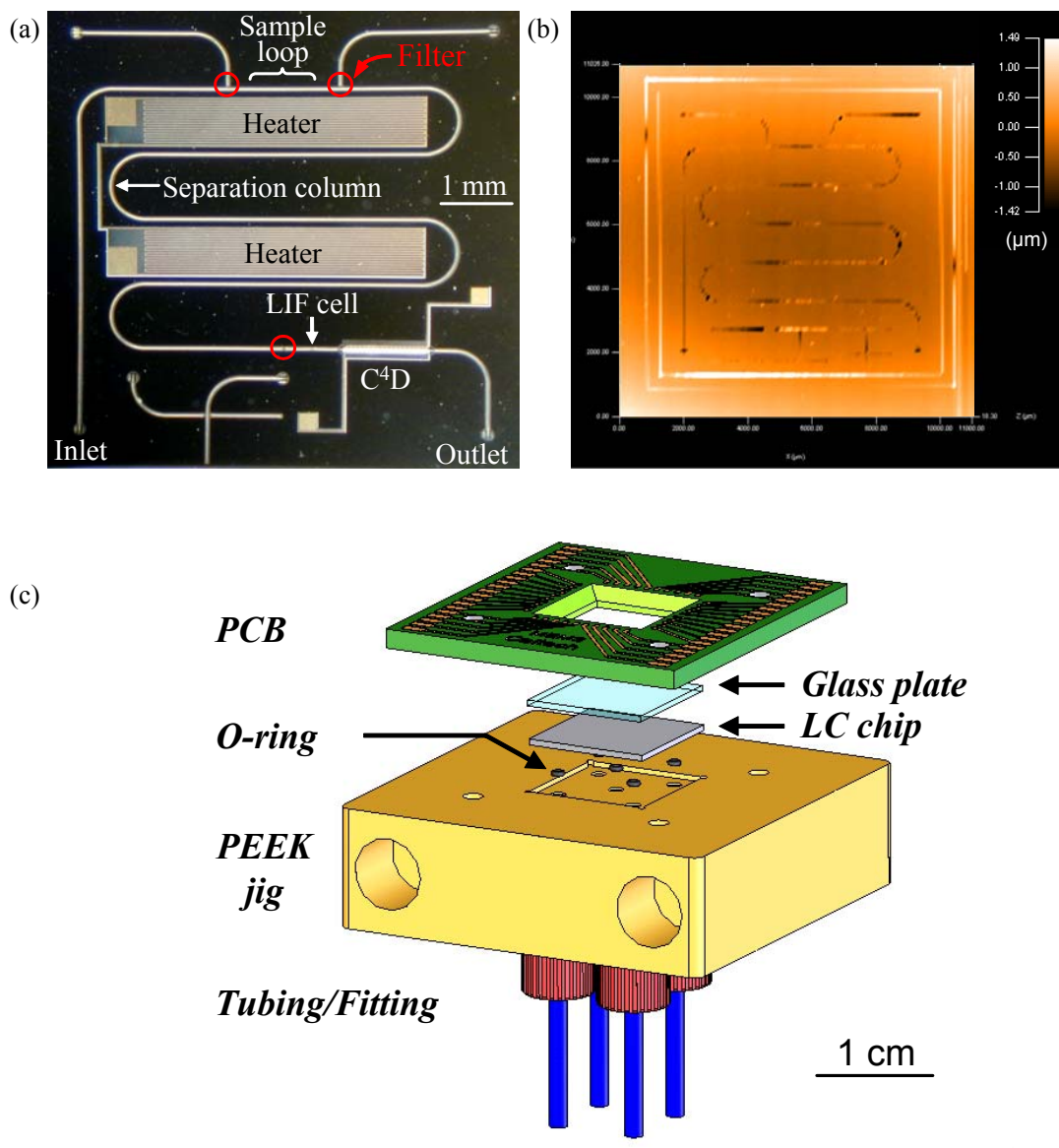


Figure 5-11: (a) Fabricated multiple-mask embedded HPLC microchip, (b) surface profile scan obtained using Tencor P15 surface profiler, (c) chip packaging.

Table 5-1 then shows the leak rate testing results of the proposed packaging method. Water was used as the filling solvent in the test. Solvent was injected through the mobile phase inlet with a nitrogen gas pressure source. The other three liquid access holes were sealed with PEEK nuts through the jig. The leak rate under certain pressure was obtained by measuring the liquid front moving velocity in a Teflon tube connected to the column inlet. With the glass-plate-clamping technique, the leak rate was measured to be 7 nL/min at 200 psi and 37.2 nL/min at 500 psi. Observing from the experiment, the leak rate was likely dominated by leakage through parylene pinholes since liquid was found between the chip and the glass plate but no holes (micron-sized) on parylene channel top surfaces were observed. For maximum pressure capacity, an epoxy thin layer can be applied between the HPLC chip and the glass plate, which completely removes the air gap in between. The leak rate of such packaging structure was only 2.1 nL/min at 500 psi and 20.3 nL/min at 1000 psi. In this case, the leak rate is dominated by the leakage through O-ring/chip and tubing/jig interfaces.

Table 5-1: System leak rate testing. Water was used as the filling solvent.

Pressure loading (psi)	Leak rate (nL/min)	
	Glass plate	Glass plate / epoxy
200	7.0	< 1
500	37.2	2.1
1000	> 100	20.3

Furthermore, the flow rate vs. pressure curve of the packed embedded column was measured as shown in Figure 5-12. The flow rate-pressure relationship is described by (see chapter 2 for parameters explanation):

$$F = \frac{\varepsilon d_p^2 A_c}{\Phi \eta L_c} \Delta P \quad (5.1)$$

By measuring the flow rate vs. pressure curve, column permeability or dimensionless flow resistance can be obtained, which is an important parameter for evaluating column-packing quality. The curve also provides information regarding the column backpressure under specific mobile phase flow rate used in the chromatography experiments (assume same fluidic viscosity in both experiments). In the testing, DI water was sent through the column with an adjustable nitrogen gas pressure source. The flow rate under certain pressure was obtained by measuring the liquid front moving velocity in a Teflon tube connected to the column inlet. In Figure 5-12, the linear curve-fitting was done to data points between 50 and 160 psi. The low pressure (<50 psi) data point was avoided since a nonlinear flow rate-pressure relationship often appears in the low pressure regime. According to the linear fitting result and equation (5.1), we then obtained:

$$\frac{\Phi}{\varepsilon} = 578 \quad (5.2)$$

Assuming the flow impedance  $\Phi$  is 500, which is common for spherical porous particles, the corresponding porosity  $\varepsilon$  is 0.865, which is slightly higher than conventional LC column porosity (0.80 to 0.84). The reason for the higher porosity is due to the fact that the microchip column dimension is approaching the order of magnitude of particle size and particle packing density is in general lower around the column wall, therefore the column packing becomes effectively “less dense” than conventional columns which has much larger column diameters. Compared with the anchored-type parylene column which has a rectangular column cross-section, the embedded-type parylene column which

has a square-like column cross-section does have lower porosity which means particle packing is denser in the embedded column under the same particle packing pressure.

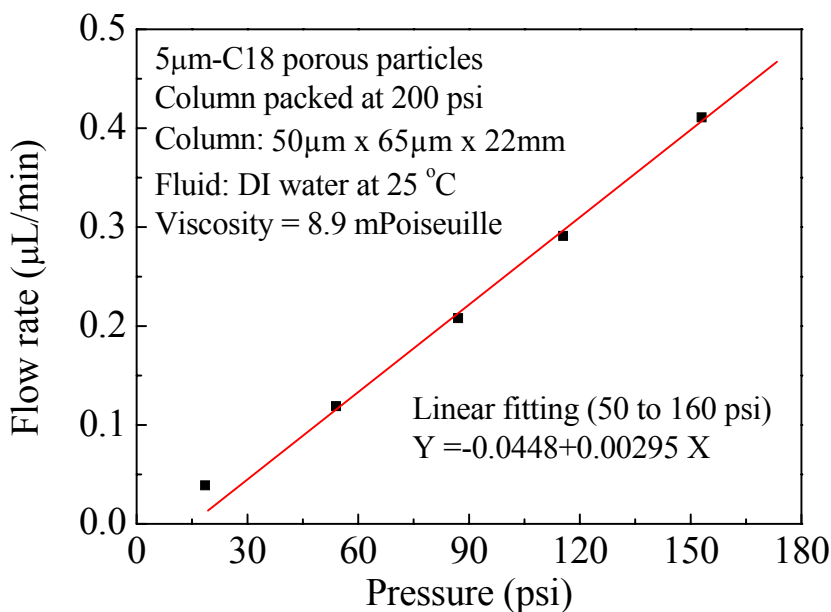


Figure 5-12: Flow rate vs. pressure curve of the embedded LC column. Linear fitting was done to the higher pressure (> 50 psi) data points.

## 5.4 Laser-Induced Fluorescence Detection

### 5.4.1 Introduction

Fluorescence detection is based on the property of certain analyte molecules to emit photons after being excited by photons with shorter wavelengths. Fluorescent molecules are promoted to an excited state by absorption of a photon. After typically 1-100 ns, molecules fall back to one of the vibrational energy levels of the ground state and emit a photon. Molecules that fluoresce or for which fluorescing derivatives can be obtained are picked up with high sensitivity by fluorescence detection. The sensitivity may be up to 1,000 times greater than with UV detection [5].

The excitation light sources for fluorescence detection are versatile, from mercury vapor to xenon to quartz halogen to deuterium to lasers. Using a laser as the excitation source for fluorescence detection is called Laser-Induced Fluorescence (LIF) detection. Lasers have well-defined wavelengths and can be focused on a very small area, yielding effective cell volumes as small as 1 nl [5]. Therefore, LIF has extremely high sensitivity and it can be easily incorporated to microchip HPLC system using off-chip optics [6-8].

The transparency characteristics of parylene to visible light make LIF a favorable detection method for our microchip HPLC system. Besides, due to the embedded-type channel configuration, incident laser light will scatter vigorously inside the channel from the roughened silicon surface (roughened by DRIE etching) and results in a thorough excitation inside the detection cell, which in turn produces stronger fluorescence signal. While it is true that a stronger reflective laser signal will be generated due to this scattering phenomenon, the laser signal level will be filtered by a bandpass filter to a negligible level and therefore the overall SNR (signal-to-noise ratio) will be enhanced by using this embedded-type channel. This advantage is not available when an anchored-type channel is used. Finally, the scattering phenomenon also provides information regarding laser spot alignment to the embedded LIF cell. When best alignment is achieved, scattering is strongest and so will be the signal picked up by the photodiode (bandpass filter is removed from the optical path during the alignment).

#### **5.4.2 System Design and Fabrication**

Figure 5-13 shows the schematic plot and the real setup of our homemade LIF system. All optics and optical paths are lying on the XY plane instead of stacking up in

the Z direction so as to facilitate the optics alignment procedure as well as the integration of microchip HPLC components. The excitation light source is a 488 nm argon ion laser with adjustable output power (National Laser Company, Salt Lake city, Utah). The emitted laser passes through a homemade, 200- $\mu\text{m}$ -sized pinhole chip followed by a stepped power density filter. The laser beam is then reflected by a visible-laser quality mirror followed by a laser-line bandpass filter (bandwidth equal to 1.9 nm with a central wavelength of 488 nm). The laser beam is then focused using a simple lens (diameter = 40 mm, effective focal length = 100 mm) onto the LIF cell of the microchip with an incident angle of 60 degrees. The reflected laser beam is absorbed by a laser beam stopper. A microscope objective (50X, NA = 0.45) is used to collect the fluorescence emitted from the LIF cell. Light collected by the objective then passes through a longpass filter (transition width < 4.9 nm, edge steepness = 2.5 nm) to remove the 488 nm laser light source. Fluorescence signal is then collected by the photodiode (DET110, Thorlabs, North Newton, NJ) and a current signal is accordingly generated. The current signal is converted to a voltage signal using a simple Op-Amp circuit. The voltage signal is then picked up by the data acquisition unit (HP34970A) and is sent to a PC where the chromatogram is recorded. Most system components, including the laser, pinhole, mirror, lens, microchip/jig, objective, and photodiode are fixed on top of XYZ stages to allow maximum alignment flexibility. The microchip/jig piece is fixed to the XYZ stage with screws to avoid movements caused by the pulling of fluidic tubing from jig backside.

In order to align the laser spot onto the LIF cell of the microchip, a CCD camera, a foldable mirror, and a monitor were assembled next to the objective to catch the chip surface image around the LIF cell. After the laser spot alignment is done, the mirror is

folded down to switch the optical path back to the longpass filter. Figure 5-14 shows an example of a successfully aligned laser spot on the LIF cell.

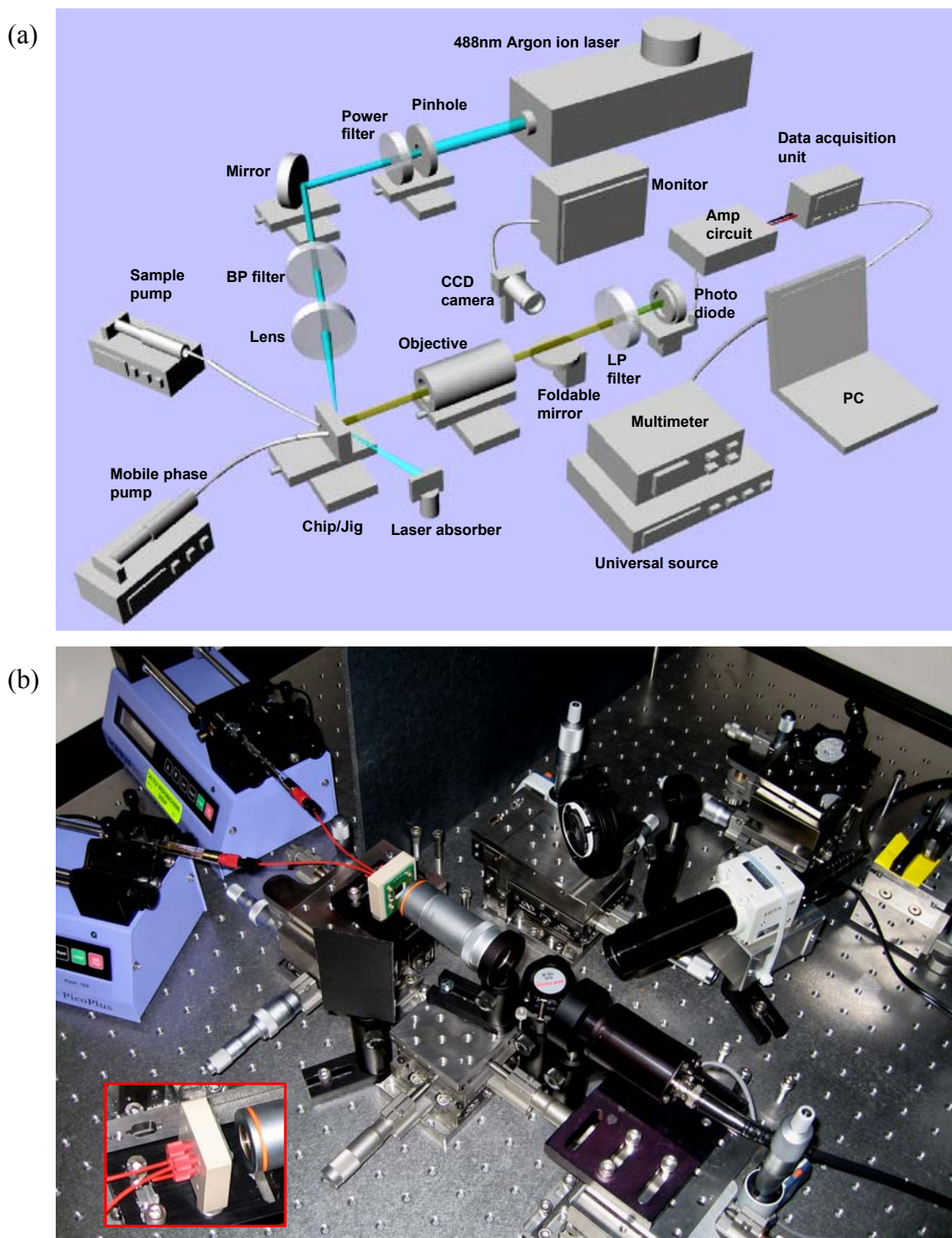


Figure 5-13: (a) Schematic plot of the LIF system, (b) pictures of the actual system.

Light-absorbing black boards were used to isolate optical paths from each other to reduce noise from laser light scattering. The whole LIF detection system was built on top of an anti-vibration table and was shielded from ambient light and dust using black rubberized fabric.

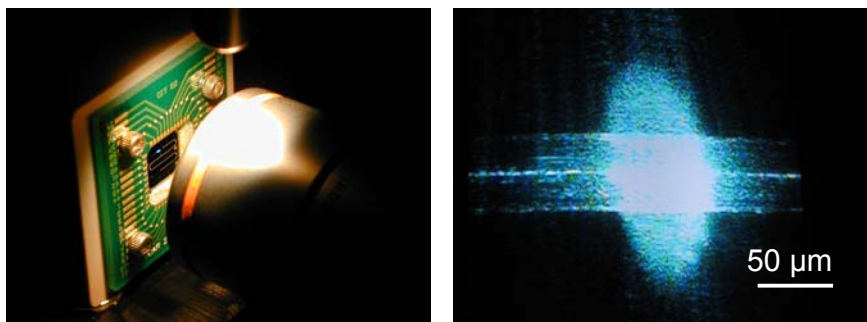


Figure 5-14: Laser spot alignment to microchip LIF detection cell.

### 5.4.3 LIF Detection Characterization

Background noise level of the LIF detection system was examined. Fluorescein solution samples with different concentrations were injected into our embedded HPLC microchip where no stationary-phase particles were packed. A 1.5 mW/488 nm laser spot was focused on the LIF cell, which has a cell volume of 0.5 nL, to excite fluorescein molecules. An Op-Amp circuit with an amplification resistance of 66 M $\Omega$  was used to convert photodiode output current into a voltage signal. Signal was sampled at a frequency of 10 Hz and signal standard deviation was calculated and plotted versus signal as shown in Figure 5-15. LIF signal increased linearly with the fluorescein concentration in the sample. The limit of detection (LOD) of the system was calculated to be 125 nM with an SNR of 10. One should note that the LOD of the LIF system can be improved by more than three orders of magnitude by replacing the photodiode with a photomultiplier tube (PMT) [6].

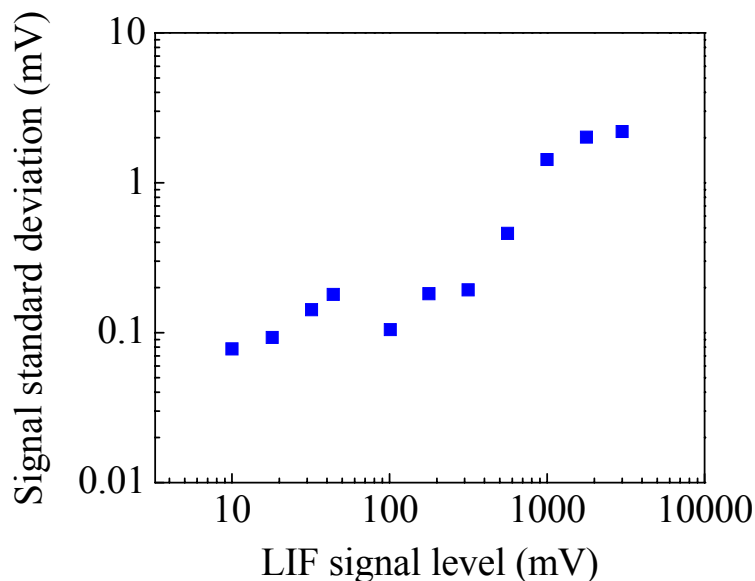


Figure 5-15: LIF signal standard deviation vs. signal level.

## 5.5 Capacitively-Coupled Contactless Conductivity Detection

Capacitively-coupled contactless conductivity detection ( $C^4D$ ) was first proposed in 1998 [9] for analyte sensing in capillary electrophoresis (CE) systems. A  $C^4D$  setup is composed of two electrode rings on the outside of the capillary that act as capacitors (Figure 5-16). To monitor the conductance of the solution in the capillary over the detection gap (the distance between the electrodes) an AC voltage is applied to the inlet electrode giving a current through the background solution, which is picked up by the second electrode and amplified and then recorded. Since the sensing electrodes of  $C^4D$  can be attached to the outside surface of the separation devices (for both conventional capillary or microchip systems), the overall system design and fabrication process is greatly simplified. Also, since the sensing electrodes are not in direct contact with the electrolyte solution as in regular conductivity sensing cases, the electrodes will never be corroded by the solution.

While  $C^4D$  has been used in microchip CE system for sensing of assorted cations and anions [10], it has never been used in microchip HPLC systems [3]. Our work below represents the first investigation into the feasibility of using  $C^4D$  in microchip HPLC for analyte detection.

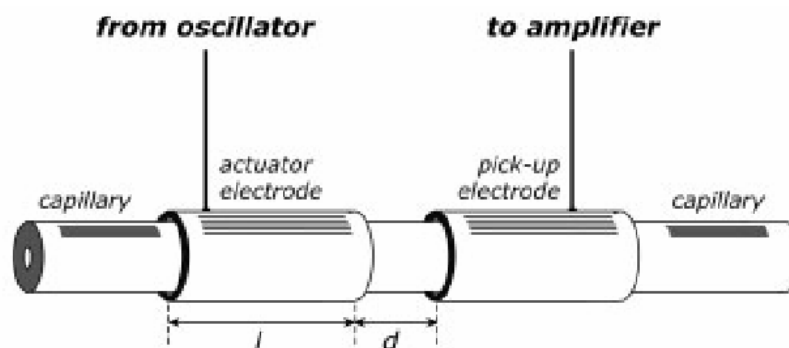


Figure 5-16:  $C^4D$  for capillary separation systems [11].

### 5.5.1 Sensor Design and Fabrication

The sensor fabrication process was described previously in 5.3.1, with which the multiple-mask embedded HPLC system was built. As shown in Figure 5-17, the fabricated  $C^4D$  device is composed of interdigitated electrodes that are on top of the silicon dioxide layer and is encapsulated by parylene. Silicon underneath the  $C^4D$  was etched away by  $XeF_2$  through the parylene openings between the interdigitated electrodes. Electrical routing and contact pad area outside the sensing zone was minimized to reduce the parasitic capacitance.

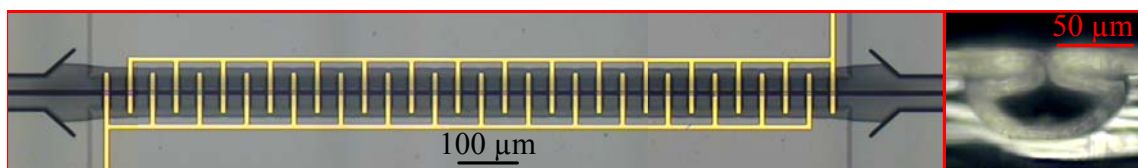


Figure 5-17:  $C^4D$  for microchip HPLC system.

### 5.5.2 Sensor Characterization

Figure 5-18 shows the equivalent circuit model of the  $C^4D$  cell.  $C_W$  is the capacitance between the interdigitated electrodes and the solution where the parylene/oxide layer is the capacitor dielectric. The capacitance of  $C_W$  was calculated to be 63 pF.  $R_S$  is the solvent resistance between the interdigitated electrodes. In general,  $R_S$  should have a resistance ranging between 1 k $\Omega$  to 1 M $\Omega$  when the sensor is filled with the electrolyte solution.  $C_P$  is the parasitic capacitance between the electrodes (including fingers, routings, and contact pads). The capacitance of  $C_P$  was measured using the HP4192A impedance analyzer to be 1.92 pF.

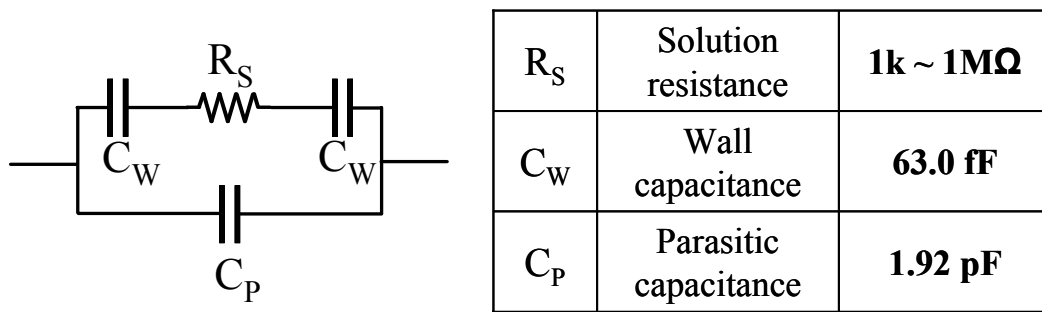


Figure 5-18: The equivalent circuit model of the  $C^4D$  cell and its component values.

For high  $C^4D$  sensitivity,  $R_S$  will need to dominate the overall cell impedance. However, for the microchip  $C^4D$  system, things go the opposite way. In other words,  $R_S$  is small due to the short distance between electrodes,  $C_W$  is small (therefore large impedance) due to the small interdigitated electrode area,  $C_P$  is large (therefore small impedance) due to the large size electrical contact pads and the silicon substrate underneath. Therefore, it can be expected that the microchip  $C^4D$  sensitivity will be much lower than that of the capillary  $C^4D$ . Figure 5-19 shows the impedance analysis of the  $C^4D$  cell. Results show that even at 1 MHz sensing frequency, the cell impedance

magnitude changes by less than 0.1% when the solution resistance changes from 1 M $\Omega$  to 10 k $\Omega$ .

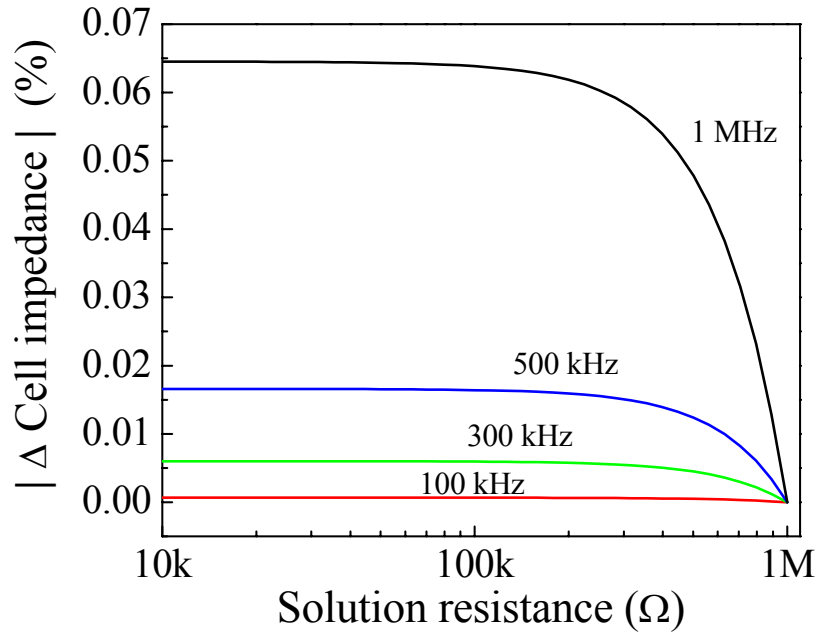


Figure 5-19: Impedance analysis of the C<sup>4</sup>D cell.

Figure 5-20 then shows the experimental results of the C<sup>4</sup>D transient responses for different cell-filling media. The voltage source is a 300 kHz,  $\pm 10$  V square wave. Load resistance  $R_L$  is 50.7 k $\Omega$ . First-order-exponential-fitting to the transient response generated time constants of 156 ns, 148 ns, and 137 ns for air, DI water and 1M salt water, respectively.

Judging from the analysis above, it is clear that the native microchip C<sup>4</sup>D sensitivity is too low and not practical for conductivity sensing. However, several approaches are available to improve the C<sup>4</sup>D sensitivity. For examples, increasing the interdigitated electrode distance to increase solution resistance; increasing interdigitated electrode area and reducing parylene coating thickness to increase  $C_W$  capacitance. It is

also possible to use off-chip circuitry to enhance  $C^4D$  sensitivity which will be discussed in the following section.

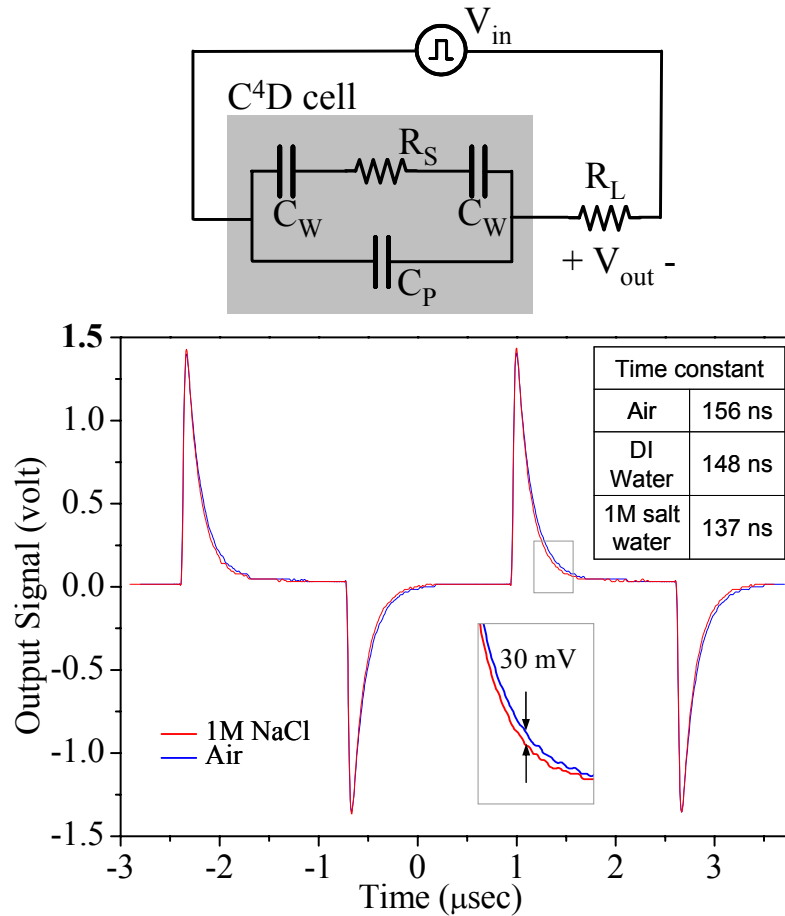


Figure 5-20: The transient responses of the  $C^4D$  cell when the cell was filled with different media.

### 5.5.3 Resonance-Induced Sensitivity Enhancement for $C^4D$

A novel technique will be introduced in this section, which improves the  $C^4D$  sensitivity by more than 10,000 times. The concept of the Resonance-Induced Sensitivity Enhancement (RISE) method is shown in Figure 5-21. An inductor  $L_S$  with an internal serial resistance of  $R_{LS}$  is put in parallel with the  $C^4D$  cell (Figure 5-21(a)). The serial

circuit of  $L_S$  and  $R_{LS}$  can be transformed to an equivalent parallel circuit that composes an inductor  $L_P$  and a resistor  $R_{LP}$  according to the following equation (Figure 5-21(b)):

$$\begin{aligned} Q_{LR} &= \frac{W_0 L_S}{R_{LS}} \\ L_P &= L_S \left( \frac{Q_{LR}^2 + 1}{Q_{LR}^2} \right) \\ R_{LP} &= R_{LS} (Q_{LR}^2 + 1) \end{aligned} \quad (5.3)$$

where the resonant frequency  $W_0$  will be defined latter. The two parylene wall capacitor  $C_W$  is combined and becomes  $C_{W'}$ , where:

$$C_{W'} = \frac{C_W}{2} \quad (5.4)$$

Then, the serial circuit of  $C_{W'}$  and  $R_S$  can be transformed to an equivalent parallel circuit that composes a capacitance  $C_{WP'}$  and a resistor  $R_{SP}$  according to the following equation (Figure 5-21(c)):

$$\begin{aligned} Q_{CR} &= \frac{1}{R_S W_0 C_{W'}} \\ C_{WP'} &= C_{W'} \left( \frac{Q_{CR}^2}{Q_{CR}^2 + 1} \right) \\ R_{SP} &= R_S (Q_{CR}^2 + 1) \end{aligned} \quad (5.5)$$

Now, as shown in Figure 5-21(d), the resistance  $R_{SP}$  and  $R_{LP}$  are combined into  $R_{total}$  and the capacitance  $C_{WP'}$  and  $C_P$  are combined into  $C_{total}$  where:

$$\begin{aligned} R_{total} &= R_{SP} // R_{LP} \\ C_{total} &= C_P + C_{WP'} \end{aligned} \quad (5.6)$$

The operation resonant frequency  $W_0$  is chosen so that  $C_{total}$  and  $L_P$  reaches resonance and the cell impedance will become a pure resistance which is  $R_{total}$ . Furthermore, the

component values can be designed so that  $R_{LP}$  is much larger than  $R_{SP}$  and therefore  $R_{total}$  is dominated by  $R_{SP}$  which has a strong dependence on the solution resistance  $R_S$ . We will show that at this resonant frequency the C<sup>4</sup>D sensitivity is dramatically enhanced by more than 10,000 times. The resonant frequency is derived as follows:

$$\begin{aligned}
W_0 &= \frac{1}{\sqrt{L_P C_{total}}} \\
&= \frac{1}{\sqrt{L_S \left( \frac{Q_{LR}^2 + 1}{Q_{LR}^2} \right) \left( C_P + C_{W'} \left( \frac{Q_{CR}^2}{Q_{CR}^2 + 1} \right) \right)}} \\
\frac{1}{W_0^2} &= L_S \left( \frac{Q_{LR}^2 + 1}{Q_{LR}^2} \right) \left( C_P + C_{W'} \left( \frac{Q_{CR}^2}{Q_{CR}^2 + 1} \right) \right) \\
&= L_S \left( \frac{\left( \frac{W_0 L_S}{R_{LS}} \right)^2 + 1}{\left( \frac{W_0 L_S}{R_{LS}} \right)^2} \right) \left( C_P + C_{W'} \left( \frac{\left( \frac{1}{R_S W_0 C_{W'}} \right)^2}{\left( \frac{1}{R_S W_0 C_{W'}} \right)^2 + 1} \right) \right) \\
&= \left( \frac{(W_0 L_S)^2 + R_{LS}^2}{W_0^2 L_S} \right) \left( C_P + \frac{C_{W'}}{1 + (R_S W_0 C_{W'})^2} \right)
\end{aligned} \tag{5.7}$$

After discarding the complex and negative solution of  $W_0$  in (5.7), the only solution left is:

$$W_0 = \frac{1}{\sqrt{2}} \left( \sqrt{\frac{1}{C_P C_{W'}^2 L_S^2 R_S^2} (-C_P L_S^2 - C_{W'} L_S^2 + C_{W'}^2 R_S^2 (L_S - C_P R_{LS}^2) + \sqrt{-4C_P C_{W'}^2 L_S^2 R_S^2 (-L_S + (C_P + C_{W'}) R_{LS}^2) + (C_{W'} L_S (L_S - C_{W'} R_S^2) + C_P (L_S^2 + C_{W'}^2 R_S^2 R_{LS}^2))^2}} \right) \tag{5.8}$$

The overall impedance at the resonant frequency is derived as follows:

$$\begin{aligned}
R_{total} &= \frac{R_{LP} R_{SP}}{R_{LP} + R_{SP}} \\
&= \frac{R_{LS} (Q_{LR}^2 + 1) R_S (Q_{CR}^2 + 1)}{R_{LS} (Q_{LR}^2 + 1) + R_S (Q_{CR}^2 + 1)} \\
&= \frac{R_{LS} \left( \left( \frac{W_0 L_S}{R_{LS}} \right)^2 + 1 \right) R_S \left( \left( \frac{1}{R_S W_0 C_{W'}} \right)^2 + 1 \right)}{R_{LS} \left( \left( \frac{W_0 L_S}{R_{LS}} \right)^2 + 1 \right) + R_S \left( \left( \frac{1}{R_S W_0 C_{W'}} \right)^2 + 1 \right)} \\
&= \frac{(R_{LS}^2 + L_S^2 W_0^2) (1 + C_{W'}^2 R_S^2 W_0^2)}{R_{LS} + C_{W'}^2 R_S R_{LS} (R_S + R_{LS}) W_0^2 + C_{W'}^2 L_S^2 R_S W_0^4}
\end{aligned} \tag{5.9}$$

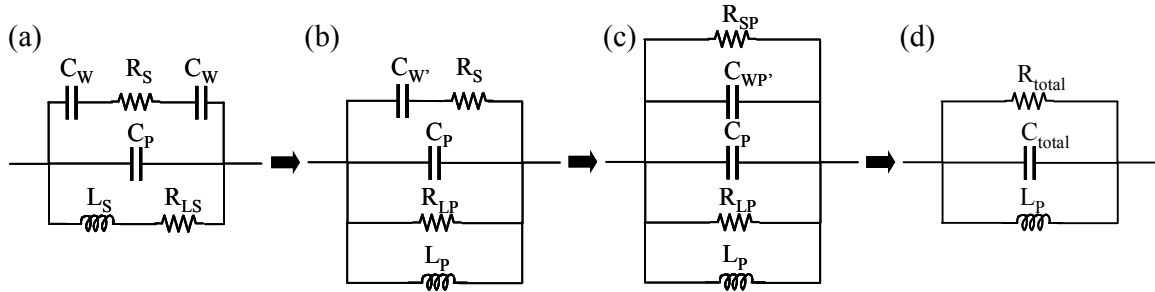


Figure 5-21: The concept of resonance-induced sensitivity enhancement for  $C^4D$ .

To illustrate the resonance-induced sensitivity enhancement technique, a set of the inductor component values were used which contains  $L_S = 15$  mH and  $R_S = 30$   $\Omega$ .  $C^4D$  component values are the same as mentioned earlier, i.e.,  $C_W = 63$  fF and  $C_P = 1.92$  pF. Using those component values, HSPICE analysis of the circuit as shown in Figure 5-21(a) was carried out. Figure 5-22 then shows the analysis results which are curves of total impedance magnitude vs. frequency. Different curves were plotted for different solution resistance  $R_S$  (1 k, 10 k, 100 k and 1 M $\Omega$ ). The resonant frequencies extracted from the HSPICE results exactly match with the calculations from equation (5.8). It is found that the resonant frequency remains at 930.23 kHz for a solution resistance ranging from 1 k $\Omega$  to 100 k $\Omega$  and slightly increases to 930.47 kHz when the solution resistance is 1 M $\Omega$ . Since the resonant frequency is not sensitive to solution resistance in the designated resistance range, we chose the operation frequency to be  $f_0 = 930.23$  kHz or  $\omega_0 = 5844.81$  krad-Hz. Using this resonant frequency,  $R_{total}$  (overall impedance at resonant frequency) versus solution resistance  $R_S$  can be plotted as shown in Figure 5-23. It is amazing to see that the overall impedance magnitude changes by 765% or 832% when the solution resistance changes from 1 M $\Omega$  to 10 k $\Omega$  or to 1 k $\Omega$ . Compared with the native  $C^4D$  performance introduced earlier (operating at 1 MHz), the sensitivity

enhancement is more than 4 orders of magnitude. It is clear that the resonance-induced sensitivity enhancement technique makes our  $C^4D$  sensitive enough for conductivity sensing in microchip HPLC. Figure 5-24 shows the analysis results of cell impedance fluctuation caused by component value changes.

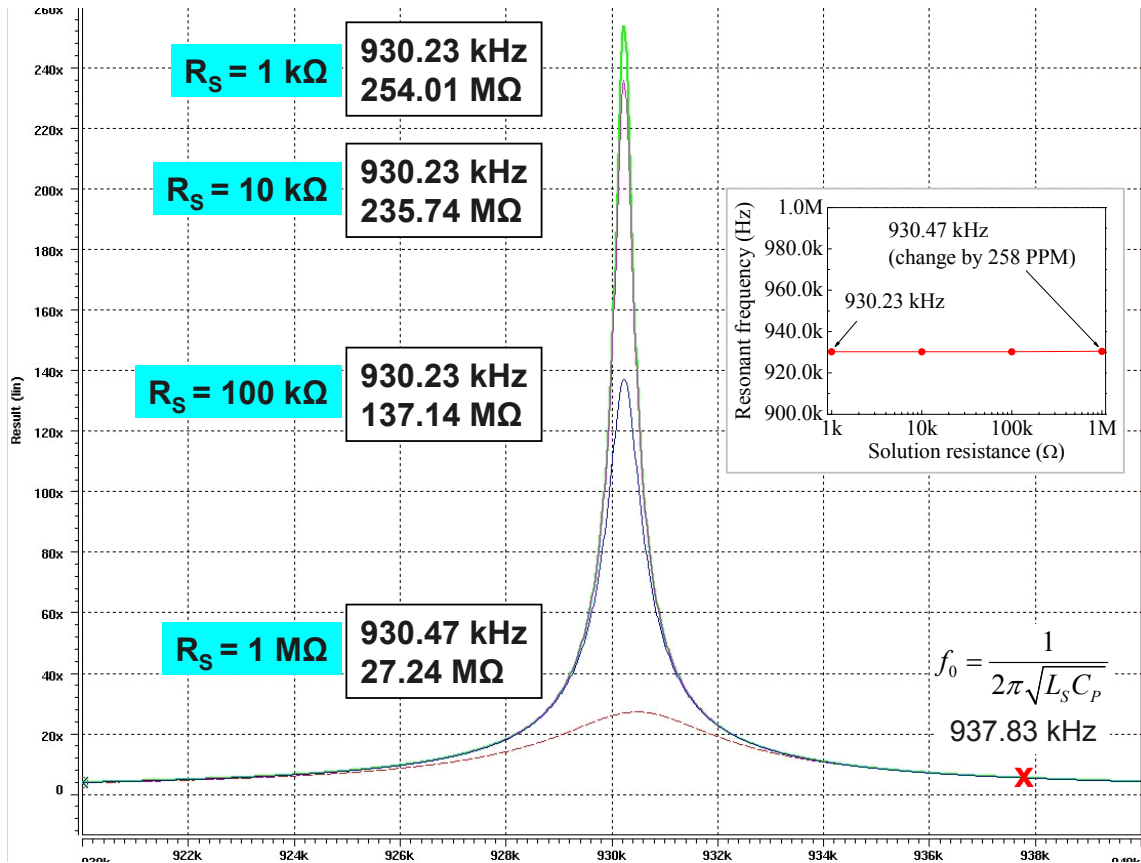


Figure 5-22: HSPICE analysis of total impedance magnitude vs. frequency. From top to the bottom, curves were plotted for a solution resistance of 1 k, 10 k, 100 k, and 1 MΩ.

As a first step to experimentally verify the RISE method, a circuit as shown in Figure 5-21(a) was assembled using discrete components. Components values were :  $C_W = 18.2$  nF;  $C_P = 0.1$  μF;  $L_S = 8.64$  mH;  $R_{L_S} = 78.8$  Ω;  $R_S = 1$  or 1,000 Ω. Circuit impedance was measured for different  $R_S$  values (1 or 1,000 Ω) under the resonant

frequency as defined in (5.8) where the circuit impedance is maximized. The experimental results (as shown in Table 5-2) show great matching between theoretical and experimental values.

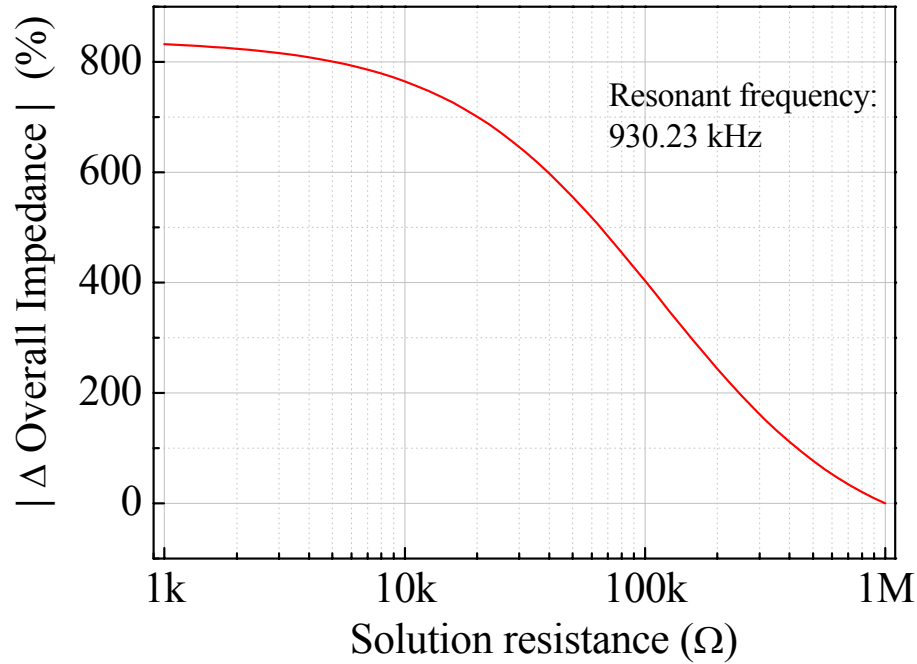


Figure 5-23: Overall impedance change versus solution resistance at resonant frequency.

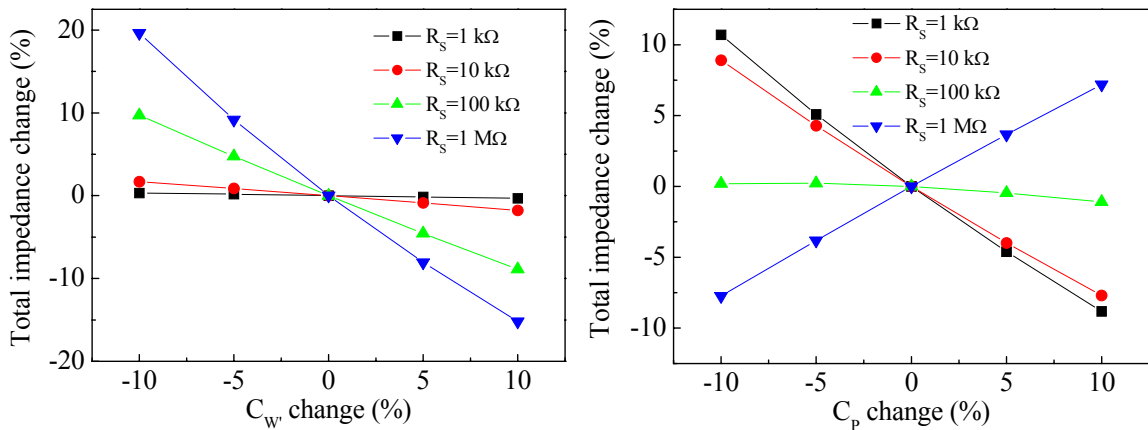


Figure 5-24: Cell impedance fluctuation due to component value variations. (left) Fluctuation caused by  $C_{w'}$  change, (right) fluctuation caused by  $C_p$  change. Operation frequency is fixed at 930.23 kHz.

Table 5-2: Experimental verification of RISE method using discrete circuit components.

	$f_0$ ( $W_0/2\pi$ )	$R_{total}$ (with $L_S$ ) ( $R_S = 1000\Omega$ )	$R_{total}$ (with $L_S$ ) ( $R_S = 1\Omega$ )	$R_{total}$ (w/o $L_S$ ) ( $R_S = 1000\Omega$ )	$R_{total}$ (w/o $L_S$ ) ( $R_S = 1\Omega$ )	Sensitivity Enhancement ratio
Theoretical values	<b>4.98 kHz</b>	<b>939.7 <math>\Omega</math></b>	<b>1004.9 <math>\Omega</math></b>	<b>294.7 <math>\Omega</math></b>	<b>292.9 <math>\Omega</math></b>	<b>11.36</b>
Experimental results	<b>5.16 kHz</b>	<b>940.4 <math>\Omega</math></b>	<b>1004.7 <math>\Omega</math></b>	<b>281.8 <math>\Omega</math></b>	<b>280.0 <math>\Omega</math></b>	<b>10.70</b>
Error	<b>3.61%</b>	<b>0.07%</b>	<b>-0.02%</b>	<b>-4.38%</b>	<b>-4.40%</b>	<b>-5.81%</b>

The proposed resonance-induced sensitivity enhancement (RISE) technique can be used for versatile applications and not just limited to microchip  $C^4D$  for HPLC analyte detection. For example, RISE can be used in the conventional capillary HPLC system to improve the macro-sized  $C^4D$  sensitivity. It can also be used to enhance the sensitivity of general conductivity sensors where electrodes are in direct contact with the electrolyte solution. In this case, it is the double-layer capacitance on top of the electrodes and the parasitic capacitance that will be removed from the circuit using RISE.

Finally, while the analysis shows significant results in terms of sensitivity enhancement (more 10,000 times enhancement), the optimal operation of this technique does require certain conditions. For example, the resonant frequency needs to be precisely measured before the sensing operation. The ability to maintain the resonant frequency for the input signal or to track and tune for the time-dependent resonant frequency during sensing operation decides the stability and reliability of this technique. External factors such as temperature, moisture, and charged objects that can contribute to the variation of component values such as capacitance and resistance should be shielded from the system so to maintain a stable resonant frequency for the system.

## **5.6 LABVIEW Program for Complete HPLC Procedure Control**

### **5.6.1 Program Design**

In order to achieve reproducible chromatography results, it is necessary to reduce manual operation steps such as sample loading or pumping schedule control throughout the separation process. We have therefore developed a complete LABVIEW program that allows users to input all necessary chromatography parameters such as sample injection volume, mobile-phase flow rate, and chromatography temperature to the program and accordingly it carries out automatic separation tasks for the users.

Figure 5-25 shows the user-interface of the developed LABVIEW program. The first part of the program allows users to input temperature-control parameters for the separation task. Basically, the user can define a temporal temperature profile that is composed of linear segments of temperature ramping by inputting temperature/time of each ramping transition point. Users can as well generate a sinusoidal temperature profile with the desired amplitude, frequency, DC offset, and phase shift. Before running the program, users will need to input TCR (temperature coefficient of resistance) information of the on-chip resistive heater, and the program will use that information to monitor chip temperature by measuring the in-situ heater resistance via a multimeter (Agilent 34401A). Temperature feedback control is achieved using the PID (Proportional, Integral, Derivative) mechanism, which is included in the LABVIEW 7.1 or newer version toolset, to output power to the resistive heater via a universal source (HP 3245A). Users can input appropriate PID parameters to be used for different temperature ranges for the best temperature tracking. The multimeter and the universal source mentioned above are communicated through the GPIB interface.

The second part of the program allows users to set up pumping parameters for the sample injection and elution procedures. Two Pico Plus syringe pumps (Harvard Apparatus, Holliston, Massachusetts) are controlled by the LABVIEW program via RS-232 interface. One pump is dedicated to sample injection and the other is dedicated to mobile phase injection. Users can define syringe sizes, pumping flow rate and pumping schedules through this interface.

In terms of data acquisition, the LABVIEW program communicates with the Agilent 34970A (data acquisition unit) via a USB-GPIB interface to retrieve the LIF detection data. The program was designed to automatically save LIF detection data and the measured microchip temperature profile data into separate files. Real-time plots of those data are also shown in the program interface for the users to keep track of the separation progress.

### **5.6.2 Program Performance Characterization**

The finished LABVIEW program mentioned above was further examined for its temperature-control performance. Data sampling and temperature feedback control were carried out at a frequency of 10 Hz. PID coefficients used for all testing are listed in Table 5-3. Due to the fact that chip temperature measurement is susceptible to various noise sources, the derivative action in the PID controller can sometimes cause the output power to fluctuate wildly. In these circumstances it is better to use a PI controller or set the derivative action of a PID controller to zero. To carry out the characterization, microchips introduced in 4.2.2 with appropriate thermal-isolation packaging were used throughout the testing.

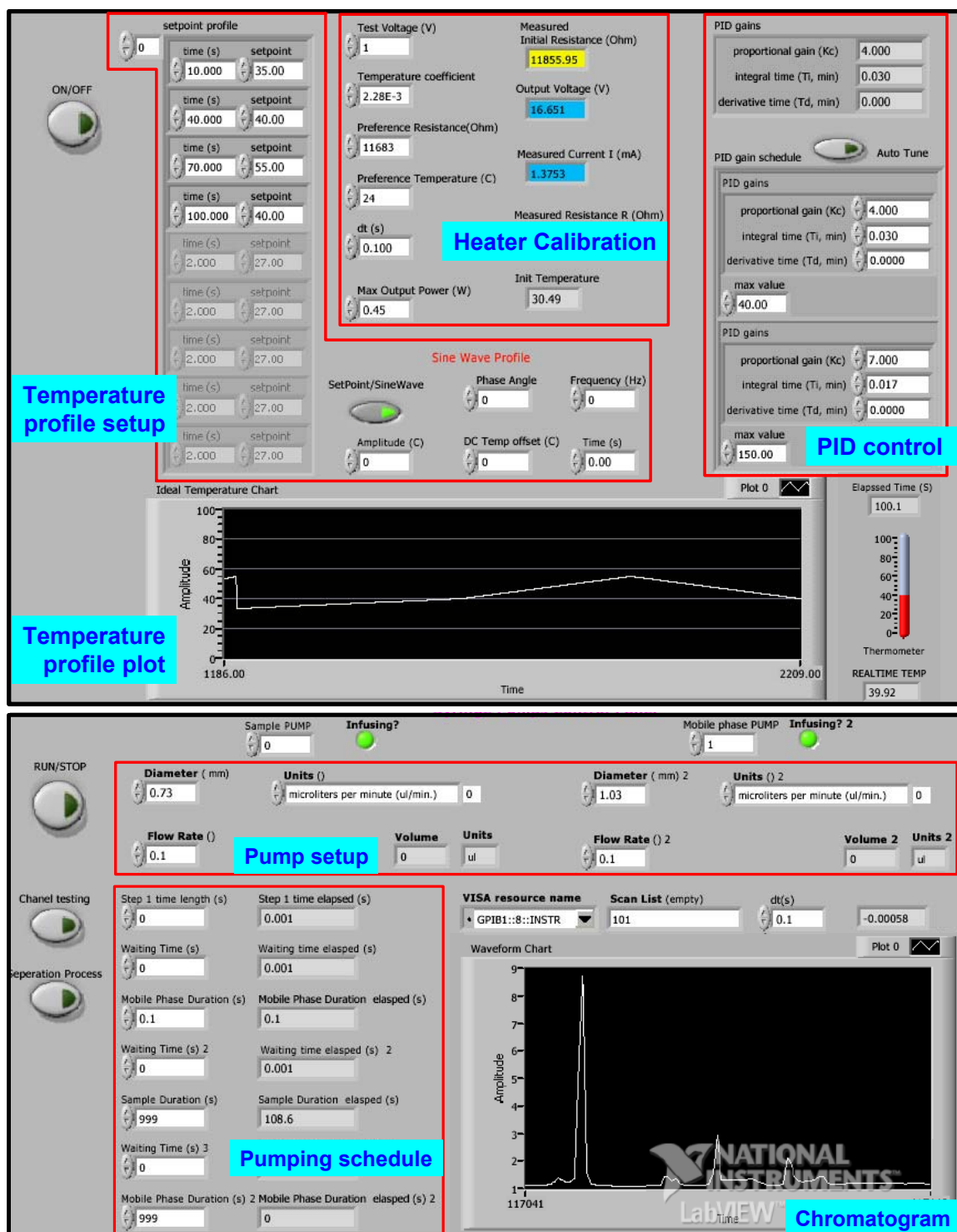


Figure 5-25: User-interface of the developed LABVIEW program for the complete automatic control of HPLC procedures, (top) temperature control panel, (bottom) pumping control panel.

Table 5-3: PID parameters used in all testing experiments.

	Proportional gain (Kc)	Integral gain (Ti, min)	Derivative time (Td, min)
Low temperature (0 to 40 °C)	5.000	0.030	0.000
High temperature (40 to 150 °C)	7.000	0.017	0.000

Figure 5-26 shows the excellent temperature-tracking ability of the program for both the multiple-linear-segment temperature profile and the sinusoidal temperature profile. The constant-temperature maintenance ability of the program at various temperature levels was examined as well. Table 5-4 summarizes the temperature standard deviation for various designated temperature levels. The best constant temperature maintenance performance occurred at 50 °C where a temperature standard deviation of 0.11 °C was obtained. Finally, Figure 5-27 shows the step-function temperature profile tracking ability of the program. A rise time (time length from the beginning of the input step to 90% of the output step height) of 2.3 s and fall time of 5.6 s were obtained. The reason for the longer fall time compared with the rise time is due to the fact that the maximum “cooling power” is limited by the heat dissipation rate from the chip surface to the air while “heating power” does not have such a limitation. However, a Peltier cooler can be used to further reduce the fall time.

From the above characterization results, we are assured that the developed LABVIEW program can easily serve the purpose of chromatographic temperature control of microchip HPLC system. It is also feasible to use this program for other lab-on-a-chip applications that require temperature profile programming such as polymerase chain reaction or micro-bioreactor which were mentioned in chapter 4.

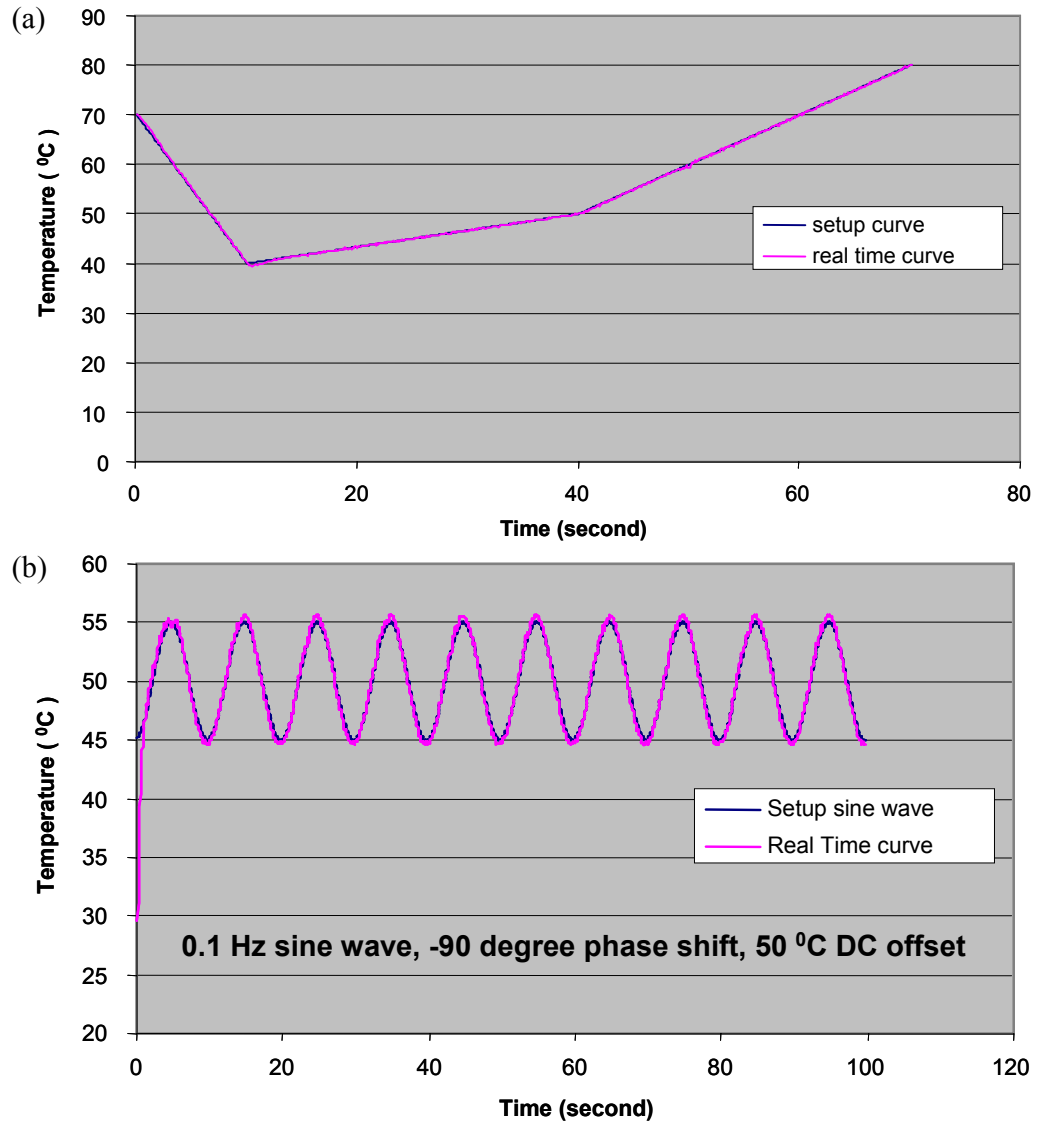


Figure 5-26: Examples of temperature profile tracking performance of the LABVIEW program, (a) multiple-linear-segment profile, (b) sinusoidal profile.

Table 5-4: Temperature standard deviations at various temperature levels.

Temperature (°C)	30	40	50	60	70
Standard Deviation (°C)	0.24	0.19	0.11	0.23	0.14

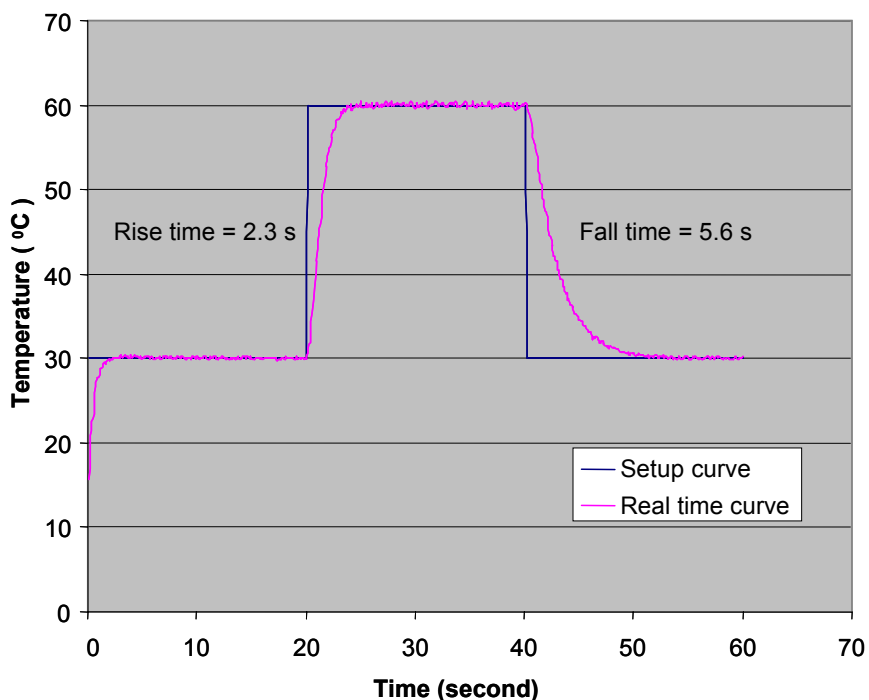


Figure 5-27: Step-function temperature profile tracking.

## 5.7 Examples of Separation

With the developed embedded microchip HPLC, incorporated LIF detection, and LABVIEW program, we are ready to evaluate the overall system chromatographic performance. Figure 5-28 shows the sample injection and elution procedures that are executed automatically by the developed LABVIEW program. Note that the sample outlet as shown in Figure 5-11 (a) is sealed in this sample injection procedure for flexible sample volume injection. In step 1, both sample and mobile phase are injected to the separation column to guarantee that there is no air bubble trapped in the fluidic path and to set up the sample/mobile phase interface for sample injection control. In step 2, sample injection stops and mobile-phase injection continues to clean up the sample species in the separation column. In step 3, mobile-phase injection stops and sample

injection starts. The injected sample volume is controlled by the sample injection pumping time and flow rate. In step 4, sample injection stops and mobile-phase injection starts to achieve sample elution and detection.

The fabricated multiple-mask embedded HPLC system with incorporated LIF detection was used for the chromatographic performance demonstration. The separation column (50  $\mu\text{m}$  x 60  $\mu\text{m}$  x 22 mm) was packed with 5- $\mu\text{m}$ -C18 porous silica particles using a 200 psi slurry-packing technique. Separation reproducibility and efficiency of the system will be addressed in the following sections.

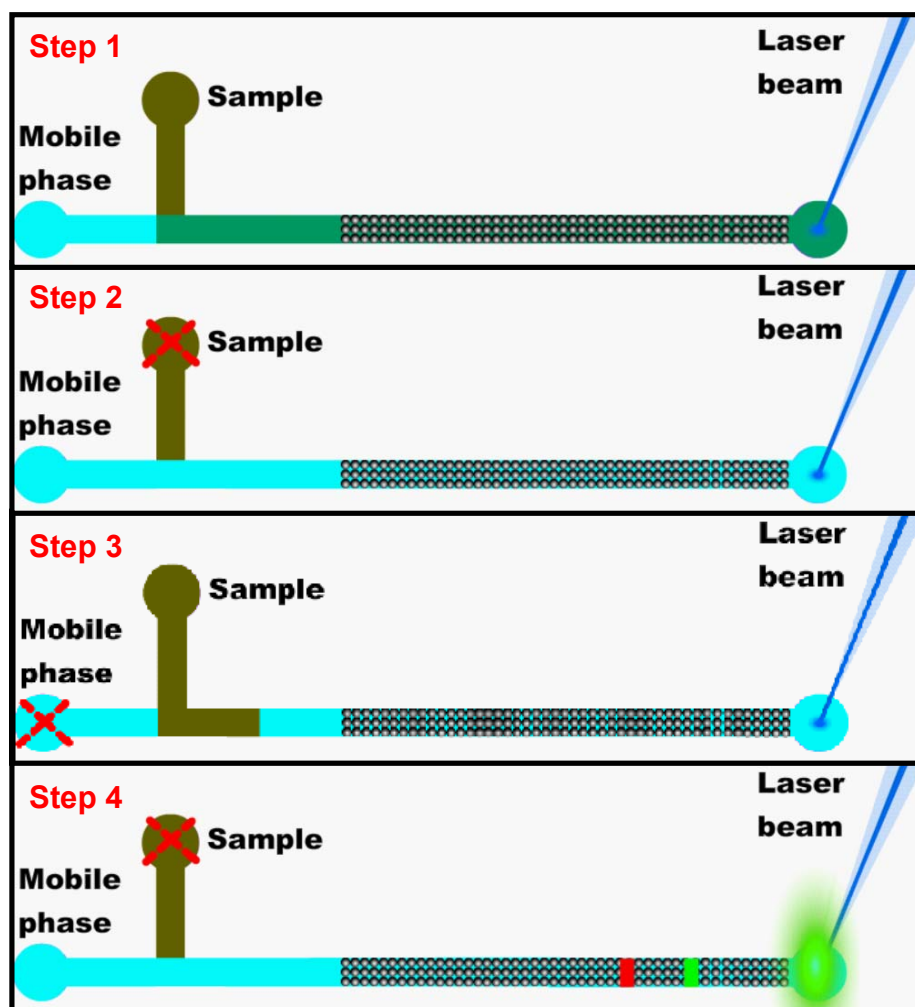


Figure 5-28: Sample injection and elution pumping procedures.

### 5.7.1 Daunorubicin Elution

Figure 5-29(a) shows the single peak elution of daunorubicin which has native fluorescence. Three identical elution procedures were carried out and extremely well matching among the three chromatograms including peak heights and retention times were obtained which means the sample injection procedure as well as the column condition were pretty robust. Number of theoretical plates  $N$  and plate height  $H$  of the 22-mm-long column is calculated as follows:

$$N = 16 \left( \frac{t_R}{w} \right)^2 \approx 1600$$
$$H = \frac{L}{N} = 13.75 \mu\text{m} = 2.75 d_p \quad (5.10)$$

where the plate height of  $2.75 d_p$  falls in the range of 2 to 5 particle diameters for the plate height of conventional HPLC columns.

### 5.7.2 Separation of Daunorubicin and Doxorubicin

To further test the separation performance of our system, a 16.7 nL sample containing a mixture of 16.7 pmole doxorubicin and 8.3 pmole daunorubicin was injected to the microchip HPLC for separation. Both compounds are used in pharmaceuticals as anticancer drugs and both compounds have native fluorescence so no derivatization process is necessary for the sample preparation. The chemical structures of the two compounds have a difference of a functional group, where doxorubicin has a hydroxyl group and daunorubicin has a methyl group, which means daunorubicin is more hydrophobic. Figure 5-29(b) shows the successful separation results. Peak resolution is calculated as follows:

$$R_S \equiv \frac{t_{R2} - t_{R1}}{\frac{1}{2} \cdot (w_1 + w_2)} = 2.23 \quad (5.11)$$

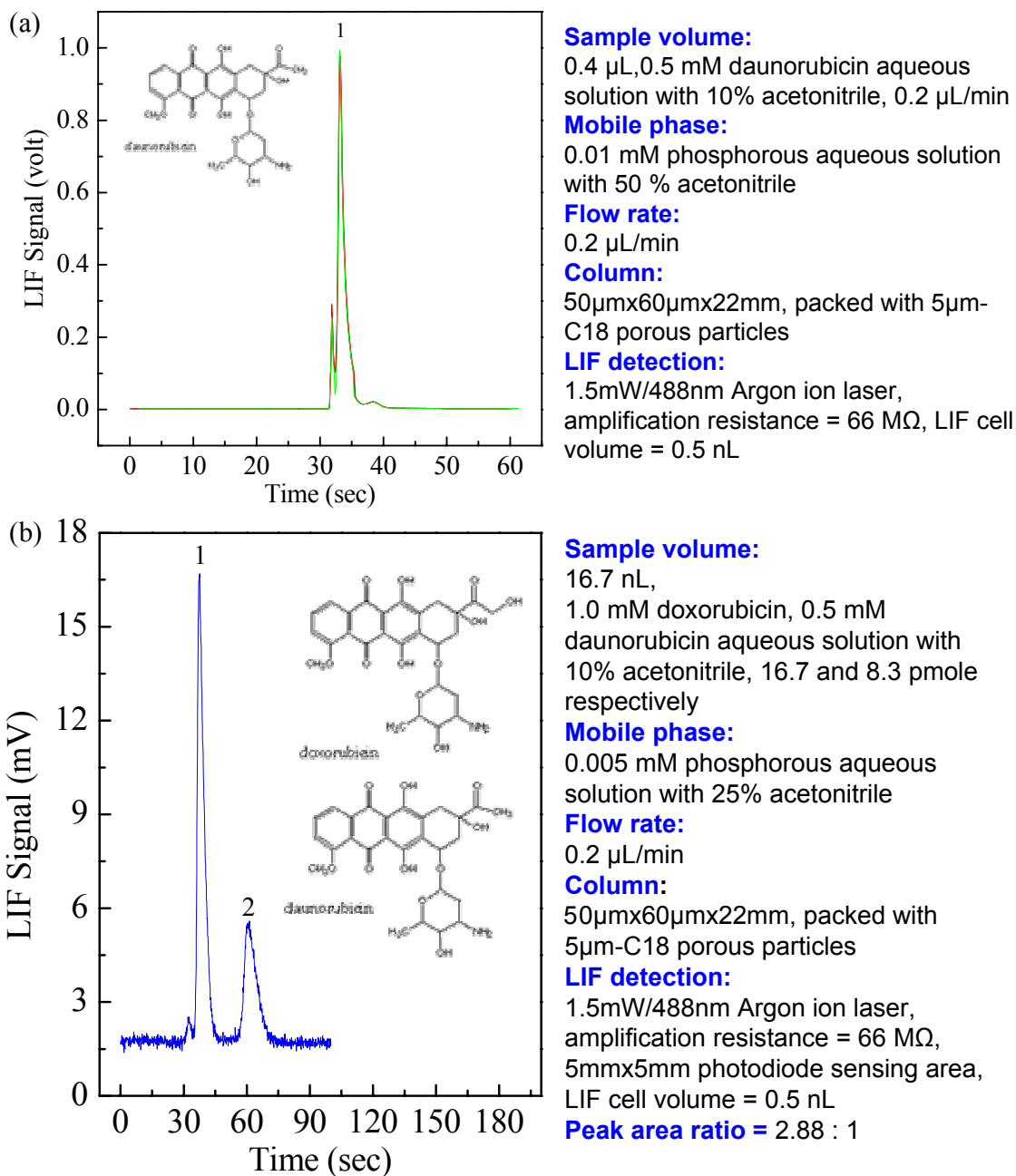


Figure 5-29: Examples of separations, (a) highly reproducible single peak elution of daunorubicin, (b) separation of doxorubicin and daunorubicin.

## 5.8 Conclusions

In this chapter we demonstrated the design and fabrication of novel embedded microchip HPLC systems. Different in fabrication complexity and device functionality, two versions of embedded systems were proposed, the single-mask system and multiple-mask system. Various analyte sensing methods, including LIF detection and capacitively-coupled contactless conductivity detection ( $C^4D$ ) have been studied to be used with the proposed embedded systems. A RISE sensitivity enhancement method was proposed to improve microchip  $C^4D$  sensitivity by more than 10,000 times. A complete LABVIEW program was developed to execute the fully automatic chromatography tasks with on-chip temperature feedback control. System characterization including pressure capacity, analyte detector sensitivity, and chromatographic temperature controllability were carried out. Finally, to evaluate the chromatographic performance of our system, the separation of doxorubicin and daunorubicin was successfully demonstrated using multiple-mask embedded HPLC and LIF detection. Results show that our system provides separation efficiency and reproducibility comparable to conventional HPLC systems.

## 5.9 Bibliography

- [1] C. Y. Shih and Y. C. Tai, "Single-mask technology for on-chip high-pressure HPLC system," presented at the 9th International Conference on Miniaturized Systems for Chemistry and Life Sciences, Boston, USA, 2005.
- [2] Q. He, C. Pang, Y. C. Tai, and T. D. Lee, "Ion liquid chromatography on-a-chip with beads-packed parylene column," presented at the 17th IEEE International Conference on Micro Electro Mechanical Systems (MEMS 2004), Maastricht, The Netherlands, 2004.
- [3] C. Y. Shih, W. Li, and Y. C. Tai, "A novel embedded liquid chromatography system with submicron-sized filter structure and capacitively-coupled contactless conductivity detector," presented at the 20th International Symposium on Microscale Bioseparations, Amsterdam, the Netherlands, 2006.
- [4] K. J. Reynolds and L. A. Colon, "Submicron sized organo-silica spheres for capillary electrochromatography," *Journal of Liquid Chromatography & Related Technologies*, vol. 23, pp. 161-173, 2000.
- [5] J. M. Miller, *Chromatography concepts and contrasts*, 2nd ed. New Jersey: Wiley-Interscience, 2005.
- [6] P. J. Obeid and T. K. Christopoulos, "Continuous-flow DNA and RNA amplification chip combined with laser-induced fluorescence detection," *Analytica Chimica Acta*, vol. 494, pp. 1-9, 2003.
- [7] J. H. Qin, F. C. Leung, Y. S. Fung, D. R. Zhu, and B. C. Lin, "Rapid authentication of ginseng species using microchip electrophoresis with laser-

- induced fluorescence detection," *Analytical and Bioanalytical Chemistry*, vol. 381, pp. 812-819, 2005.
- [8] P. Schulze, M. Ludwig, F. Kohler, and D. Belder, "Deep UV laser-induced fluorescence detection of unlabeled drugs and proteins in microchip electrophoresis," *Analytical Chemistry*, vol. 77, pp. 1325-1329, 2005.
- [9] A. J. Zemann, E. Schnell, D. Volgger, and G. K. Bonn, "Contactless conductivity detection for capillary electrophoresis," *Analytical Chemistry*, vol. 70, pp. 563-567, 1998.
- [10] M. Pumera, J. Wang, F. Opekar, I. Jelinek, J. Feldman, H. Lowe, and S. Hardt, "Contactless conductivity detector for microchip capillary electrophoresis," *Analytical Chemistry*, vol. 74, pp. 1968-1971, 2002.
- [11] A. J. Zemann, "Capacitively coupled contactless conductivity detection in capillary electrophoresis," *Electrophoresis*, vol. 24, pp. 2125-2137, 2003.

---

# CHAPTER 6

---

## PACKING NANOPARTICLES INTO HPLC COLUMN

### 6.1 Introduction

One way to improve LC separation efficiency is to pack the separation column with smaller stationary-phase particles since plate height  $H$  is proportional to the square of the particle diameter [1]:

$$H \equiv \frac{\sigma^2}{L} = c \frac{d_p^2}{D_M} u \quad (6.1)$$

For example, using 30 nm particles instead of 3  $\mu\text{m}$  particles (Figure 6-1) to pack the column can reduce the plate height 10,000 times (assuming porous particles):

$$\frac{(30\text{nm})^2}{(3\mu\text{m})^2} = \frac{1}{10000} \quad (6.2)$$

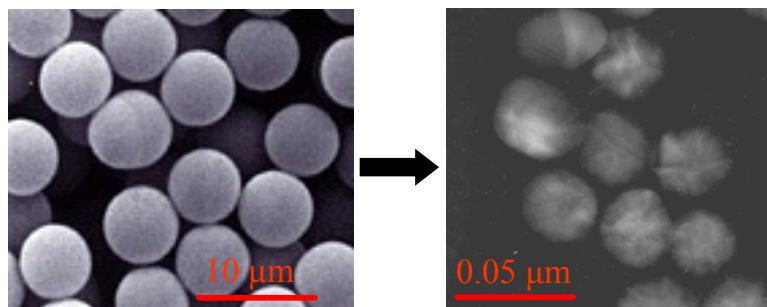


Figure 6-1: Micron-sized and nanometer-sized particles.

However, fabrication of a fully packed or fully filled nanoparticle column is an extremely difficult task. For example, a submicron-sized particle filter or frit is necessary for direct nanoparticle packing and this filter cannot be sealed by particles or impurities during chromatography procedures otherwise the column backpressure will increase dramatically which eventually will damage the column. Besides, packing nanoparticles will require much higher backpressure ( $> 10,000$  psi) since the pressure drop in the packed column is inversely proportional to the square of the particle size as has been mentioned in chapter 2. Due to those challenges, fully packed nanoparticle columns have rarely been achieved before [2]. Instead, nanoparticles have been used to coat the separation column wall [3, 4] or partially fill the column for separation efficiency enhancement purposes [5, 6].

In this chapter, we propose a new approach that involves the molecular self-assembly technique to prepare fully packed nanoparticle columns, which do not require a nano-sized particle filter or extremely high packing pressure. Our prospect is that by using the proposed technology, a new generation nano-HPLC column that has extremely high separation efficiency (for example, millions of plates per centimeter) can be realized [7].

## 6.2 Molecular-Self-Assembly-Assisted Nanoparticle Packing

### 6.2.1 Concept

The proposed approach to achieve nanoparticle packing is named molecular-self-assembly-assisted nanoparticle packing. The idea is to crosslink nanoparticles with some functionalized molecules and form micron-sized clusters before nanoparticles are packed into the separation column [8, 9]. This way, instead of packing individual nanoparticles, we are now virtually packing micron-sized particles into the column, which means both the filter and backpressure issues mentioned in 6.1 can be addressed.

For example, as shown in Figure 6-2, gold nanoparticle solution and thiolated molecule solution can be sent into a microfluidic device through individual channels. While an interface will form between the two flows, gold nanoparticles and thiolated molecules will diffuse across the interface and self-assembly among the two species will occur based on the gold-thiol chemistry [10]. Initially, the assembled compounds might be composed of only a few nanoparticles and molecules. As the compounds travel downstream of the microfluidic channel, self-assembly will continue to happen to the compounds, which will grow bigger either by taking in more nanoparticles and molecules or by merging with other similar-sized compounds. With the appropriate assembly time and assembly efficiency, micron-sized or even bigger compounds can be formed. Those micron-sized compounds are then packed into the separation column against a micron-sized particle filter.

The functionalized molecules mentioned above are not just used for crosslinking nanoparticles. More importantly, they can be designed to provide specific surface property to the gold nanoparticles to serve separation purposes. For example, alkyl-chain

molecules provide a hydrophobic property that can be used for reversed-phase liquid chromatography [1].

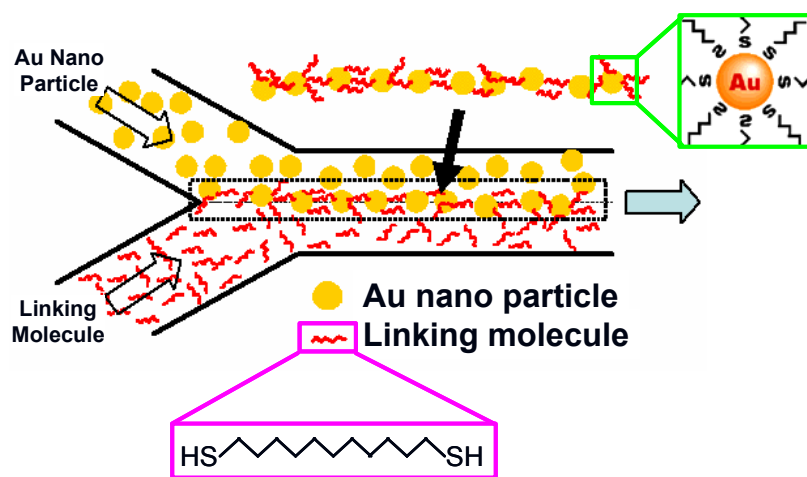


Figure 6-2: Concept of molecular-self-assembly-assisted nanoparticle packing.

## 6.2.2 System Design and Fabrication

To quickly demonstrate the idea of molecular-self-assembly-assisted nanoparticle packing, we have designed and fabricated PDMS (Sylgard 184) microfluidic devices as shown in Figure 6-3. A silicon mold is first prepared by standard lithography process and DRIE etching. Microfluidic channels that are 10- $\mu$ m-deep and 50 to 100- $\mu$ m-wide are molded onto PDMS surface using soft lithography as introduced in chapter 1. Liquid access holes are created by punching through PDMS pieces with syringe needles. The PDMS pieces are then bonded to glass slides with overnight baking at 80 °C [11].

As shown in the close-up of Figure 6-3(b), an in-channel pocket formed by PDMS posts is designed to collect the self-assembled compounds in the downstream. Stainless steel cut-tube is inserted into PDMS through hole at one end and the other end is connected to Teflon tubing as shown in Figure 6-3(c). Syringe pumps are used to deliver gold nanoparticle solution and thiolated molecule solution into the PDMS device.

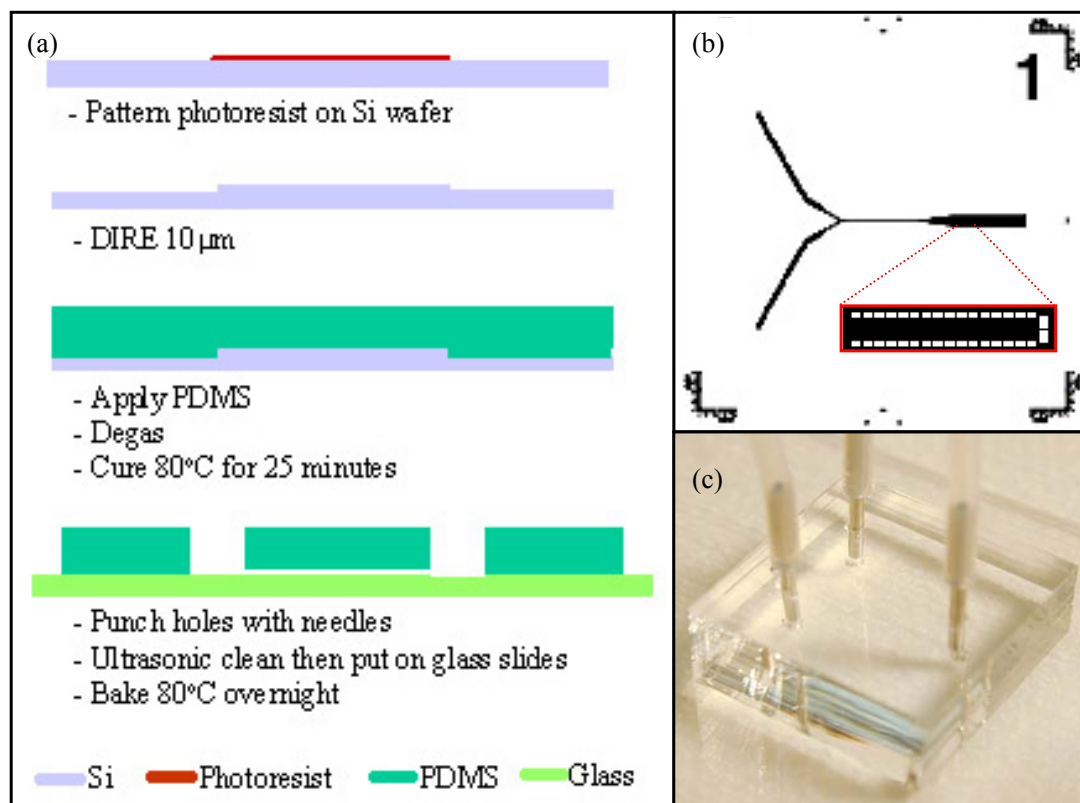


Figure 6-3: (a) The process, (b) the design, and (c) the fabricated device of the PDMS/glass microfluidic system.

### 6.2.3 Molecular-Self-Assembly Characterization

The success of the proposed nanoparticle packing approach counts on the conjugation reaction between the thiol groups of the crosslinking molecules and the gold nanoparticles. Therefore, a great amount of effort has been put into studying the solvent effects, gold nanoparticle size effects, and temperature effects on the conjugation efficiency [8]. The purpose of the study was also to locate working self-assembly parameters, which include choices of crosslinking molecules, solvents, nanoparticle sizes, and reaction temperature that can later be used in microchip HPLC systems for nanoparticle packing.

To study the gold-thiol conjugation efficiency under various conditions, we have engineered special thiolated “model molecules” (bisdisulfide/ $C_{28}H_{34}O_4S_4$ ) as shown in Figure 6-4. With the model molecules we then studied the solvent effects, gold nanoparticle size effects and temperature effects to determine the working conditions for gold nanoparticle-model molecule conjugation.

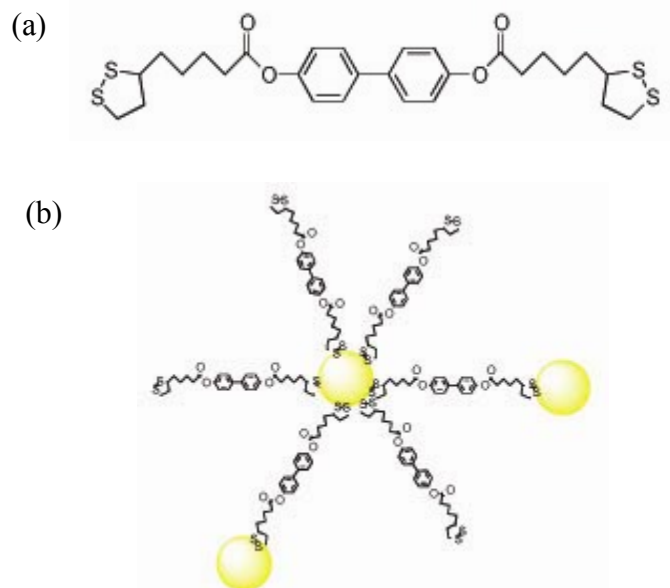


Figure 6-4: (a) Chemical structure of the bisdisulfide model molecule, (b) a schematic plot of the assembled nanoparticle-molecule compound.

First of all, we found that the model molecules do not dissolve well in water (due to its hydrophobic backbone). Meanwhile, they can dissolve easily in DCM ( $>100$  mM), and much less in acetone (about 1 mM), and ethanol ( $<100$   $\mu$ M). On the other hand, the colloidal gold nanoparticle solution from British Bio-cell Inc. (BBI) is a water-based system. The first task is therefore to find a solvent system that can dissolve both species to some extent as well as allow conjugation reaction among species to happen in that solvent system. Figure 6-5 then shows our solvent system screening procedures. In the

negative control experiment, solvent A is just pure solvent while solvent B is used to resuspend gold nanoparticles that will be extracted from the original aqueous solution using centrifugation. Solvent A and solvent B are then mixed. Since no model molecules are present in the mixture, no conjugation reaction or assembly should happen and the mixture should remain reddish, which is characteristic color of a stable gold nanoparticle solution. If the mixture changes color (from red to purple/black) or even generates some precipitates, that means the solvent system destabilizes gold nanoparticles and results in nanoparticle aggregation [12]. Those solvent systems that destabilize gold nanoparticles will be discarded while other solvent systems which remain reddish after mixing will enter the next stage of solvent screening which is the assembly test. In the assembly test stage, solvent A will be saturated with model molecules at room temperature and solvent B will be used to resuspend gold nanoparticles. After mixing solvent A and solvent B, if the mixture color remains reddish, that means conjugation reaction among molecules and nanoparticles does not happen. Those solvent systems will be discarded. On the other hand, if the mixture changes its color from red to purple/black or even has precipitates, this means conjugation reaction does happen and the solvent system passes the complete solvent screening test. While the solvent screening procedures seem straightforward, it can occur that some reactions, whether it is nanoparticles destabilization or conjugation reaction, happen at very slow rates (taking hours or days to be observable). In our screening test, we allowed long observation time (24 hours) for the negative control tests so to guarantee long term stability of the solvent system. On the other hand, we limited the reaction observation time to be 5 minutes for the assembly tests so to screen for high-assembly-efficiency solvent systems.

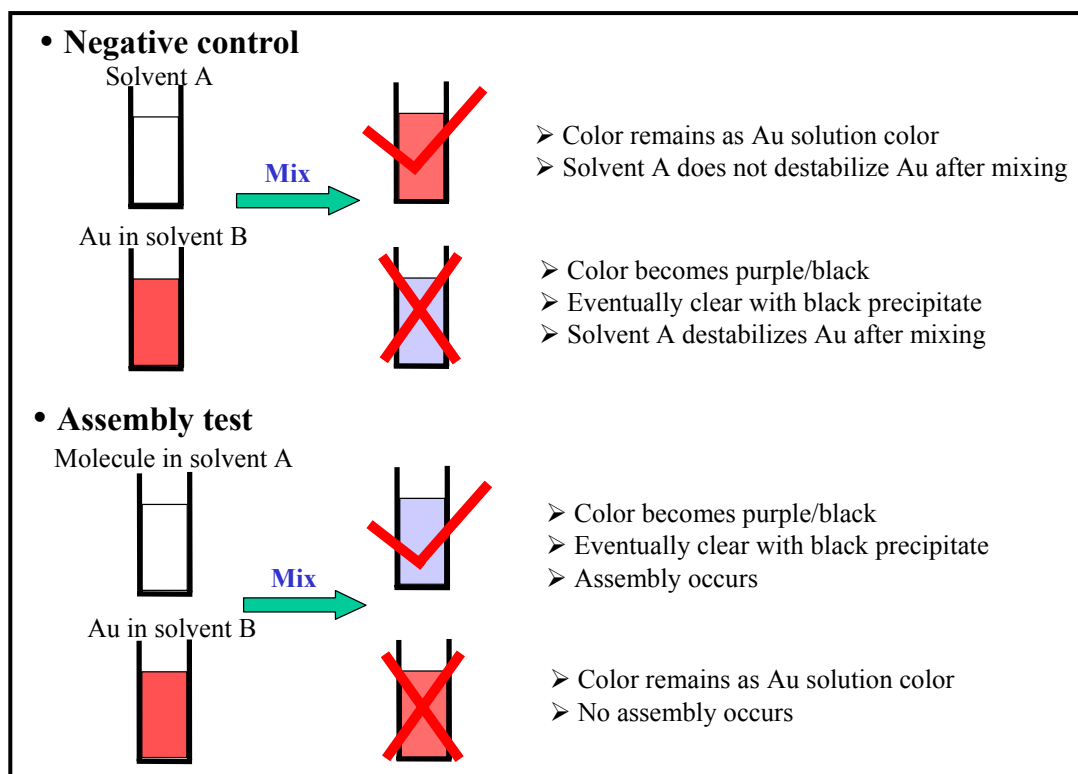


Figure 6-5: Solvent system screening procedures.

• Negative controls					• Assembly tests						
	Au	H <sub>2</sub> O	ethanol	IPA	acetone		Au	H <sub>2</sub> O	Ethanol	IPA	Acetone
Ethanol						Molecule					
IPA						Ethanol					
Acetone						IPA					
DCM						Acetone					
						DCM					

Figure 6-6: Solvent system screening test results.

According to the screening procedures, we then carried out the solvent screening tests. First of all, a method for gold nanoparticle solvent exchange was developed. 30 nm Au nanoparticle aqueous solution ( $2 \times 10^{11}$  particles/mL) from BBI was purchased and used in the experiment. Original aqueous nanoparticle solution was centrifuged in test tubes (10 krpm for 5 min) and the supernatant was removed. Nanoparticles were then resuspended in non-aqueous solvents such as ethanol, IPA, DCM (dichloromethane), or acetone. Molecule solutions were saturated with model molecules (except for DCM) and were filtered using 0.5- $\mu\text{m}$ -sized particle sieves to remove precipitated particles. Figure 6-6 then shows the results of the screening tests. DCM was found to destabilize gold nanoparticles. IPA also destabilized gold nanoparticles slowly. Therefore DCM and IPA are not suitable solvents. For the case where model molecules in acetone were mixed with water, model molecules precipitated out as a result of low solubility in the mixture. For the case where model molecules in acetone and gold nanoparticles in acetone were mixed, no visible reaction was observed, i.e., solution color maintained reddish after mixing for 5 minutes. Finally, we located model molecules in ethanol (saturated with model molecules) and 30-nm-sized gold nanoparticles in ethanol ( $2 \times 10^{11}$  particles/ml) as the simplest and working solvent system. Figure 6-7 then shows the TEM and SEM pictures of the self-assembled compounds formed by the conjugation reaction of model molecules and 30 nm gold nanoparticles using ethanol solvent system in the test tubes.

To confirm that model molecules indeed play a role in forming the self-assembled compound, i.e., the nanoparticles are crosslinked to each other with model molecules, electrical property of the compound was studied. Since the model molecules are electrically insulating, one can expect the self-assembled compound to have a much

higher resistivity compared with the resistivity of an aggregate formed by pure gold nanoparticles.

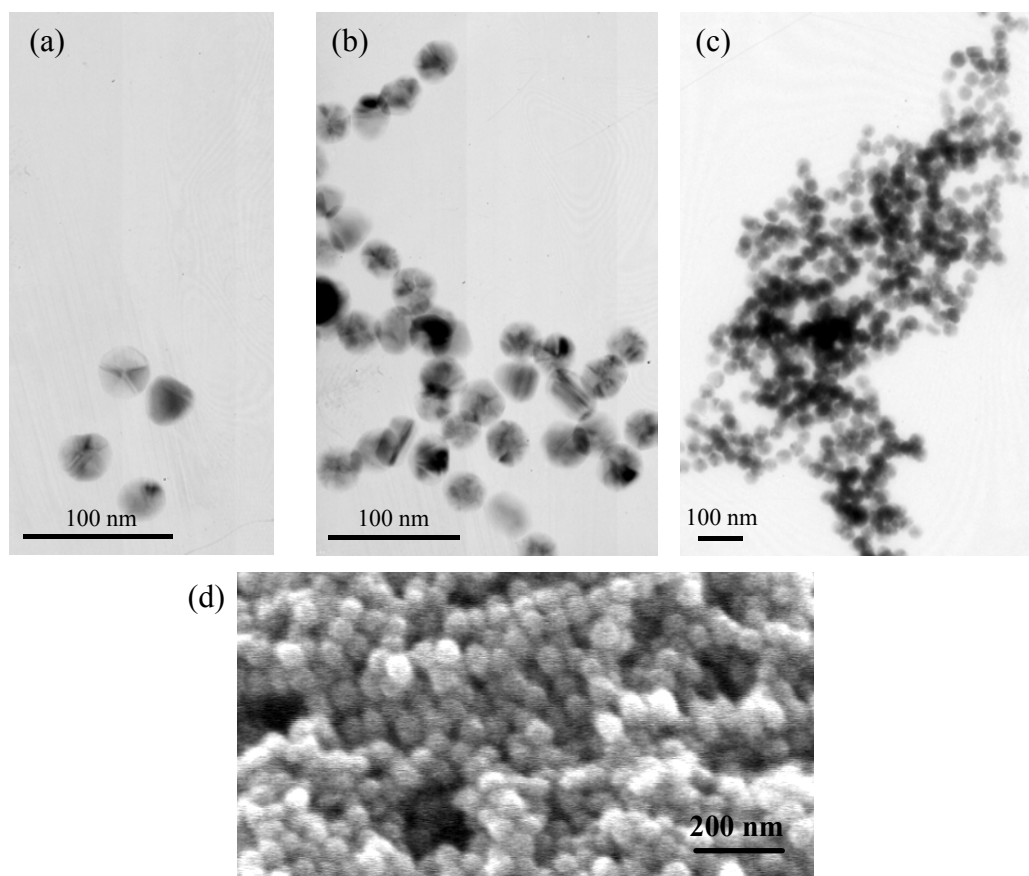


Figure 6-7: TEM and SEM pictures of gold nanoparticles, (a) individual nanoparticles from original aqueous solution, (b, c) self-assembled compound formed by 30 nm gold nanoparticles and model molecules in test tubes. (d) An SEM picture of the self-assembled compound.

To carry out the conductivity analysis of the self-assembled compounds, pieces of self-assembled nanoparticle-molecule compounds were collected from test tubes and were carefully placed onto a gold-electrode-array chip using a pipette to bridge pairs of electrodes as shown in Figure 6-8. 20 hr-air-drying followed by 4 hr-baking at 100 °C

was used to remove extra solvent on the chip and to produce better electrical contact between the compound and the gold electrodes. Wyko surface profiler was used to get geometrical information of the compound for resistivity calculation purpose. Results show that the compound had a resistance of 16.1 G $\Omega$ , which corresponded to a resistivity of  $\sim 10^6$   $\Omega$ -cm based on the geometrical data of the compound. In a control test, we have prepared a pure gold nanoparticle aggregate by adding salt water into the aqueous gold nanoparticle solution. Using the method introduced earlier, the resistance and resistivity of this pure gold nanoparticle aggregate were obtained which were 1.1  $\Omega$  and  $\sim 10^{-5}$   $\Omega$ -cm respectively. The resistivity of the pure gold nanoparticle aggregate is quite comparable to the bulk gold resistivity which is  $\sim 10^{-6}$   $\Omega$ -cm. The fact that the compound formed by nano particles and model molecules has a resistivity 11 orders of magnitude higher than the pure gold nanoparticle aggregate suggests that uniform conjugation among gold nanoparticles and molecules indeed occurred in the assembly process.

Furthermore, the gold nanoparticle size effect on conjugation or self-assembly efficiency was studied. We investigated the size effect by using gold nanoparticles with different particle sizes (5 nm, 10 nm, and 30 nm) in the self-assembly experiments where the ethanol solvent system was used. As shown in Figure 6-9, only 30 nm gold nanoparticles produced visible conjugation reaction. We believe the observed size effect is related to the geometrical shapes of gold nanoparticles. Colloidal gold nanoparticles with a diameter larger than 25 nm exhibit eccentricity and can possess different shapes other than pure spherical shape [13]. The 30 nm gold nanoparticles show crystalline nature with polygonal shapes. These crystal facets provide larger binding area for molecules to crosslink and result in stable and big assembly compounds.

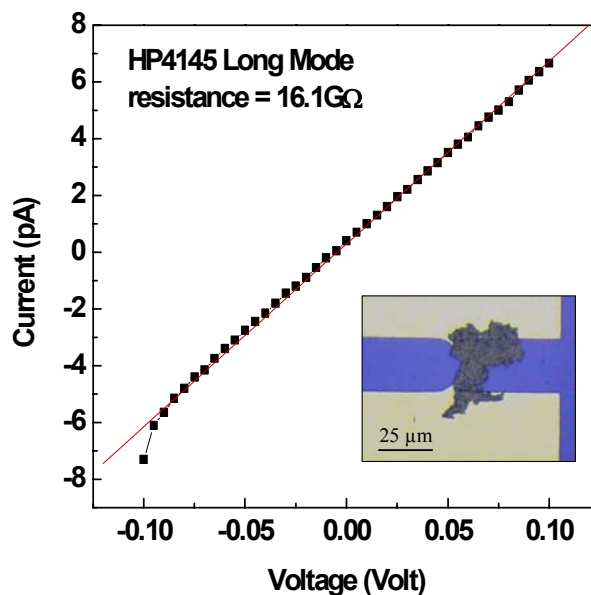


Figure 6-8: Electrical properties of the compound formed by gold nanoparticles and model molecules. The inset shows the measurement setup where the electrode pair was bridged by the compound.

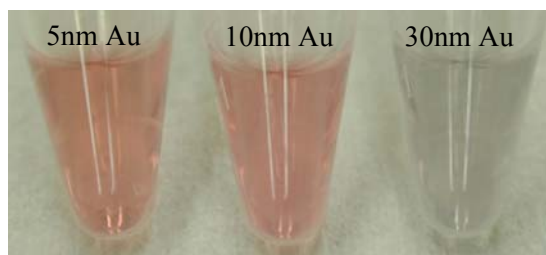


Figure 6-9: Gold nanoparticle size effect on conjugation efficiency.

Finally, temperature effect on the self-assembled compound was studied. The purpose was to see whether high temperature (100 °C), which might be encountered in the temperature-controlled HPLC, could disassociate the compound by breaking the gold-thiol chemical bonds. The conjugation reaction mixture which contained self-assembled compound was heated up to 100 °C for several hours. Results showed no visible change to the mixture color (purple/black), which indicated gold-thiol bonds and the compound structure are stable up to 100 °C.

#### 6.2.4 Column Packing Results and Comments

With the selected solvent system and species concentrations, the self-assembly and packing experiments were then carried out on the PDMS devices that were introduced in 6.2.2. As shown in Figure 6-10, the self-assembly and packing process were monitored in-situ by microscope. Self-assembly occurred around the gold nanoparticle flow and model molecule flow interface and aggregates/compounds were collected successfully in the downstream PDMS pocket. The experiment result successfully demonstrated the concept of molecular-self-assembly-assisted nanoparticle packing.

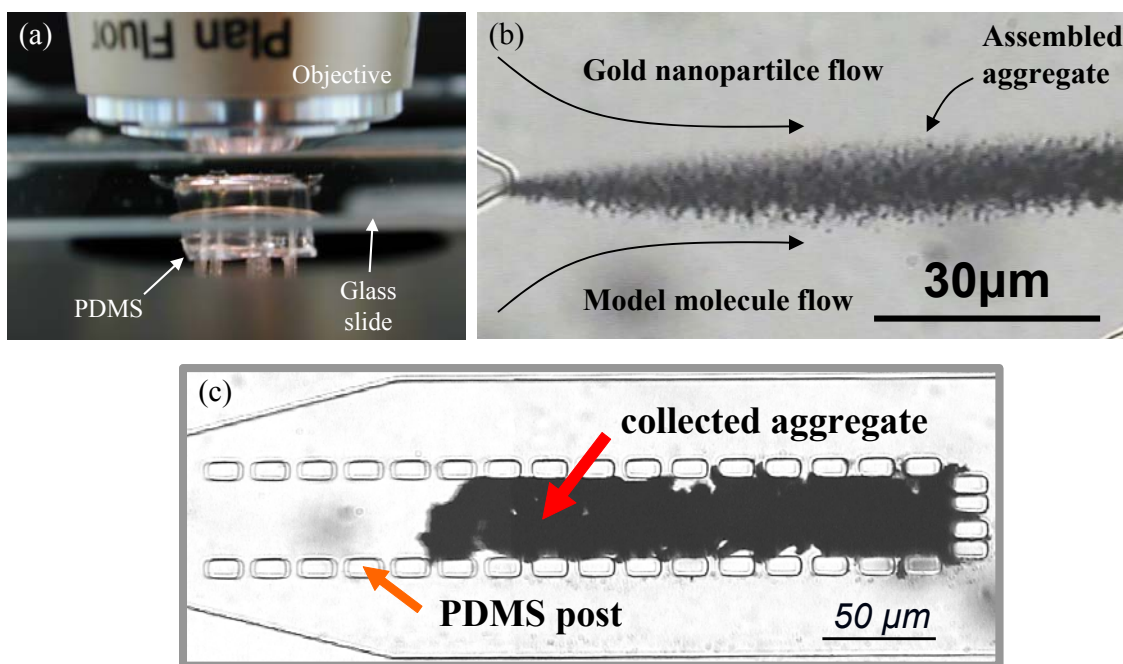


Figure 6-10: Self-assembly and packing tests on PDMS devices. (a) Setup for in-situ monitoring of the assembly and packing process, (b) gold nanoparticle and model molecule self-assembly at flow interface, and (c) self-assembled aggregate collected by the PDMS pocket.

Finally, we demonstrated packing the self-assembled aggregate into an HPLC column as shown in Figure 6-11. In this case, the anchored-type HPLC column was first packed with 5  $\mu\text{m}$  porous silica particles (100 nm pore size), which served as stationary-phase backbone/matrix and filter for nanoparticle clusters. The self-assembled aggregates formed by nanoparticles and model molecules were collected from the reaction test tubes and then packed into the column using the slurry-packing technique introduced earlier.



Figure 6-11: Packing self-assembled aggregate into the HPLC column.

### 6.3 Conclusions

In this chapter, we have proposed and demonstrated a new approach to prepare fully packed nanoparticle HPLC columns called molecular-self-assembly-assisted nanoparticle packing. A solvent screening procedure was defined and executed to locate a working solvent system (ethanol/ethanol) for the molecular self-assembly process. 30-nm-sized gold nanoparticles were crosslinked by thiolated model molecules into micron-sized clusters inside the microfluidic devices. The assembled compounds were successfully packed into the microchip LC columns. The morphology, electrical properties and thermal stability of the assembled compounds were characterized, which confirmed that the gold-thiol chemistry indeed occurred during the assembly process.

## 6.4 Bibliography

- [1] V. R. Meyer, in *Practical high-performance liquid chromatography*, 3rd ed. New York: Wiley: Chichester, 1998.
- [2] J. M. Cintron and L. A. Colon, "Organo-silica nano-particles used in ultrahigh-pressure liquid chromatography," *Analyst*, vol. 127, pp. 701-704, 2002.
- [3] Z. J. Tan and V. T. Remcho, "Bonded polymethacrylate stationary phases for open tubular liquid chromatographic and electrochromatographic separations," *Journal of Microcolumn Separations*, vol. 10, pp. 99-105, 1998.
- [4] O. Bruggemann, R. Freitag, M. J. Whitcombe, and E. N. Vulfson, "Comparison of polymer coatings of capillaries for capillary electrophoresis with respect to their applicability to molecular imprinting and electrochromatography," *Journal of Chromatography A*, vol. 781, pp. 43-53, 1997.
- [5] L. Schweitz, P. Spegel, and S. Nilsson, "Molecularly imprinted microparticles for capillary electrochromatographic enantiomer separation of propranolol," *Analyst*, vol. 125, pp. 1899-1901, 2000.
- [6] P. Viberg, M. Jornten-Karlsson, P. Petersson, P. Spegel, and S. Nilsson, "Nanoparticles as pseudostationary phase in capillary electrochromatography/ESI-MS," *Analytical Chemistry*, vol. 74, pp. 4595-4601, 2002.
- [7] S. E. Martin, J. Shabanowitz, D. F. Hunt, and J. A. Marto, "Subfemtomole MS and MS/MS peptide sequence analysis using nano-HPLC micro-ESI Fourier

- transform ion cyclotron resonance mass spectrometry," *Analytical Chemistry*, vol. 72, pp. 4266-4274, 2000.
- [8] C. Y. Shih, S. Zheng, E. Meng, Y. C. Tai, Y. Liu, and J. F. Stoddart, "Nano-to-micro self-assembly using shear flow devices," presented at the 17th IEEE International Conference on Micro Electro Mechanical Systems (MEMS 2004), Maastricht, the Netherlands, 2004.
- [9] C. Y. Shih, S. Zheng, Y. C. Tai, Y. Liu, and J. F. Stoddart, "Shear flow self-assembled gold nanoparticle film for chemiresistor sensor applications," presented at the 8th International Conference on Miniaturized Systems in Chemistry and Life Sciences, Malmo, Sweden, 2004.
- [10] A. N. Shipway, M. Lahav, R. Gabai, and I. Willner, "Investigations into the electrostatically induced aggregation of Au nanoparticles," *Langmuir*, vol. 16, pp. 8789-8795, 2000.
- [11] M. A. Unger, H. P. Chou, T. Thorsen, A. Scherer, and S. R. Quake, "Monolithic microfabricated valves and pumps by multilayer soft lithography," *Science*, vol. 288, pp. 113-116, 2000.
- [12] J. J. Storhoff, A. A. Lazarides, R. C. Mucic, C. A. Mirkin, R. L. Letsinger, and G. C. Schatz, "What controls the optical properties of DNA-linked gold nanoparticle assemblies?" *Journal of the American Chemical Society*, vol. 122, pp. 4640-4650, 2000.
- [13] M. A. Hayat, *Colloidal gold: principles, methods, and applications*, vol. 1. San Diego: Academic, 1989.

---

# CHAPTER 7

---

## CONCLUSIONS

With the growing analytical needs from the fields of chemistry, biotechnology, and pharmaceuticals, there is no doubt that HPLC will remain an important analytical tool and research topic in the future. Each year, thousands of papers are published on HPLC related topics. While most of them are based on conventional capillary HPLC research, one would find that more and more works are focused on chip-based HPLC systems. Indeed, as was said in the title of Richard Feynman's famous speech, "There is plenty of room at the bottom", the microchip HPLC research field is young, attractive, and full of opportunities. A fully integrated microchip HPLC system allows crucial applications including personal health monitoring, point-of-use testing, or much lower analysis cost for regular HPLC analysis in the labs. The potential markets and revolution to everyday life are significant and promising.

This thesis aims to explore state-of-the-art technologies for building microchip HPLC systems and to examine chromatographic performances of such systems. Chapter 3 demonstrates using MEMS technology to make high-pressure microfluidic channels, which were used for constructing microchip HPLC systems. Chapter 4 describes the world's first temperature-controlled microchip HPLC system that uses a temporal temperature gradient to achieve analyte elution. Separation examples of amino acids and low density lipoprotein were successfully demonstrated. Chapter 5 describes a novel embedded HPLC system that has the record high pressure capacity ( $> 1000$  psi) among all microchip HPLC systems. High quality separation results of trace-level daunorubicin and doxorubicin were obtained using the proposed system with incorporated laser-induced fluorescence detection and LABVIEW program for procedure automation. A novel  $C^4D$  sensor together with the RISE sensitivity enhancement method was proposed and investigated for the first time for microchip HPLC analyte detection. Finally, chapter 6 reports the first work of packing 30 nm gold nanoparticles into an HPLC separation column as the stationary phase with the assistance of in-situ molecular self-assembly between nanoparticles and thiolated molecules. Preliminary results demonstrated the possibility of building a fully filled nanoparticle HPLC column for extremely high separation efficiency application.

Studying the published works in the HPLC field, the future research of microchip HPLC can be partitioned into two categories. The first category is to speed up the commercialization process for microchip HPLC systems, which requires further improvements on system components integration, separation performance (efficiency and reproducibility), and manufacturing costs. Demonstrating that microchip HPLC has

comparable or superior performance to conventional desktop HPLC is especially important since most applications will still come from industries where separation reproducibility is often the top criterion. Once the industry is willing to accept the microchip HPLC system, the mass production of microchip HPLC by MEMS will surely guarantee significantly lower manufacturing costs.

The second research category is to further miniaturize HPLC system down to the “nano” scale, which includes using nanometer-sized column inner diameters and stationary-phase particles; nanoliter-sized sample injection volumes, detection cell volumes, and fluidic swept/dead volumes; nanoliter/min mobile phase flow rates. In the nano scale, extremely high sensitivity (single molecule detection) and separation efficiency (millions plates/cm) can be expected and new phenomena based on known physics can often appear that are surely of major scientific interest. The manufacturing and analysis of such systems will as well take experiences from the accumulated research efforts on modern nanotechnology.

I feel grateful to be able to work on and contribute to the advancement of microchip HPLC. Doing molecular separation on-a-chip is not only a fun thing to do but also it makes lots of sense in terms of getting better performance and faster analysis. I am looking forward to the near future where I can buy microchip HPLC from drugstores and carry out self-diagnosis at home with a cost lower than driving to a hospital!